Structural Studies of Copper Tetra-Tert-Butyl Phthalocyanine Langmuir-Blodgett and Vacuum Deposited Films

A thesis for the degree of

PHILOSOPHIAE DOCTOR

Presented to

DUBLIN CITY UNIVERSITY

By

C. J. Hanson B.Sc.
School of Physical Sciences
Dublin City University

Research Supervisor: Dr. A. A. Cafolla

External Examiner: Dr. S. Clarke
Internal Examiner: Dr. E. McLoughlin

January 2008

To my darling daughter Faye

Declaration

I hereby certify that this material, which I now submit for assessment on the programme of study leading to the award of Doctor of Philosophy (PhD) is entirely my own work, that I have exercised reasonable care to ensure that the work is original, and does not to the best of my knowledge breach any law of copyright, and has not been taken from the work of others save and to the extent that such work has been cited and acknowledged within the text of my work.

Signed: Claire Hanson

ID No.: 98015737

Date: 22/01/2006.

Contents

Abstract

The Langmuir-Blodgett (LB) technique was employed to fabricate thin films of Copper-Tetra-Tert-Butyl Phthalocyanine (CuTTBPc). However, CuTTBPc has a strong tendency to aggregate and hence inhibit the synthesis of uniform layers. It has been found that the incorporation of Arachidic Acid (AA) can reduce the aggregation effect A study of the isotherms produced for a variety of concentrations of CuTTBPc:AA showed a reduction in the aggregation as the amount of AA was increased. Transfer ratios for such films are predominately Y-type indicating that deposition occurred on both the up- and downstroke

Atomic Force Microscopy (AFM) was used to image the CuTTBPc.AA LB films with a thickness of 1 – 21 MLs. Good surface coverage was observed. Height profile studies of the 1 ML film indicate that the layer is 1.7 nm in thickness. When the film thickness is increased the topography of the surface consists of clusters typically associated with aggregation. The uniformity of the films was examined by spectroscopic ellipsometry, whereby it became evident that films were growing in a uniform layer-by-layer fashion despite the obvious presence of aggregation. The average layer thickness, deduced from the ellipsometric data, was 2.31nm. The uniform growth would suggest the layers were depositing on both the up- and downstroke making the films Y-type in configuration and perhaps indicating that the films have a Stranski-Krastanov structure. Scanning Tunnelling Microscope (STM) images of CuTTBPc on Ag/Si(111)-($\sqrt{3}$ x$\sqrt{3}$)R30° found the molecules to be flat lying. The surface was highly ordered and densely packed with molecules forming rows, which ran parallel to each other. Scanning Tunnelling Spectroscopy (STS) studies found that the Highest Occupied Molecular Orbital (HOMO) is a half-occupied MO of b_{1g} symmetry with mixed Cu 3d(x^2-y^2) and ligand 2p character.

A study of the orientation and molecular ordering of the CuTTBPc molecule in a pure CuTTBPc LB film (on SiO_2) and evaporated films of CuTTBPc(on SiO_2 and Si(111)) and H_2TTBPc (SiO_2) was carried out using X-Ray Photoemission Spectroscopy (XPS) and Near Edge X-ray Absorption Fine Structure (NEXAFS) A strong angular dependence was found indicating that the molecule was tilted on the surface. The tilt angle was calculated to be 18.5° to the surface normal XPS results revealed that the ordering was strongest in the CuTTBPc LB film, followed by the evaporated films of CuTTBPc and H_2TTBPc on SiO_2, followed by CuTTBPc on Si(111). A study of the electronic structure of the copper atom in the CuTTBPc was also carried out and the found to be in good agreement with previously published work.

Acknowledgements

First and foremost I would like to thank Dr. Tony Cafolla for allowing me the opportunity to carry out a PhD under his supervision. Over the last number of years Tony has offered invaluable help, advice and support with my research. I would like to thank Dr. Sergey Krashniov who helped with the STM, XPS and NEXAFS experiments. Without Sergey's help there simply would not be any STM, XPS or NEXAFS data for this project. Many thanks to Mr. Henry Barry who offered tremendous help with the gathering and analysing of the ellipsometry data. Thanks to Zheshen Li for his help with NEXAFS experiments in Arrhus University, Denmark. I am grateful to Professor Phillip Mortiary and Mr. Cong Yang (both from Nottingham University, UK) who allowed me the use of their brand new LB bath. I spent six months in Nottingham on a Marie Curie Scholarship and during that time I synthesised all the LB films used in this research.

Over the years I have made many friends with the people in the physics department in DCU. Whether you were from my Surface Science group or another group you made my time at DCU more enjoyable and there was always someone around for coffee or the pub. I would also like to thank Robert Groake from the chemistry department, DCU.

I am indebted to my family who have supported me over the years. In particular I'd like to thank my aunt and uncle, Marian and Aidan. I went to live with them when I started secondary school at the age 13 and some 14 years later "the mucky orphan" finally left the nest. A big thank you for all your help, support and friendship over the years.

Many thanks to my parents, brother, sisters and extended family. After almost 9 years I'm finally finishing up in DCU!!! I bet you'd never thought you'd never see the day.

Thanks to my partner Martin who has been a shoulder to lean on, especially during the writing of this thesis when I spent a lot of time in hospital when I was pregnant with our daughter Faye.

The work in this thesis was funded by the School of Physical Sciences, DCU, and the Marie Curie EU Scholarship programme.

List of Publications

C. Hanson, A.A. Cafolla, H. Barry, **An ellipsometry and AFM study of CuTTBPc:AA mixed LB films**, to be published

Sergey A. Krasnikov, Claire J. Hanson, Attilio A. Cafolla, **Dimer structure of the CuTtertBuPc layer on the Ag/Si(111)-($\sqrt{3} \times \sqrt{3}$)R30° surface: STM/STS study**, accepted for publication in Journal of Physics Condensed Matter.

S. A. Krasnikov, C. J. Hanson, J. P. Beggan, A. A Cafolla, **Ordering on CuTTBPc on Si substrates studied by NEXAFS and VB XPS using Synchrotron Radiation**, in Press.

Kathleen Grennan, Anthony J. Killard, Claire J. Hanson, Attilio A. Cafolla, Malcolm R. Smyth, **Optimisation and characterisation of biosensors based on polyaniline**, Talanta, 68 (2006) 1591-1160

J. Fryar, E. McGlynn, M.O. Henry, A.A. Cafolla, C.J. Hanson, **Excitonic properties of the polar faces of bulk ZnO after wet etching**, Physica B, 340 – 342 (2003) 210-215.

List of Figures

List of Tables

Chapter 1

Introduction

The ***Langmuir-Blodgett (LB)*** technique involves the study and manipulation of molecules trapped at an interface, such as air-water. These molecules form thin molecular films, which can be compressed and transferred onto solid substrates. An everyday example of a thin film would be oil on water and folklore has it that oil has the ability to calm troubled water. However, it was not until 1773 that Benjamin Franklin carried out the first scientific study of this phenomenon [1]. During a stay in England he observed rough winds over a pond in Chapham Common [2]. He tried to smooth the waves by adding a little oil to the pond and much to his surprise he noted how the oil spread swiftly on the surface of the water and produced an "instant calm". He had only used a teaspoon of oil and managed to cover about a quarter of the pond. The area of the pond covered (approximately half an acre) was "as smooth as a looking glass". Franklin reported his findings to the Royal Society of London in 1774 [3], however, at that time the concept of atoms and molecules did not exist and therefore his experiment went largely unnoticed. If Franklin had been able to calculate the thickness of the oil he would have discovered that it was indeed one monolayer in thickness.

Lord Rayleigh began calculating the thickness of thin films in 1890. He was able to quantitatively measure the area to which a known volume of oil would expand and from that deduced the thickness of the oil film [1]. At this time a German woman named Agnes Pockels (1862-1935) was also carrying out pioneering work in her own home. For almost 10 years she had studied surfactants and surface tension in her kitchen. Her results were sent to a professor of physics in the University Of Goettingen but were not appreciated [4]. When Lord Rayleigh began to publish his findings she wrote him a letter about her works and Rayleigh was so impressed that he sent it to *Nature* to be published [5].

Pockel's work revealed how she built a simple rectangular trough (70cm long, 5cm wide and 2 cm high) out of tin and filled it with water [5]. She then used another strip of tin, 1.5 cm in width, to partition two sides of the baths. This partition (or barrier) was adjustable and hence it was possible to vary the area of the two

water surfaces. She used a small disc, believed to be a button, of 6mm in diameter to monitor surface tension by attaching it to a balance. Of the many things that she discovered, she was able to obtain a perfectly clean surface by fully closing the trough (i.e. bringing the partition to the edge of the trough) and then moving it back to center again. By doing this, the surface on one side is formed from the interior of the liquid and is clean. She also discovered that perfectly pure surfaces can be contaminated by the vessels in which they are contained and that any solid body, no matter how clean, will contaminate a newly formed surface. She epitomised this by showing how the addition of camphor or flour to the trough leads to a change in the surface tension [5]. The above described work by Pockels lead to her first scientific publication in *Nature* which Lord Rayleigh assisted her in the publication of as "for various reasons I (Pockels) am not in a position to publish them in scientific periodicals". In total she had fourteen publications but during that time women were not accepted for higher education. Her parents did not encourage her to pursue her education even when it did become acceptable for women to do so [4].

The flow of molecules between both sides of the bath was also of importance to Pockel. She noted that if both sides of the bath were contaminated and the partition removed the molecules tended to flow from the more contaminated side to the least contaminated side. She undertook experiments to see how wax, sulphur, wood and tinfoil contaminated surfaces.

Today many of the standard techniques used in the production of thin films are the same as those used by Pockels. She introduced the idea of using spreading solvents, (e.g. chloroform) to spread small quantities of material rapidly and accurately across the surface [6]. She obtained isotherms (discussed below) of stearic acid which are now considered to be essentially correct [6]. Lord Rayleigh also conducted experiments on these films and found them to be in the order of one monolayer thick [7].

In 1931 she won the "Laura Leonard Prize" with Henri Devaux for "Qualitative investigation of the properties of surface layers and surface films". In 1932, three years before her death she received an honorary Doctorate from the Carolina-Wilhelhima University in Brunswick, Germany [4].

The Nobel Prize winner (1933) Irving Langmuir made considerable contributions in the field of thin films [8]. He set about studying the pressure-area relationship of molecules on an aqueous phase and found that the areas occupied by molecules such as acids, alcohols and esters were independent of the chain length, showing that only the hydrophilic head groups were immersed in the liquid ***subphase***. In terms of the LB technique the subphase is the liquid on which the floating monolayer resides. The equipment he used was very similar to that used by Agnes Pockels and he was the first scientist to show that molecules have a preferred orientation at the air-water interface. For these measurements he devised the surface balance used for monitoring the surface pressure [9], subsequently named the Langmuir balance. Katherine Blodgett worked with Langmuir and together they demonstrated that it was possible to transfer monolayers onto solid substrates and that one could build a film consisting of a multilayer stack of any required thickness [6]. Today any films made in such a manner are known as ***Langmuir-Blodgett (LB) films***.

This research focuses primarily on the synthesis of LB films containing ***Arachidic Acid (AA)*** and ***Copper-Tetra-Tert-Butyl Phthalocyanine (CuTTBPc)***. Phthalocyanines are natural occurring dyes which are made up of macrocyclic compounds. Since phthalocyanines are naturally dyes they are readily available. A variety of phthalocyanine complexes exist as it is possibly to alter the central metal atom and the side chains attached to the phthalocyanine ring. Over recent years phthalocyanines have attracted considerable attention due to their semi-conducting properties and their chemical and thermal stability which in turn makes them ideal candidates in the field of photoconductors, photovoltaic cell elements, optical devices, non-linear optics, electrocatalysis and gas sensing devices [10][11][12]. In this research CuTTBPc was studied in LB films and evaporated films. CuTTBPc has previously been studied in terms of LB films and evaporated films [11] but this work focuses primarily on the molecular ordering within the films.

Traditionally molecules used in LB research are amphiphilic in nature, meaning that the molecule has both hydrophobic and hydrophilic properties. AA is a good example of an amphiphilic molecule with the carboxyl group being hydrophilic

and the alky chain being hydrophobic. CuTTBPc, in contrast to AA, is not amphiphilic as it does not contain any hydrophilic groups (such as a carboxyl group), but consist mainly of hydrophobic moieties (phthalocyanine ring and tert butyl groups). This makes the synthesis of LB films containing CuTTBPc a challenging process as the molecules tend to aggregate and form clusters. Sheu *et. al.* [13] and Emelianov *et. al.* [14] [15] found that by mixing AA together with CuTTBPc the aggregation could be reduced and the film quality improved.

LB films can be made to exact thicknesses and should encompass a well packed surface with a good structural uniformity. For this reason LB films of pure CuTTBPc were produced alongside vacuum deposited films of CuTTBPc to compare the molecular ordering within both types of film. Mixed LB films, produced with varying molar concentrations of CuTTBPc:AA, were synthesised to investigate if aggregation decreased upon the incorporation of AA into the CuTTBPc film. Films, ranging in thickness from one ***monolayer (ML)*** to twenty one MLs were produced to study the layer-by-layer growth structure of the mixed films.

A range of techniques were employed to study the quality, thickness and structural properties of mixed CuTTBPc:AA films. The film quality and coverage was investigated by ***Atomic Force Microscopy (AFM),*** where it was possible to study the films on a sub-micron scale, and ***ellipsometry*** was used to determine the exact thicknesses of the various films. For the pure CuTTBPc films ***Scanning Tunneling Microscope (STM), Scanning Tunneling Spectroscopy (STS), X-ray Photoemission Spectroscopy (XPS)*** and ***Near Edge X-ray Absorption Fine Structure (NEXAFS)*** were used to probe the surfaces. The orientation of individual CuTTBPc molecules on Ag/Si(111)R30°($\sqrt{3}$ x $\sqrt{3}$) was observed using STM and the HOMO-LUMO band gap of CuTTBPc was found using STS. Detailed studies of the NEXAFS spectra revealed the presence of molecular ordering and made it possible to calculate the exact tilt angle of the CuTTBPc molecule within an LB film of CuTTBPc (on SiO_2). The NEXAFS spectra were compared to XPS spectra of evaporated CuTTBPc (on SiO_2 and Si(111)) and H_2TTBPc (on SiO_2) and were found to be good agreement with each other.

Chapter 2 outlines the theory of the LB process and the other techniques employed in this work. The floating monolayer, pressure measurements, isocycles and target pressure are discussed in sections 2.1.2-2.1.3. From these many properties such as the monolayer stability, aggregation, phase changes, target pressures etc. are determined. The deposition process and transfer ratios (sections 2.1.4-2.1.5 respectively) indicate whether the film is X, Y or Z type and whether the films quality is good. Sections 2.2 and 2.3 covers the theory behind the AFM and STM where the different modes of operation and scanning probes are detailed. Ellipsometry and the interaction of polarised light with a solid substrate and subsequent deduction of the film thickness is discussed in section 2.4. A description of the photoemission process is given in section 2.5 and the NEXAFS process is given in section 2.6.

The experimental procedures for the LB, AFM, STM, ellipsometer, XPS and NEXAFS are discussed in chapter 3, where detailed accounts of the Nima 2022 and Nima 312D LB baths are given. The cleaning procedure of the subphase is outlined and the preparation of the plasma etched silicon substrates is given along with the preparation procedures of the materials which were used in the bath. Evaporated films of CuTTBPc on Ag/Si(111)R30°($\sqrt{3}$ x $\sqrt{3}$) were studied under UHV with an Omicron STM. The experimental setup of the STM is given in section 3.2. Tapping mode AFM is described in section 3.3. A Digital Instruments AFM was used to image the LB films. The experimental setup of the ellipsometer is found in section 3.4 XPS experiments were carried out in the Daresbury Laboratories, UK, while the NEXAFS experiments were carried out in Aahrus University, Denmark. Descriptions of the experimental setups for the XPS and NEXAFS measurements are presented in sections 3.5 and 3.6 respectively.

Chapter 4 reports the findings of LB films produced using pure AA, pure CuTTBPc and mixed films of AA and CuTTBPc. AA films were grown to gain familiarity with the LB technique and experience in the interpretation and analysis of isotherms. A range of films were produced and, as predicted, were Y-type in configuration. A study was undertaken to investigate if changes in dip speed, pH or drying times between layers would affect the film quality. The isotherm for pure

CuTTBPc exhibited strong aggregation which made the synthesis of smooth monolayers a cumbersome task. AA was incorporated into the CuTTBPc monolayer in differing molar ratios to try and reduce aggregation and improve film quality.

In chapter 5 topographical, orientation and height studies were carried out using the AFM, STM and ellipsometer. Using the AFM it was found that the surface roughness increased as the thickness of the mixed CuTTBPc films increased. Ellipsometry results showed that there was a linear growth in the film thickness as the number of layer increased for the 1:1 CuTTBPc:AA films. Such a strong linear trend indicates that the layers must have been depositing on both the up- and downstroke. This would agree with the LB results and confirm that the films are Y-type in structure. Through analysis of the ellipsometry data film thickness, refractive index and extinction coefficients were determined. An STM study of CuTTBPc on Ag/Si(111)R30°($\sqrt{3}$ x $\sqrt{3}$) revealed a highly ordered and densely packed surface which has previously been unreported in literature. The molecules are found to form rows, two molecules in width, running parallel to each other across the surface. It was possible to view both the empty and filled states of the molecule by altering the voltage bias of the tip. STS data for CuTTBPc on Ag/Si(111)$\sqrt{3}$ was in excellent agreement with XPS and NEXAFS data for thin films of evaporated CuTTBPc in this work.

Chapter 6 discusses the NEXAFS and XPS results. Using the NEXAFS technique a decrease in the HOMO peak as a function of angle of incoming radiation showed that the molecule had a strong angular dependency and hence must be highly ordered on the surface. It was possible to calculated the exact tilt angle of CutTTBPc in a 12 ML LB film on SiO_2. Analysis of the XPS would verify the NEXAFS results and confirm that there was a definite ordering of the CuTTBPc molecule, not only in the LB film but also in the evaporated films. The XPS results disclosed how the substrate and method of film deposition can influence the orientation of the molecule. It was found that LB films are more ordered than evaporated films and that films grown on SiO_2 are more ordered than those on Si(111).

Chapter 7 discusses the overall finding of the work in thesis.

Chapter One References

[1] www.umn.edu

[2] Nima Technology, **Tensiometers and Langmuir-Blodgett Troughs**, Operating Manual, 4th Edition, 1995.

[3] Of the Stilling of Waves by means of Oil. Extracted from Sundry Letters between Benjamin Franklin, L.L. D. F. R. S. William Brownrigg, M. D. F. R. S. and the Reverend Mr. Farish, 1774.

[4] http://www.physics.ucla.edu

[5] A. Pockels, "Surface Tension", ***Nature***, 43, (1891) 437.

[6] www.nima.co.uk

[7] Lord Rayleigh, ***Philosophical Magazine***, 48, (1899) 321.

[8] www.woodrow.org

[9] Gaines, G. L., Jr. **Insoluble Monolayers at Liquid-Gas Interfaces**; Interscience: New York, 1996.

[10] N. Kobayashi, Curr. Opin, ***Solid State Material Science***, 4 (1999) 345.

[11] C.C. Leznoff, A.B.P. Lever (Eds.), **Phthalocyanines, Properties and Applications**, Vol. 1–4, VCH, New York, 1989.

[12] I.L. Emelianov, V.V. Khatko, ***Sensors and Actuator B***, 60 (1999) 221.

[13] C-W Sheu, K-M Lin, I-H Ku, C-H Chang, Y-L Lee, Y-M Yang, J-R Maa ***Colloids and Surfaces A: Physicochemical and Engineering Aspects***, 207 (2002) 81–88.

[14] I.L. Emelianov, V.V. Khatko, ***Thin Solid Films***, 354 (1999) 237-244.

[15] I. Emelianov , V. Khatko, A. Tomchenko, ***Sensors and Actuators B***, 47 (1998) 158–163.

Chapter 2

Theoretical Background

Here in Chapter 2 the theory behind the techniques used to produce and analyse LB films and evaporated films is explained. Section 2.1 gives a theoretical description of LB process. The STM and AFM techniques are described in sections 2.2 and 2.3, respectively. Ellipsometry is explained in section 2.4, while XPS and NEXAFS are explained in sections 2.5 and 2.6.

2.1 Langmuir-Blodgett Films

2.1.1 Introduction to Langmuir-Blodgett Films

Interest has grown in the field of LB research over recent years. The LB technique allows the user to manipulate molecules trapped at an interface. Film thickness can be accurately controlled as the technique involves the deposition of one monolayer on top of another. The film thickness can therefore be controlled to within one monolayer. This has made the LB process a valuable technique in the field of Nanoscience where molecular devices, such as gas sensors, photoconductors and optical devices, can be constructed with great precision [1]. Ordered films can also be synthesised under UHV but UHV equipment can be very expensive compared to LB equipment. Obtaining the correct pressure when using thermal evaporation can be time consuming. This is not a problem with the LB technique as film synthesis is preformed in air in standard laboratory settings. In addition thin films may be produced via spin coating but such films often contain spin specific defects. Occasionally substrate breakage occurs as the film is being deposited and high energy costs can also be incurred. For these reasons the LB technique was favoured. The behavior and control of molecules on a subphase is discussed in the following sections. The deposition process along with the different types of LB films is also explained.

2.1.2 The Floating Monolayer and Pressure Measurements

For a molecule to be suitable for LB film deposition it must have amphiphilic properties. An amphiphilic molecule consists of both a hydrophobic and hydrophilic part. The hydrophilic (water loving) part of the molecule is attracted to polar media such as water. Examples of hydrophilic groups are carboxylic acid, sulphates, amines and alcohols. Hydrophobic groups (water hating) are typically hydrocarbon chains, fats and lipids. Amphiphilic molecules are also known as surfactants or surface-active molecules, as they have one part of the molecule attracted to the subphase and the other pulling away from the subphase. These properties make the molecules float at the air-water interface [1].

Most molecules exist in a powdered and aggregated form therefore, in order to spread a monolayer on the subphase, it is necessary to dissolve the molecule in a non-aqueous volatile solvent, such as chloroform, benzene etc. This spreads the molecules over the surface as the solvent evaporates and the molecules orientate at the interface with the hydrophobic tails pointing into the air and the hydrophilic part pointing into the subphase [2]. A schematic illustration of the molecules at the air-water interface is given in figure 2.1.

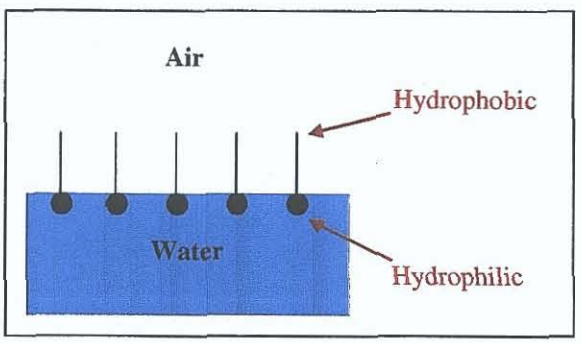

Figure 2.1: Amphipilic molecules at the air-water interface.

When the molecules are initially spread onto the subphase the area occupied per molecule is large and no lateral adhesions exist. The surface pressure is therefore low and the size of the molecules compared to the area of the subphase is negligible. It can be assumed that the molecules obey the "Ideal Gas Equation":

$$PV = nRT \tag{2.1}$$

Where P is pressure, V is volume, n is number of moles, R is the gas constant and T is temperature. In the two dimensional case of Langmuir films $P = \pi$ (surface pressure) and $V = A$ (area per molecule) which gives the following equation

$$\pi A = kT \tag{2.2}$$

where k is Boltzmann's constant [3]. Upon compression, the distance between the molecules decreases resulting in an increase in the surface pressure. This leads to the transition from gas phase to liquid phase to solid phase, as shown in figure 2.2.

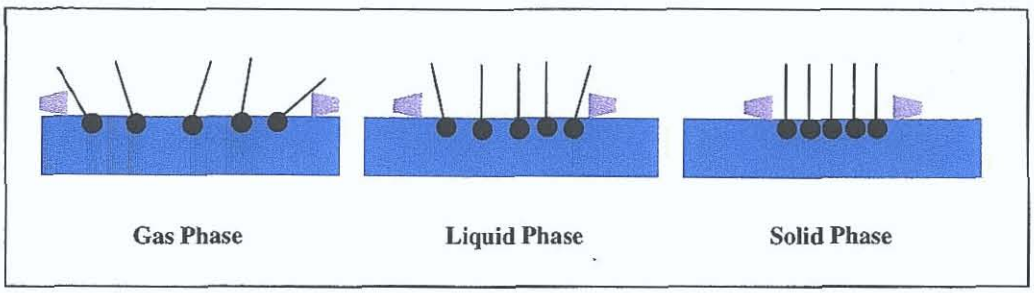

Figure 2.2: The different phases molecules occupy upon compression of the monolayer with the barriers shown in purple.

A plot of the change in surface pressure versus area gives an ***isotherm***, which is a graphical representation of the phase changes. Figure 2.3 shows isotherms of an arachidic acid (AA) and copper tetra-tert-butyl phthalocyanine (CuTTBPc) molecules. It should be noted that every molecule has it own unique isotherm, which acts as a fingerprint. Ideally the isotherm should show distinct regions where the phase transitions are obvious but this is not always the case. Most molecules, such as phthalocyanines, do not exhibit this behaviour making it difficult to determine the exact point at which a phase transition occurs.

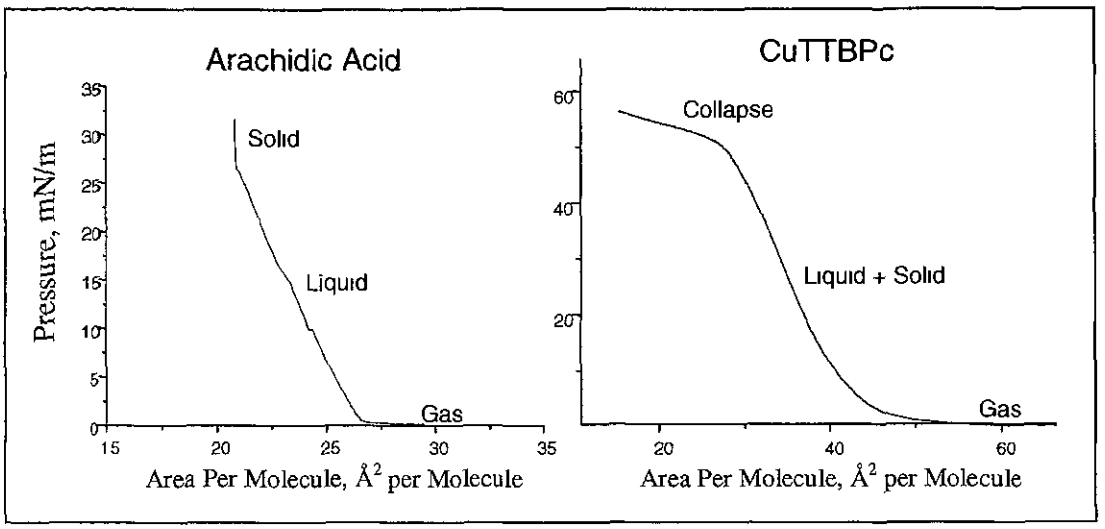

Figure 2.3: Examples of isotherms for AA and CuTTBPc. The AA isotherm is an "ideal" isotherm in that it clearly shows the phase changes. On the other hand there is no clear distinction between the liquid and solid phase for CuTTBPc.

When the liquid expanded state is reached the molecules have some degree of freedom and gauche formations result from the repulsive steric strain interactions which occur when atoms or molecules are forced together more than their atomic radii allow, hence there is an increase in pressure. Further compression forces the molecules to pack tightly together and the monolayer is then said to be in its liquid condensed or solid phase. It is possible to make a monolayer collapse by compressing it too much. This collapse can be observed as a sudden rise followed by a sharp drop in surface pressure as the layer collapses.

The pressure sensor used in this research is a Wilhelmy paper plate made from Whatman chromatography paper of dimensions width (w) 10mm, thickness (t) 0.15 mm, and length (l) 20 mm, figure 2.4. The Wilhelmy plate has a weight of 100 mg or 0.1 x 10^3kg. When the plate comes in contact with the subphase a number of forces act upon it. Gravity and surface tension pull the plate downwards while buoyancy due to displaced water push the plate upwards. The net force acting on the plate is described by the following equation [2]

$$\text{Force} = \text{weight} - \text{upthrust} + \text{surface tension} \qquad (2.3)$$

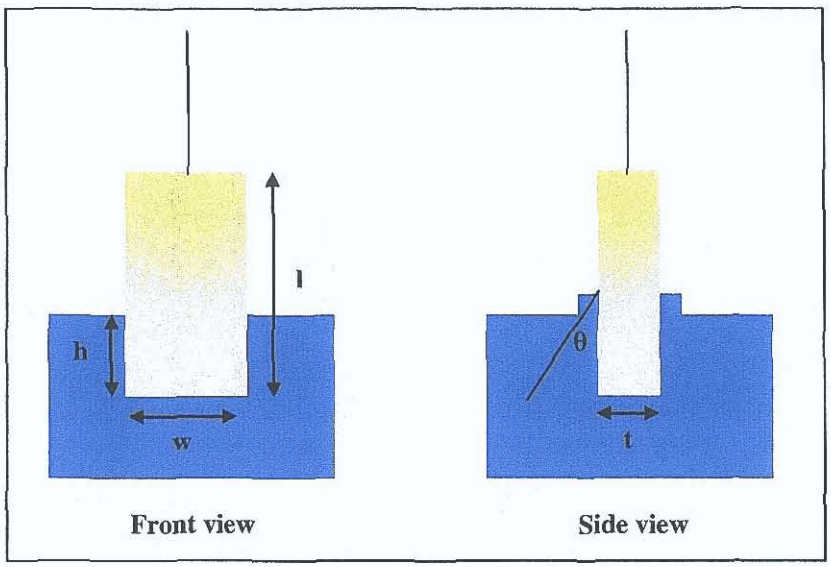

Figure 2.4: A Wilhelmy plate immersed in water

For a plate of dimensions length × width × thickness (l × w × t) and density ρ, immersed in a liquid subphase to a depth of h, equation 2.3 becomes:

$$F = \rho glwt - \rho' ghwt + 2\gamma(t + w)\cos\theta \tag{2.4}$$

where γ is the surface tension of the liquid, ρ is the density of the plate, ρ' is the density of the subphase and θ the contact angle between the plate and the subphase. When taking surface tension measurements the pressure sensor is "zeroed" this means that the ρglwt (weight) and ρ'ghwt (upthrust) are adjusted to zero. Therefore, any additional measured force is equal to surface tension.

$$F = 2\gamma(t + w)\cos\theta \tag{2.5}$$

Assuming that the angle θ is 0° (i.e. cos θ = 1) and that the thickness of the plate is so small that it can be ignored then the force simplifies to

$$F = 2\gamma w \tag{2.6}$$

Taking the mass of the Wilhemly plate as 0.1 x 10^{-3}kg and acceleration due to gravity as 9.81 ms^{-2} gives:

$$F = mg = 0.1 \times 9.81 = 2\gamma w \tag{2.7}$$

which gives a surface tension value of 49.1 mN/m for a 100 mg mass. The computer software is programmed to read this value as a negative value thus ensuring that a positive surface tension reading is obtained when the plate is lifted out the liquid.

It is standard practice to check the pressure sensor by lifting it out of pure water, which should give a surface tension value of 72.8 mN/m at 293K. Another way of checking the sensor is to attach the 100 mg calibration mass to the pressure sensor and adjusting the calibration until a reading of –49 1 mN/m is obtained for a 100 mg mass.

The difference in downwards force, ΔF, experienced by the plate when immersed in pure water and and the force experiences in the surfactant covered water is given by:

$$\Delta F = 2(\gamma'-\gamma)(t + w) \tag{2.8}$$

γ and γ' are the surface tension of the pure water (72.8 mN/m) and the surfactant covered water respectively. Again it can be assumed that the plate thickness is so small that it can be ignored. So for a 10mm wide paper plate

$$\Delta F = 2(\gamma'-\gamma) \quad \text{or} \quad \Delta F = 2(\Delta\gamma) \tag{2.9}$$

where $\Delta\gamma$ is defined as the surface pressure, π.

Hence for a paper plate of width 10 mm the force is equal to twice the surface pressure (or twice the change in surface tension)

$$\Delta F = 2(\gamma' - \gamma) = 2\pi \tag{2.10}$$

The pressure sensor measures π ($= \gamma' - \gamma$) , which corresponds to the surface pressure of the adsorbed surfactant. The accuracy in the pressure readings is ±0.1 mN/m for the pressure sensor used in this experiment.

2.1.3 Isocycles and Target Pressure

Continuous compressions and expansions of a monolayer result in better "packing" of molecules and can give more accurate isotherms. The trough is programmed to carry out these compressions and expansions (also called ***isocycles***). The speed at which the barrier moves and the pressure to which the monolayer is compressed is defined by the user. The pressure should not be so high as to collapse the layer, as this means that molecules can be forced into the subphase or that the molecules can form aggregates. The ***Limiting Area per Molecule*** and ***Target Pressure*** are determined by studying the isotherms and the pressures in the solid and

liquid phases. When a satisfactory, reproducible isotherm is obtained the limiting area per molecule is found by extrapolation of the isotherm to the x-axis (area/molecule). The target pressure is the pressure at which the film is held when transferring it onto a solid substrate. Normally the target pressure is the pressure at which the film enters the condensed or solid state phase. Once the target pressure is chosen it is necessary to check the stability of the film by recording an "area/pressure versus time" graph. For a stable film little or no change in area should occur when the film is held at the target pressure for a fixed period, usually 30 minutes. Once the correct target pressure is achieved the film can be transferred onto a solid substrate.

2.1.4 Deposition onto a Solid Substrate

When the monolayer is compressed to its correct target pressure a film can be transferred by lowering the substrate into the subphase. Both hydrophobic and hydrophilic substrates can be used for LB films and depending on the nature of the substrate, the layer can deposit in different ways.

Hydrophobic substrates are held above the subphase and lowered into the subphase when the film is at its correct target pressure. The film then attaches onto the slide on the downstroke when the hydrophobic end of the molecule is attracted to the hydrophobic substrate. For this reason the meniscus of the film curves in the same direction as the substrate travel as shown in figure 2.5.

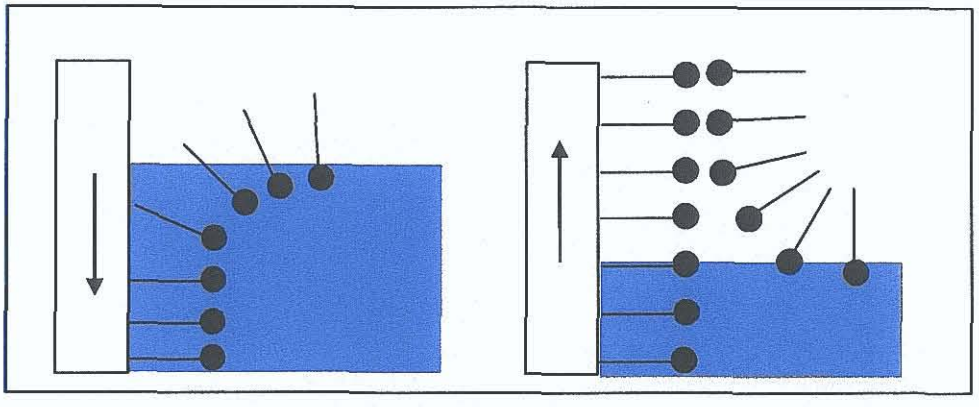

Figure 2.5: Deposition of the 1st and 2nd layer onto a hydrophobic substrate.

Hydrophilic substrates can start either above or below the subphase during the dipping process. If they start above, then in theory no molecules should be picked up on the downward stroke. On the upward stroke the hydrophilic parts of the molecule should attach to the substrate. As with hydrophobic substrates the meniscus should follow the direction of the dip, as illustrated in figure 2.6.

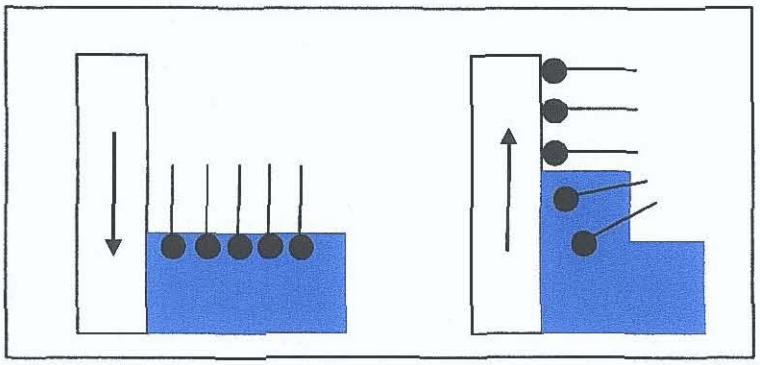

Figure 2.6: *Deposition on to a hydrophilic substrate. Note there is no deposition on the* downsroke if the substrate starts above the subphase

The vast majority of amphiphilc molecules deposit in a "head to head and tail to tail" fashion resulting in a so-called Y-type film. Other film types also exist. They are X-type, Z-type and mixed Y-type. X-type films result from the first layer depositing with the tails attached to the surface and subsequent layers depositing in a head-to-tail fashion. Z-type films are similar but the heads attach to the surface. Y-type films have a head-to-head and tail-to-tail structure regardless of how the first layer deposits. Currently there is little understanding as to why molecules deposit as X- and Z-type. Films of these structures can, however, be useful in the field on non-linear optics because of their non-centrosymmetric structure. It is also possible to produce alternating Y-type films. Such films can be produced by using one type of molecule on the first layer and a different type of molecule on the second layer. The pattern is then reproduced through out the film as the layers are deposited. An alternating trough, where the bath is partitioned in two, is required to make such a film. This enables the subphase on one side of the bath to be covered with one type of molecule while to the other side is covered with a different molecule. The dipping then occurs on alternating sides of the bath to produce to so-called alternating Y-type film.

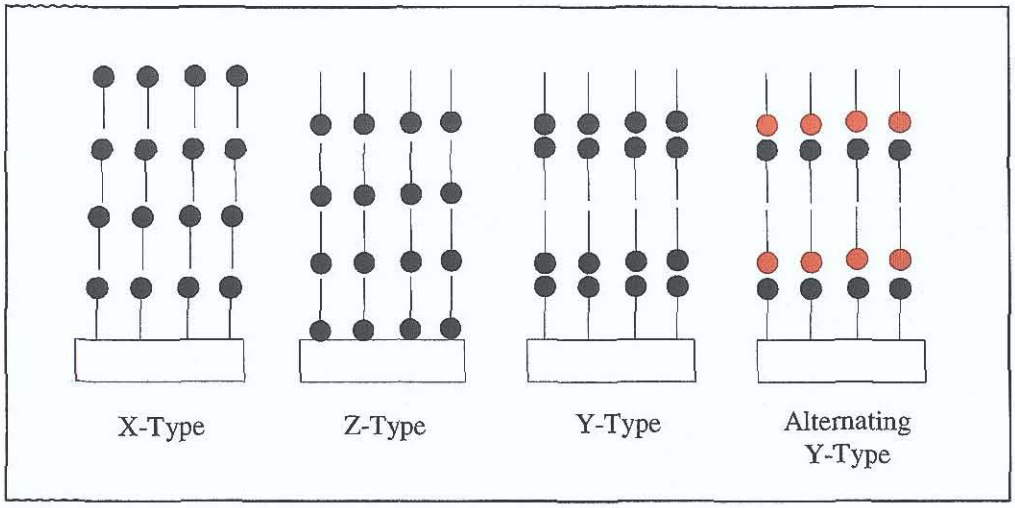

Figure 2.7 : X-, Z- and Y-type layer films as well an alternating Y-type layer.

2.1.5 Transfer ratios

The ***transfer ratio*** is the percentage of the substrate covered by the film and is defined as the area of molecules removed from the subphase at constant pressure divided by the area of the substrate immersed in water. Ideally this value should be 100% but this is rarely achieved for several reasons: (i) the target pressure may be incorrect and the film may be collapsing; (ii) if the water level in the bath is too low or the barriers are not attached to the bath properly then it is possible for the molecules to leak under the barrier. This in turn leads to unstable pressures or (iii) the molecules may be unsuitable for deposition and dissolve into the subphase if they do not possess enough amphiphilic character.

Cleanliness of the bath, subphase and substrate are vital for achieving good transfer ratios. If any of these are contaminated then the film will not deposit properly. The film then transfers to the substrate and subsequently peels off again. Complete or partial peeling of the film is observed when one layer goes on at 100% and the next layer goes on with significantly lower or negative transfer ratio. Therefore care should be taken when interpreting transfer ratios as poor transfer ratios can indicate that there is a problem with the cleanliness of the substrate, the subphase or both [2].

2.2 Scanning Tunnelling Microscopy

2.2.1 Introduction to STM

The ***scanning tunnelling microscope (STM)*** was invented by Binning and Röhrer in 1981 for which they won the Nobel Prize in 1986 [4]. The STM is a non-optical microscope used to study surfaces on an atomic scale. The principles of quantum mechanics are employed as an atomically sharp tip (often containing a single atom at its apex) is brought into close proximity to a conducting surface. When a voltage is applied between the tip and the sample electrons "tunnel" between the tip and sample, or sample and tip depending on the polarity, resulting in a weak electrical current (~1nA). Samples need to be either conductors or semi-conductors if they are to be studied by STM. It is found that the strength of the current varies exponentially with the distance between the tip and sample; the closer the tip is to the sample the stronger the current. By measuring the current as the tip scans across the sample a topographical image of the surface can be obtained.

2.2.2 Quantum Tunnelling

In STM the electron wavefunction, must penetrate a potential barrier in order to generate a tunnelling current The potential barrier is the gap between the tip and sample as shown in Figure 2.8. Both the tip and the sample are assumed to have the same work function, φ. In this case there is a positive voltage on the tip and thus negatively charged electrons flow or "tunnel" from the sample to the tip. The wavefunction of the electrons is shown as a solid line and it can be seen that it drops off a few nanometers outside the surface.

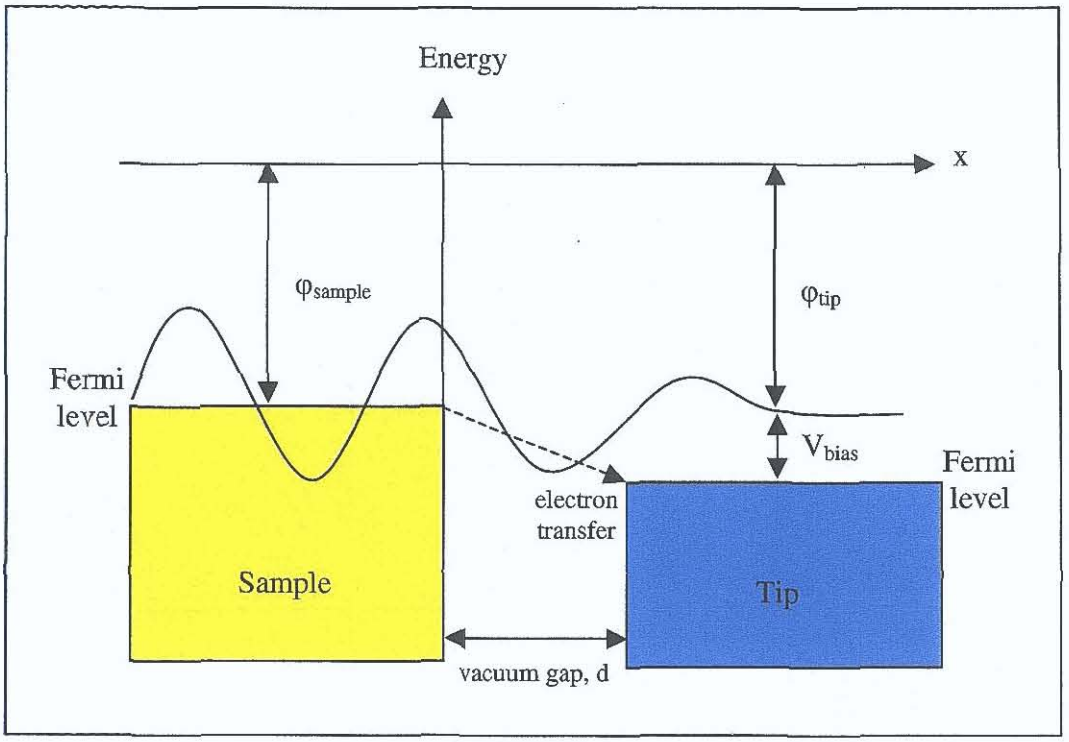

Figure 2.8: The energy level diagram showing electron tunnelling between the tip and the sample in STM.

The tunnelling current (I) depends exponentially on the distance between the tip and the sample (d) and the work function of the sample (φ).

$$I(d) = C\exp^{(-d\sqrt{\varphi})} \tag{2.11}$$

where C is a constant which depends on the joint density of states in both the sample and the tip.This is a simple one-dimensional description of the tunnelling current. In reality a more complicated description of the tunnelling current is called for [5]. The tunnelling current then becomes:

$$I = (2\pi e/h)e^2V\sum_{\mu,\nu}\left|M_{\mu,\nu}\right|2\delta(E_\nu - E_F)\delta(E_\mu - E_F) \tag{2.12}$$

where E_F is the Fermi energy, E_μ is energy of the state ψ_μ in the absence of tunnelling and $M_{\mu,\upsilon}$ is the tunnelling matrix element between states ψ_μ of the tip and ψ_υ of the sample. The matrix element $M_{\mu,\upsilon}$ is given by:

$$M_{\mu,\nu} = (h^2/2m)\int dS(\psi_\mu^*\nabla\psi_\nu - \psi_\nu\nabla\psi_\mu^*) \tag{2.13}$$

where dS is a surface element of tip. If the STM tip is spherical, the tunnelling current I, becomes:

$$I \approx 32\pi^3 h^{-1} e^2 V \phi_0^2 D_t(E_f) R_t^2 k^{-4} e^{2kR_t} \sum |\psi_v(r_0)| 2\delta(E_v - E_F) \qquad (2.14)$$

where φ_0 is the work function and $D_t(E_F)$ is the density of states at the Fermi level per volume of the tip [5]. Therefore at the centre of the tip the tunnelling current is proportional to the local density of density of states at the Fermi level. As a result the STM images are directly related to the electron states at the surface and subsequently the resolution of the images is on an atomic scale.

2.2.3 Scanning Tunnelling Spectroscopy

Scanning Tunnelling Spectroscopy (STS) is preformed by bringing an STM tip into close proximity to a conducting sample whereby there is an overlap of the electron wave functions of the tip and sample. If the tip and sample are ideal conductors with work functions of φ_t and φ_s respectively, have equal Fermi levels and no voltage is applied to the sample then no electrons will tunnel between the tip and sample, figure 2.9 (a). If, however, a positive voltage bias is placed on the sample, as shown in figure 2.9 (b) then a tunnelling current will be established. Electrons can now flow from the tip into the unoccupied (empty) states of the sample. It is also possible for electrons to flow from occupied (filled) states of the sample to the tip by placing a negative bias on the sample. The **Density of States (DOS)** of a molecule can be investigated by closely analysing the tunnelling current *(I)* as a function of the applied bias voltage *(V)*, or *I(V)* curves.

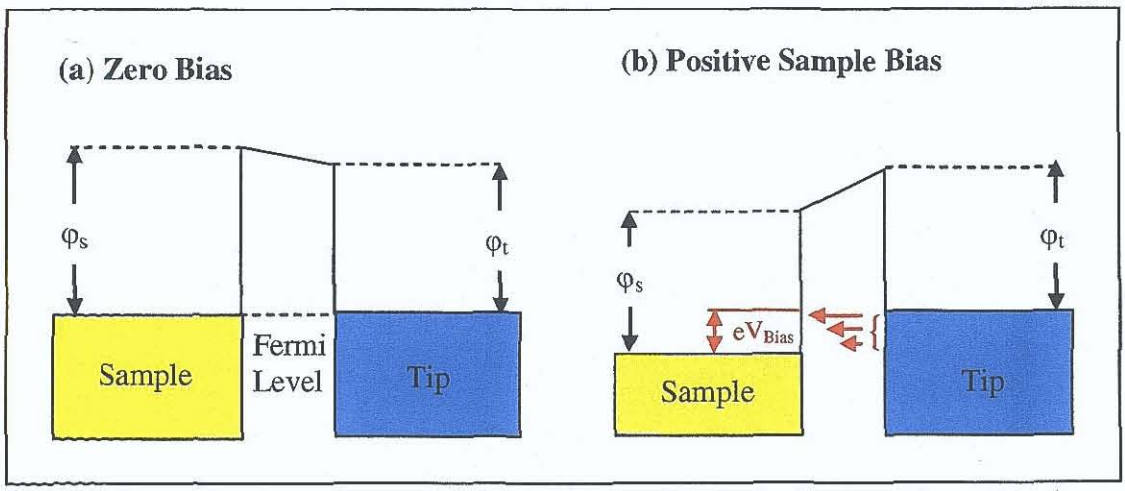

Figure 2.9 : (a) No voltage difference between the sample and tip. (b) A positive voltage is applied to the sample inducing a flow of electrons from the tip to the empty states of the sample.

The tunnelling current, *(I)*, is given by

$$I \propto \int_0^{eV} n_t(\pm eV \pm E) n_s(E) T(E, eV) dE \qquad (2.15)$$

where eV is the over all shift in the Fermi energy levels as electrons tunnel, n_t is the density of the electronic states of the tip, E is the electronic energy based on the Fermi state of the sample, n_s is the density of the electronic state of the sample and T(E,eV) is the transmission coefficient [6]. Electrons near the Fermi level are more likely to tunnel across the barrier gap and therefore have a higher transmission coefficient than those further away from the Fermi level. This is illustrated in figure 2.9(b) by the arrows of differing sizes.

Numerous experimental methods can be used to probe the DOS of molecules. For instance *I(V)* curves may be measured at a constant tip-sample separation or *z(V)* curves measured at a constant current with a variable tip-sample separation. For this research *I(V)* spectra were recorded at a constant tip-sample separation thereby eliminating the *1/V* background. This background prevents investigations of the electronic structure near the Fermi level and is a result of *dI/dV* diverging toward *1/V* as *V* approaches zero. With the *I/V* background eliminated it is possible to probe the electronic density of state by normalising the differential conductance *(dI/dV)* to the total conductance *(I/V)*. In this work both *I(V)* and *(dI/dV)/(I/V)* were measured for CuTTBPc on silver terminated silicon as discussed in chapter 6.

2.3 Atomic Force Microscopy

2.3.1 Introduction to Atomic Force Microscopy

Atomic force microscopy (AFM) is an increasingly important tool in the analysis of surface topography and surface mechanical properties. Binning, Rohrer, Gerber and Weibel developed the Scanning Tunneling Microscope (STM) in 1981 [7]. The AFM was a later development of the STM technique by Binning, Quate and Gerber [8]. The basic operating principle of the AFM involves rastering a sharp tip attached to a cantilever, across a surface. Laser light reflected off the back of the cantilever as it follows the contour of the surface, "maps" out the surface

topography. The AFM can operate in three different modes, contact mode, non-contact mode and tapping mode. In order to explain the operation of the AFM both the contact and tapping mode are discussed.

2.3.2 Contact Mode AFM

The AFM tip is positioned by a piezoelectric scanner, which expands and contracts linearly with an applied voltage. As the cantilever and tip are attached to the piezoelectric scanner they follow the motion of tube scanner. The x and y voltages control the movement of the tip in the lateral direction, while the z voltage controls the movement of the tip in the vertical direction. In contact mode the tip scans across the sample surface and changes in the cantilever deflection are monitored with a split photodiode detector, as shown in figure 2.10.

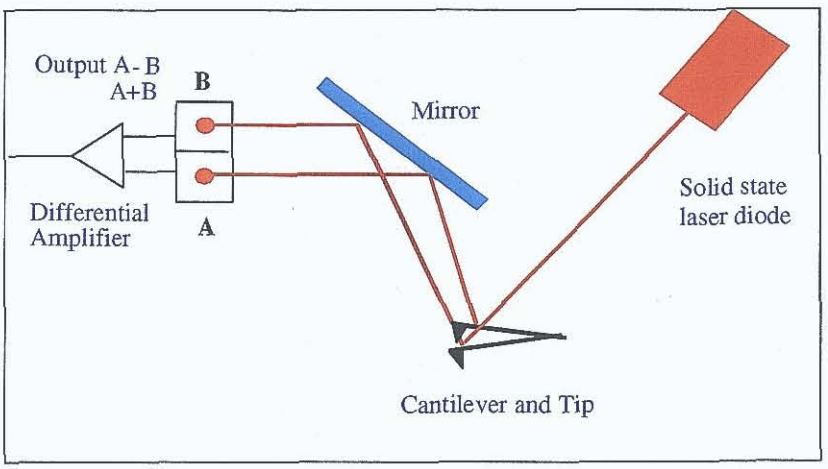

Figure 2.10: The laser beam is reflected off the back of the cantilever onto the photodiodes. Displacement of the cantilever results in one diode collecting more light than the other producing an output signal.

A feedback loop (discussed below) maintains a constant deflection between the cantilever and the sample by vertically moving the scanner at each (x, y) data point to maintain a "setpoint" deflection [9]. The setpoint deflection controls the amount of force the tip applies to the sample. The force between the tip and sample is held constant by maintaining a fixed cantilever deflection. Due to the displacement of the cantilever one photodiode may receive more light than the other. The difference between the photodiode signals divided by their sum produces a signal proportional

to the cantilever deflection. The feedback loop for the AFM acts to maintain a constant deflection during operation and the z position of the scanner is adjusted to

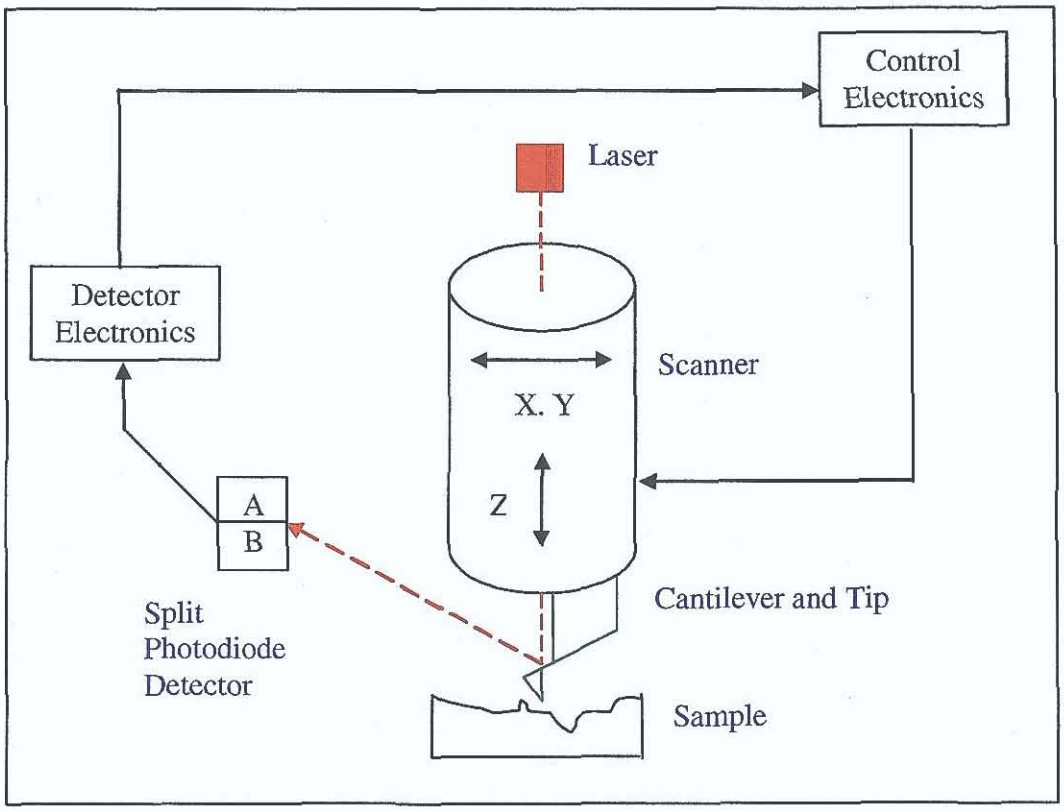

maintain this condition. The feedback loop for contact mode is shown below in figure 2.11. The vertical distance the scanner moves at each (x, y) data point is stored in the computer to form a topographic image of the sample surface.

Figure 2.11: Schematic of the AFM (in contact mode) where the feedback loop keeps the deflection of the cantilever constant. In doing so the scanner must move in the Z direction, this movement is used to produce an image of a surface.

2.3.3 Tapping mode AFM

In tapping mode the likelihood of the tip damaging the surface is reduced as the tip only taps across the sample rather than maintaining contact. Before the tip interacts with the surface its resonant frequency is found by exciting it with a second piezo mounted on the end of the scanner, which is attached to the cantilever and tip. The amplitude of the oscillation remains constant while the tip is far from the sample. When the tip interacts with the sample there is a change in amplitude. In tapping mode the feedback loop acts to maintain a constant oscillation amplitude by

adjusting the height of the tip above the surface, so that any change in amplitude is related to the surface topography. Variations in surface composition can also be mapped out by monitoring the change in phase between the drive frequency and the tip as it scans different regions. This is illustrated in figure 2.12.

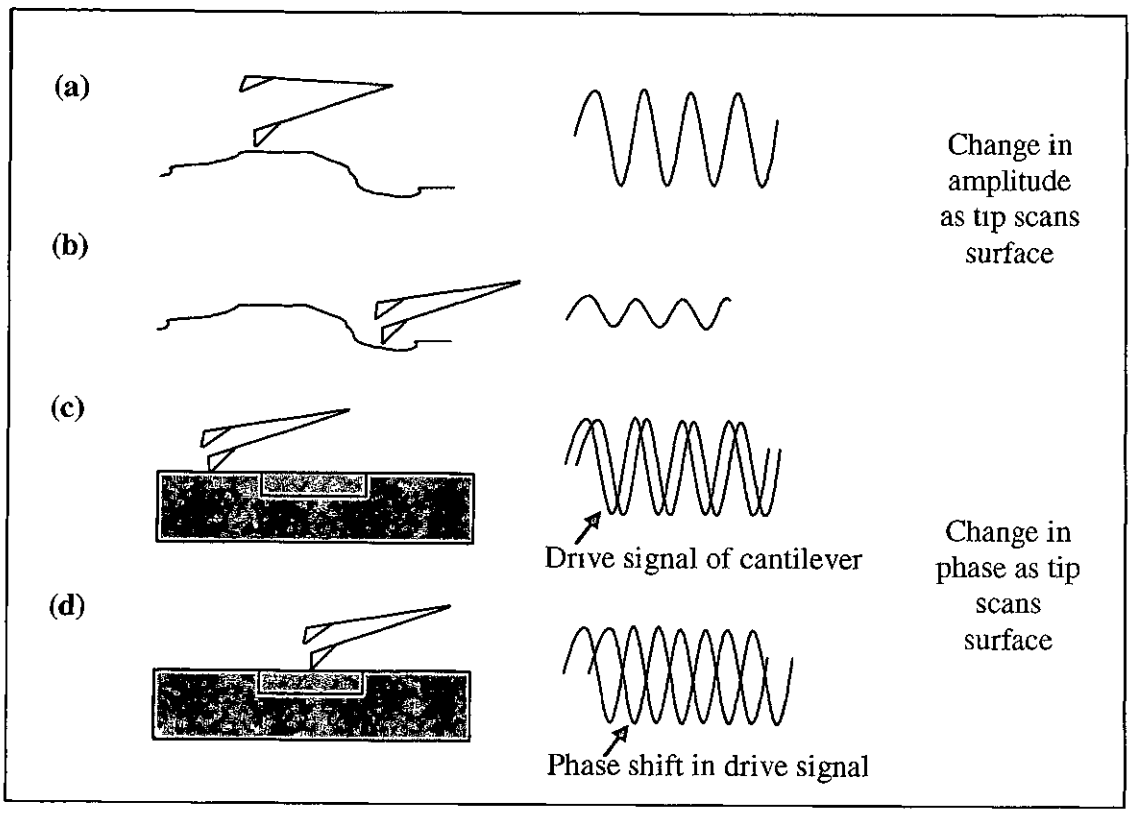

Figure 2.12: The changes in tip amplitude (part (a) and (b)) and phase (part (c) and (d)) during scanning in tapping mode.

In figure 2.12, part (a), the tip encounters a surface which has the same composition as that in part (b). The tips taps the surface at some point in (a) and the amplitude at that point is monitored. As the tip moves along there is a change in height on the surface (part (b)) resulting in a change in amplitude of the tip. In part (c) and part (d) the sample is of constant height but its composition changes. There is no change in the amplitude of vibration of the tip since the height is constant. However, there are changes in the phase of the oscillation due to variation in the

force of interaction. Monitoring the phase change produces an image related to the compositions on the surface.

2.4 Ellipsometry

2.4.1 Introduction to Ellipsometry

Ellipsometry is a non-destructive optical method used in the analysis of thin films, surfaces and material microstructure. In 1810 Malus observed polarised light for the first time[10] and in 1890 Drude took the first measurements to calculate film thickness by using the phase difference between two mutually perpendicular beams. Ellipsometry is based on measurements of the change in the polarization state of light reflected from a sample. The reproducibility and precision of this technique is high since ratios rather than absolute values are measured. In ellipsometry the change in phase and amplitude of the elliptically polarized beam is used to determine the film thickness, refractive index, extinction coefficient, surface roughness, interfacial regions, composition, crystallinity, anisotropy and uniformity of thin films [10].

2.4.2 Fresnel Reflection Coefficients and Brewster Angle

In ellipsometry linearly polarised light interacts with the sample. This interaction changes the light from linear polarisation to elliptical polarisation. In polarisation measurements only the electric field is of interest. The electric field vector, E has two components, E(x) and E(y), and the resultant vector can be at any angle or orientation. When the light waves propagate in the same direction, and are in phase with their E-vectors at right angles a linear polarised wave results. Circular polarised light results if E(x) and E(y) have the same amplitude and direction but are 90° out of phase. Elliptical polarized light results when E(x) and E(y) have different amplitudes and phases [12].

In ellipsometry linear polarised light is incident on the sample at an oblique angle,θ. The incident light has electric field components of E_p and E_s which are parallel and perpendicular respectively to the plane of incidence. For angles of incidence between 0° and 90° the p- and s-components have different reflection

coefficients. When linear polarised light interacts with the sample the p- and s-components experience a phase and amplitude shift. The change in polarisation is measured in terms of psi (Ψ) and delta (Δ). Δ provides information about the changes in phase while Ψ provides information about the amplitude change [11].

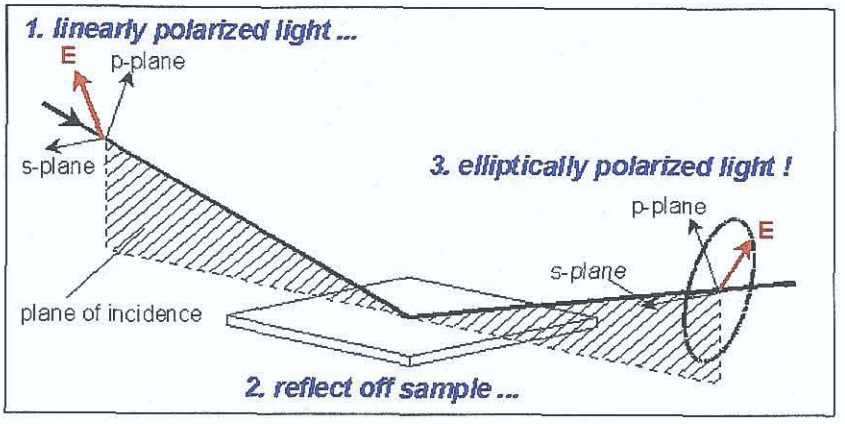

Figure 2.13: Linearly polarized light reflects off a sample changing linear polairsed light to elliptically polarised light. Both the incident and reflected beams lie in the same plane[12].

The ***Fresnel Reflection Coefficients***, $\mathbf{R_p}$ and $\mathbf{R_s}$ are related to the Ψ and Δ values by the following equation [10]

$$\rho = R_p/R_s = \tan(\Psi)e^{i\Delta} \qquad (2.16)$$

where **ρ** is the ***Ratio of the Fresnel Reflection Coefficients***. This ratio gives the ellipsometry technique its high accuracy and precision as absolute values are not required.

Another advantage of ellipsometry is that the measurement does not depend on the intensity of the incident light. The measurements depend only on the changes in polarization of the light (i.e. changes in the values of Ψ and Δ). In figure 2.14 the light has the same polarization (Ψ and Δ values) in both cases but the size of the ellipse or its intensity is different.

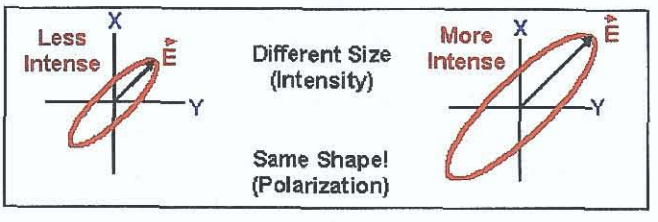

Figure 2.14: In ellipsometry the intensity of the light does not effect measurements [12].

If the R_p and R_s values are plotted as a function of the angle of incidence then at a certain angle the R_p values is at minimum. At this angle the difference between the R_p and R_s values is a maximum. The angle at which this occurs is called the ***Brewster Angle***, θ_B and ellipsometry measurements are most sensitive to film characteristics at this angle [13]. Figure 2.15 gives examples of the Brewster Angle for silicon dioxide and aluminum.

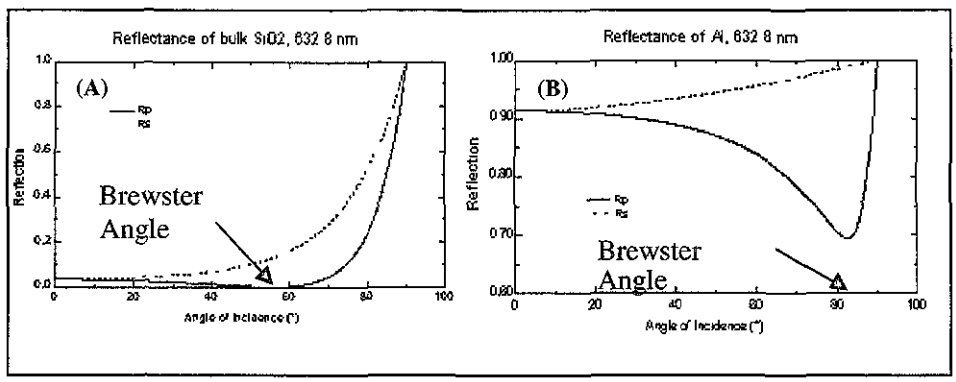

Figure 2.15: The Brewster Angle is the angle at which the Rp value reaches a minimum while the Rs value continues to increase. The difference between the Rp and Rs values is at a maximum and this angle. (a) is silicon dioxide and (b) is aluminum [13].

The Brewster angle is also related to the refractive index.

$$\tan\theta_B = n_2/n_1 \tag{2.17}$$

where n_1 and n_2 are the refractive indices of air and the substrate or of the thin film and substrate respectively. If graphs of R_p/R_s and Ψ/Δ versus angle of incidence are compared then it can be seen that the Δ value drops from 180° to 0° at the Brewster angle. Maximum sensitivity of the ellipsometer is achieved when the Δ value is set to 90°.

2.4.3 Interaction with a Solid Substrate

If a substrate is composed of layers then the substrate and each of the layers have their own Brewster angle. The ***Pseudo-Brewster*** angle is the angle at which measurements are be taken for any layered substrate. The presence of layers or a thin film introduces interference in the reflected and transmitted light. Each reflected wave has its own phase and amplitude. The refractive index, extinction coefficient

and thickness of the film determine the reflected and transmitted intensities, phase change, and refraction angle. For a material containing a substrate and a film the thickness of the film can be calculated. For thin films the R_p and R_s components are

$$R^p = \frac{r_{01}{}^p + r_{12}{}^p e^{-i2\beta}}{1 + r_{01}{}^p r_{12}{}^p e^{-i2\beta}} \tag{2.18}$$

$$R^s = \frac{r_{01}{}^s + r_{12}{}^s e^{-i2\beta}}{1 + r_{01}{}^s r_{12}{}^s e^{-i2\beta}} \tag{2.19}$$

where r_{01} is the reflection from the thin film to air, r_{12} is the reflection from the substrate to the thin film and β is the phase thickness [10]. The reflections and transmissions which take place in a thin film are shown in figure 2.16.

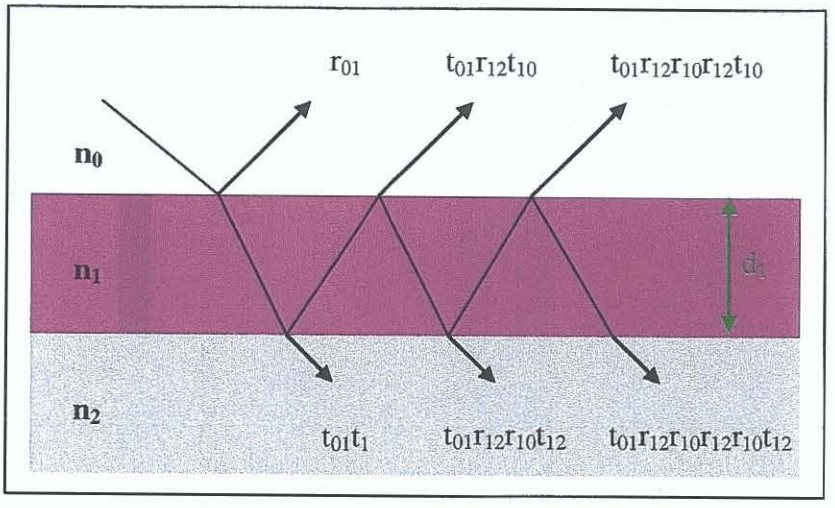

Figure 2.16: The various transmissions and reflections which occur in a thin film

When the ratio of R_p to R_s is known β, the phase thickness, can be determined and this is then used to calculate the film thickness d_1, if the refractive index of the film n_1, is known. The equation for calculating film thickness, at a wavelength, λ, is [10]

$$\beta = 2\pi\left(\frac{d_1}{\lambda}\right) n_1 \cos\theta_1 \tag{2.20}$$

2.5 X-Ray Photoelectron Spectroscopy

2.5.1 Introduction to XPS

X-Ray Photoelectron Spectroscopy (XPS) is carried out in an ultra high vacuum environment, where the sample to be analysed is irradiated with X-ray photons. XPS is used to study the chemical and electronic structure of solids and is based on a "photon in-electron out" process When a photon impinges upon an atom in the solid, one of three events may occur, (i) the photon can pass through with no interaction; (ii) the photon may be scattered by an orbital electron leading to partial energy loss or (iii) the photon may interact with an atomic orbital electron with total transfer of the photon energy to the electron, leading to electron emission from the atom. The third event describes the photoemission process that is the basis of XPS [5].

2.5.2 The Photoemission Process

Total transfer of the photon energy to the electron is the essential element of photoemission. In XPS the photon is absorbed by an atom in a molecule leading to ionization of the molecule and the emission of a photoelectron [4]. The kinetic energy, E_{kin}, of the photoelectron is given by

$$E_{kin} = h\upsilon - E_B - \phi \qquad (2.21)$$

Where $h\upsilon$ is the energy of the photon, E_B is the binding energy of the electron and ϕ is the work function of the material. The photoemission process is shown schematically in figure 2.17.

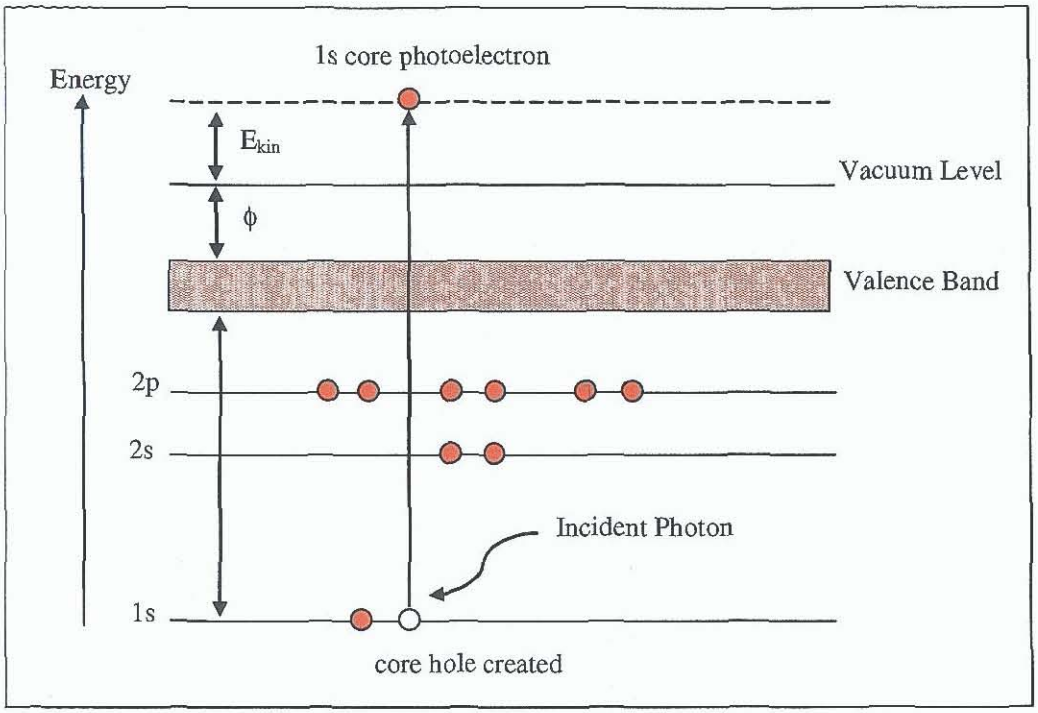

Figure 2.17: A photon impinges on a 1s core electron with a total transfer of energy resulting in a 1s core photoelectron.

Both core levels and valence bands can be studied using XPS. Each element has it own unique core level spectrum making it possible to carry out chemical identification. The valance band electrons are directly involved in bond formation and changes in chemical environment may give rise to chemical shifts in the spectrum. The electronic properties of the material can be determined by studying the valance band spectrum The position of the highest occupied molecule orbital (HOMO) and the tilt angle of a molecule can be determined by studying photoemissions from the valance band.

2.5.3 Inelastic Mean Free Path

When photons interact with electrons elastic and inelastic collisions take place as the excited electrons are ejected from their orbitals. In an elastic collision the ejected electron does not lose any energy when it is involved in a collision with an atom. In an inelastic collision the electron loses a fraction of its energy in a collision. Inelastic collisions may occur as the emitted electrons make their way out of the sample and into the detector. These scattered electrons contribute to a

background in the spectrum. XPS focuses on the elastically scattered electrons which have characteristic energies for that material and contribute to the peaks in the spectra used for analysis of the composition of the material. Elastically scattered photoelectrons from the core levels (1s, 2s, ,2p etc.) contribute to the formation a core level spectrum. Inelastic collisions are responsible for the decay in intensity after the electron beam has traveled a distance, d, in a solid. The decay follows a first-order exponential and is given by

$$I(d) = I_0 \exp(-d/\lambda) \tag{2.22}$$

Where I(d) is the intensity of the electron beam after is has traveled a distance d in the material, I_0 is the initial beam intensity and λ is the ***Inelastic Mean Free Path (IMFP)***. The IMPF is the mean distance traveled by an electron in a solid before it is inelastically scattered. Small inelastic mean free paths mean that the electrons only travel a short distance before colliding with other electrons and are scattered. This makes the distance d, small and hence the surface sensitivity is high. A plot of the IMFP for metals versus electron energy is shown in figure 2.18.

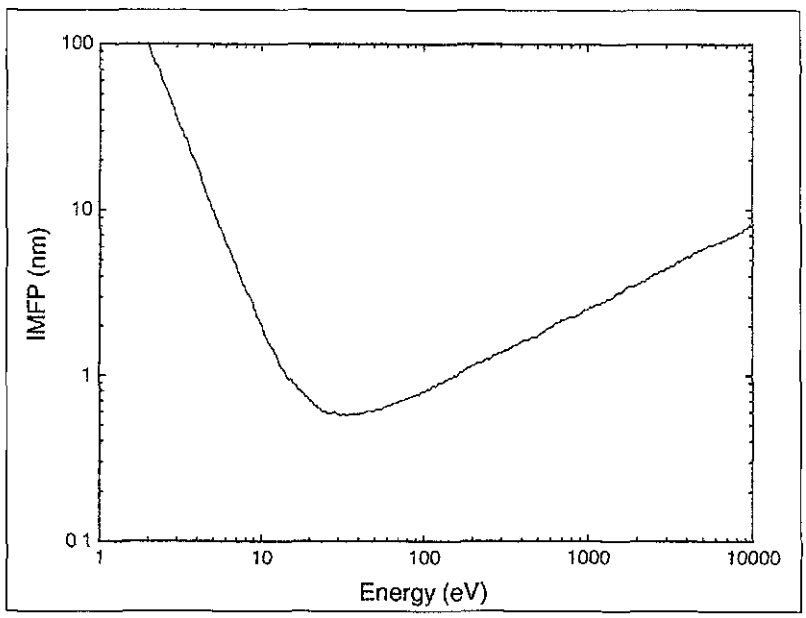

Figure 2.18: Universal Inelastic Mean Free Path versus kinetic energy for solids [14].

Plasmons are produced when electrons collide with those electrons found in the valence/conduction band of the solid resulting in a quantised electron density oscillation Below 30 eV it is found that the electrons do not possess enough energy

to excite ***plasmons***. Between ~50-100 eV the IMFP is at its minimum meaning that the surface sensitivity is at it greatest. Beyond this value the electrons have a higher energy and travel faster, therefore reducing the amount of time the electron spends in the sample. This reduces the possibility of any energy loss.

2.5.4 Shake-up Satellite Peaks

The XPS spectrum not only consists of peaks due to core level emissions but also contains shake-up satellite peaks. These peaks are a result of photoelectrons losing energy by promoting valence electrons from an occupied energy level to an unoccupied higher level. During normal photoelectron emission a photon impinges on a core electron and the electron is emitted with an energy of $h\upsilon$-E_B with no loss of energy. However, if that electron collides with a valence band electron and an energy loss of ΔE occurs the emitted photoelectron (or shake-up satellite) will have an energy of $h\upsilon$-E_B-ΔE The shake-up satellite peaks are therefore found at lower kinetic energies than the core level peaks. The process is shown in figure 2.19.

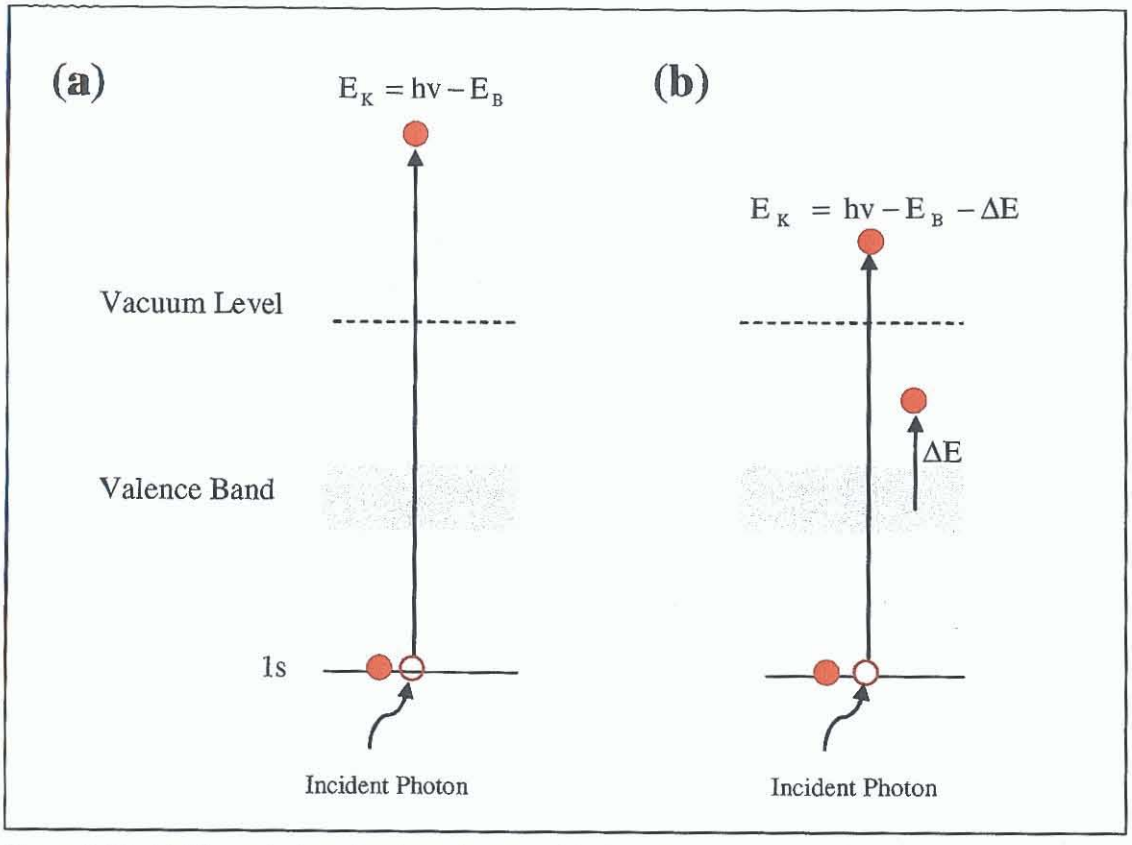

Figure 2.19: (a) The emission of a photoelectron with $E_K = h\nu - E_B$. (b) The formation of a shake-up satellite after the photoelectron collides with a valence band electron. The collision results in an energy loss of ΔE and therefore the kinetic energy of the shake-up satellite is $h\nu - E_B - \Delta E$.

The electronic structure of copper in its ground state is $[Ne]3s^2 3p^6 3d^{10} 4s^2$. There are three possible excitations involving the 3d electrons and a 4s electron. The first process involves the direct photoemission of one of the 3d electron according to [15]

$$3p^6 3d^{10} 4s^1 + h\nu \rightarrow 3p^6 3d^9 4s^1 + e^- \qquad (2.23)$$

Figure 2.20 illustrates the direct excitation of the 3d electron.

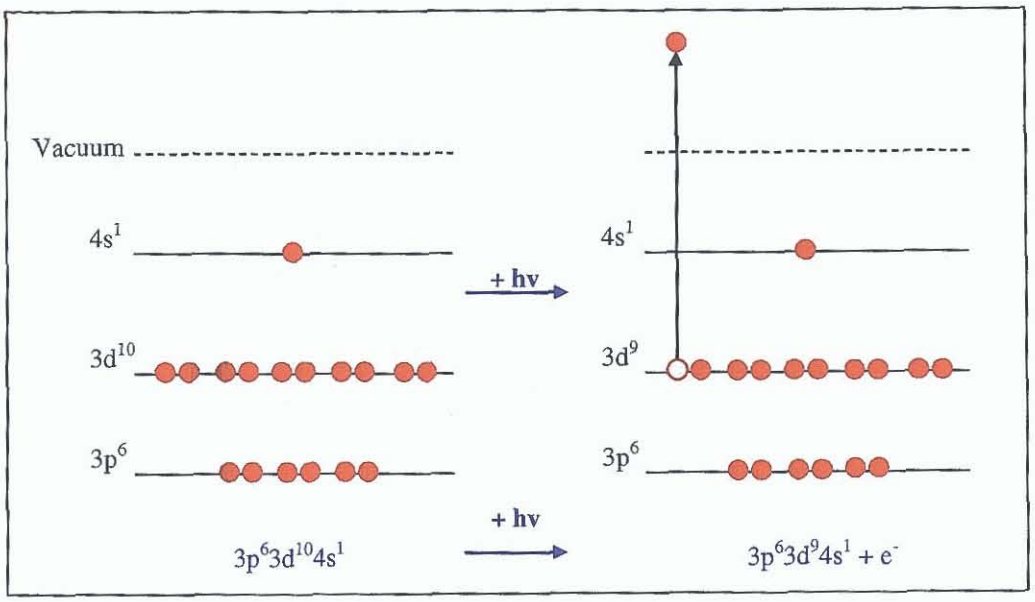

Figure 2.20: The one-electron photoemission process exciting the 3d electron.

The second process involves the formation of a 3d shake-up satellite which occurs after a 3d electron is emitted and a second 3d electron is promoted into the 4s energy level. This two-hole shake-up is shown in figure 2.21 and is represented by [15]

$$3p^6 3d^{10} 4s^1 + h\nu \rightarrow 3p^6 3d^8 4s^2 + e^- \qquad (2.24)$$

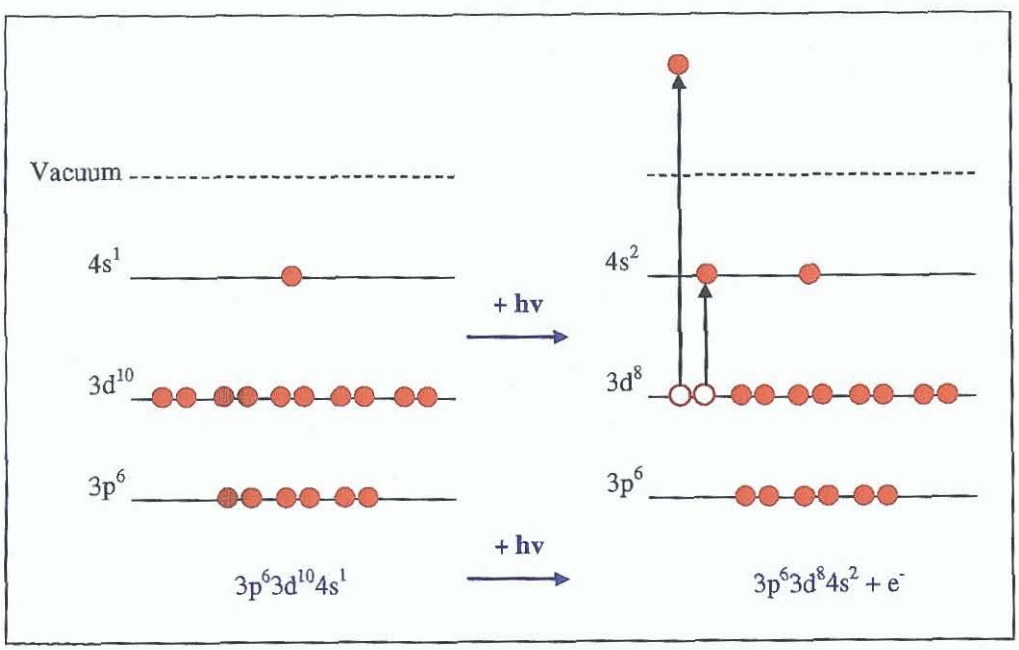

Figure 2.21: The two hole shake-up where one 3d electron is emitted from the sample, while the other 3d electron is promoted into the 4s energy level.

The third excitation process involves a transition from the 3p to the 4s level followed by a simultaneous Auger decay. The process is shown in figure 2.22 and is represneted by:

$$3p^6 3d^{10} 4s^1 + h\nu_{res} \rightarrow 3p^5 3d^{10} 4s^2 \leftrightarrow 3p^6 3d^8 4s^2 + e^- \quad (2.25)$$

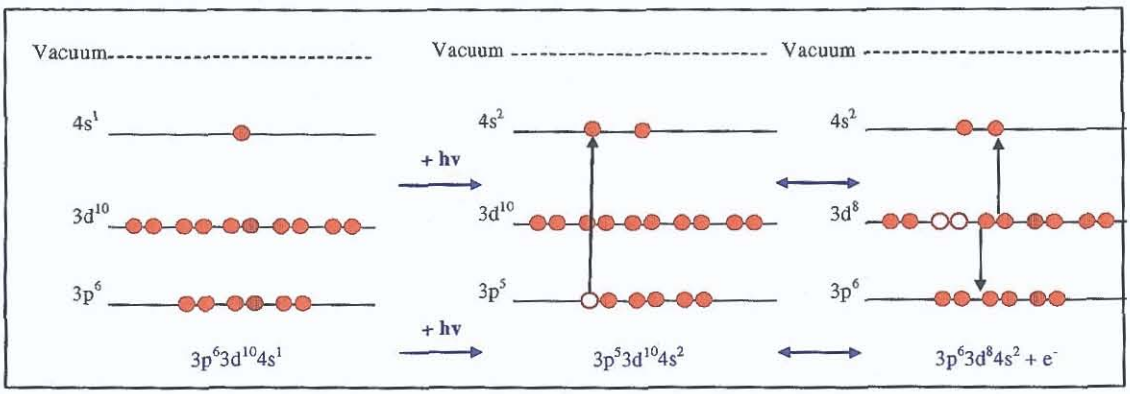

Figure 2.22: The Auger decay associated with the promotion of a 3p electron to the 4s energy level.

2.6 Near Edge X-ray Absorption Fine Structure

2.6.1 Introductions to NEXAFS

The NEXAFS technique is used to probe the orientation of molecules on surfaces. Extended X-ray absorption fine structure (EXAFS) was the precursor to NEXAFS. Initially the NEXAFS part of the EXAFS spectrum was discarded as it was thought to be too complicated to analyse. The first calculations of the NEXAFS structure of molecules were carried out by Dehmer and Dill in 1975 [16]. Today NEXAFS is a standard technique in surface analysis. NEXAFS was used in this work to determine the orientation of the CuTTBPc molecule on silicon substrates.

2.6.2 NEXAFS process

Beer's Law describes the absorption of photons in a medium [5] by

$$I(x) = I_o \exp^{(-\mu x)} \quad (2.26)$$

where I_o is initial photon intensity I(x) is intensity at a distance x into the medium and μ is the absorption coefficient. X-ray photons have the ability to excite core electron into the empty valence states or into the ionisation states. The transition of

the electrons from their initial to final states can be observed by studying the absorption coefficient as a function of photon energy, as shown in figure 2.23. The presence of absorption edges at certain energies lead to a sharp increases in the absorption coefficient due to new X-ray absorption channels opening up in the material. There is a decrease in the X-ray absorption as the photon energy increases. The energy region close to the absorption edge is called the ***Near Edge X-Ray Absorption Fine Structure (NEXAFS)*** region. Above these edges there is an oscillation in the absorption signal and this region is known as the ***Extended X-Ray Absorption Fine Structure (EXAFS)*** region.

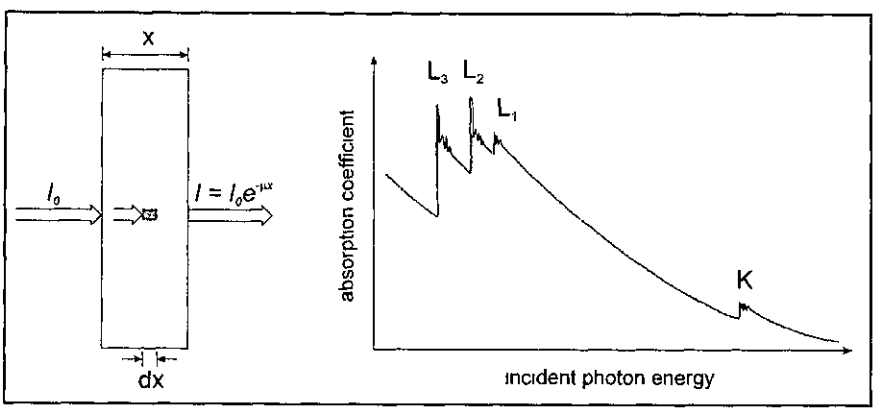

Figure 2.23: Beer's Law is shown on the left hand side of the image, while the absorption coefficient as a function of photon energy is shown in the right hand side [17].

The NEXAFS region is used to study the orientation of molecules on a surface. The orientation is calculated by studying the intensity of peaks corresponding to π and σ bonds in the molecule for different angles of incidence of the radiation.

The absorption of a photon can cause the excitation of a core level electron into an unoccupied molecular state ($\pi \rightarrow \pi^*$ and $\sigma \rightarrow \sigma^*$) above the Fermi Level. The core hole created can be filled by a valence electron and the excess energy is given off either by the emission of an Auger electron or by a fluorescent photon. The process is shown below in figure 2.24.

Fluorescent photon emission is known as a radiative event and Auger photon emission is known as a nonradiative event. The fractions of the radiative and

nonradiative decay rates as a function of the total decay rate are given by the formula:

$$\omega_a + \omega_f = 1 \tag{2.27}$$

where ω_a is the Auger yield and ω_f is the fluorescent yield. From the K-shell excitations of low-Z atoms, the Auger event occurs over a shorter timescale and so is found to dominate. ***Total yield experiments (TEY)*** were carried out whereby the spectrum contained a photoemission derived signal and an Auger derived signal at each incident photon energy

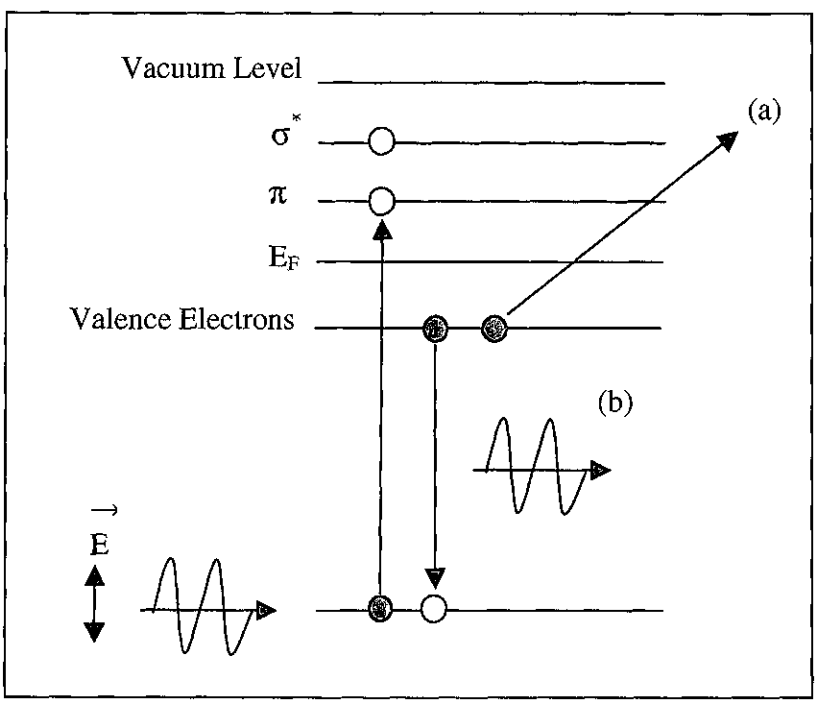

Figure 2.24: The absorption of a photon can cause the excitation of a core electron resulting in the formation of an Auger electron (a) or a fluorescent photon (b).

2.6.3 Determination of molecular orientataion

An excited CuTTBPc molecule contains a number of aromatic bonds which consists of highly directional π^* and σ^* molecular orbitals. It is found that the π^* molecular orbital is aligned perpendicular to the plane of the aromatic ring, while the σ^* lies in the parallel direction [18] as shown in figure 2.25.

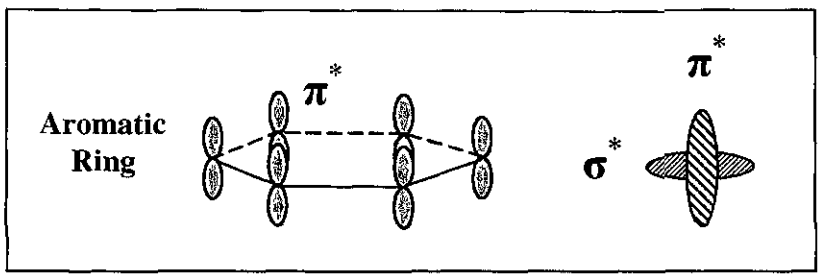

Figure 2.25: The orientation of the π* and σ* molecular orbitals in an aromatic ring.

The probability of exciting an electron from the core level to an unoccupied molecular orbital is given by [18]:

$$I \propto \left|\langle f|\underline{\mathbf{e}} \bullet \underline{\mathbf{p}}|i\rangle\right|^2 \propto \frac{1}{|\underline{\mathbf{E}}|^2}\left|\langle f|\underline{\mathbf{E}} \bullet \underline{\mathbf{p}}|i\rangle\right|^2 \propto \frac{1}{|\underline{\mathbf{E}}|^2}\left|\langle \underline{\mathbf{E}}|f \bullet \underline{\mathbf{p}}|i\rangle\right|^2 \qquad (2.28)$$

where I is the intensity of the resonance, f is the oscillator strength, $\underline{\mathbf{e}}$ is the unit vector, $\underline{\mathbf{p}}$ is the momentum operator and $\underline{\mathbf{E}}$ is the electric field vector. For the π^* state, where the molecular orbitals are aligned perpendicular to the plane of the aromatic ring, $\langle f|p|i\rangle$ is in the direction of the maximum orbital amplitude meaning that the probability of excitation between a 1s initial state and a π^* state is at a maximum when the electric field vector, $\underline{\mathbf{E}}$, is pointing in the same direction as the direction of the final state, then

$$\left|e \bullet \langle f|p|i\rangle\right|_v^2 \propto I_v = \cos^2\delta \qquad (2.29)$$

where δ is the angle between the E-field vector and the vector perpendicular to the plane of the final state orbital and v denotes a vector final state orbital. Similarly for the σ^* state·

$$\left|\langle f|e \bullet p|i\rangle\right|_p^2 \propto I_p = \sin^2\varepsilon \qquad (2.30)$$

where ε is the angle between the E-field vector and normal to the plane of the final state orbital and p denotes a plane final state orbital. The above two equations relate to the interaction of a unidirectional (i.e polarised) E-field with the π^* and σ^* molecular orbitals. There are two components to the E-field vector in synchrotron radiation, one in the horizontal orbital plane and one in the vertical orbital plane. If the X-ray propagates along the z-axis, then the x- and y- axes with unit vectors of $e^{\parallel}$ and $e^{\perp}$ lie in the horizontal and vertical planes respectively The electric field vector can now be described as:

$$E = E^{\parallel}\cos(kz - \omega t) + E^{\perp}\sin(kz - \omega t) \tag{2.31}$$

where $\hbar k$ is the momentum of the X-rays and ω is the frequency of the electromagnetic wave. Equation 2.27 can be altered to account for the perpendicularly oriented E-field vectors with the resultant equation being:

$$I \propto \frac{\left|\langle f|E^{\parallel}\bullet p|i\rangle\right|^2 + \left|\langle f|E^{\perp}\bullet p|i\rangle\right|^2}{\left|E^{\parallel}\right|^2 + \left|E^{\perp}\right|^2} \tag{2.32}$$

where P, the polarisation factor, characterises the intensity or energy density of the electromagnetic field in the orbit plane and is given by

$$P = \frac{\left|E^{\parallel}\right|^2}{\left|E^{\parallel}\right|^2 + \left|E^{\perp}\right|^2} \tag{2.33}$$

Using Equation 2.33, equation 2.32 can now be written as

$$I \propto P\left|\langle f|e^{\parallel}\bullet p|i\rangle\right|^2 + (1-P)\left|\langle f|e^{\perp}\bullet p|i\rangle^2\right| \tag{2.34}$$

where $\mathbf{e}^{\parallel}$ and $\mathbf{e}^{\perp}$ are the unit length vectors in the directions of $E^{\parallel}$ and $E^{\perp}$ respecively.

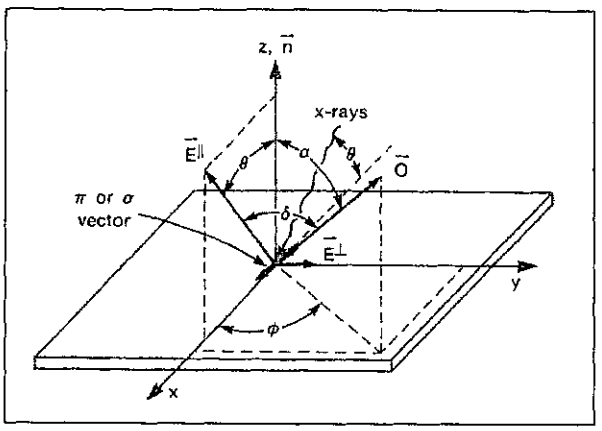

Figure 2.26: Coordinate system defining the geometry of a π^* vector orbital, , with respect to the sample surface and the incident synchrotron radiation [18].

Figure 2.26 represents the coordinate system defining the geometry of a π^* vector orbital, $\vec{O}$, with respect to the incident E-field vectors $\vec{E}^{\parallel}$ and $\vec{E}^{\perp}$, θ is the angle between the incident synchrotron radiation and the plane of the surface, α is the angle between the surface normal and the incident vector $\vec{O}$ and δ is the angle between the projections of $\vec{O}$ and $\vec{E}^{\parallel}$ onto the surface plane.

Using this coordinate system, equation 2.34 can be redefined in terms of the angles δ, α and θ. It is shown that for a surface exhibiting twofold symmetry the intensity of the π^* emission is given by [18]:

$$I \propto P(\cos^2\theta\cos^2\alpha + \sin^2\theta\sin^2\alpha\cos^2\phi) + (1-P)(\sin^2\alpha\sin^2\phi) \quad (2.35)$$

For threefold or higher symmetry the $\cos^2\phi$ averages to ½ and the intensity variance of the π^* emission can be given by:

$$I \propto P\left(\cos^2\theta\cos^2\alpha + \frac{1}{2}\sin^2\theta\sin^2\alpha\right) + (1-P)\left(\frac{1}{2}\sin^2\alpha\right) \quad (2.36)$$

Using equations 2.35 and 2.36 it is possible to deduce the orientation of the unoccupied molecular orbitals with respect to the incident synchrotron radiation. From this the tilt angle of the molecule on the substrate can be determined.

Chapter Two References

[1] **Langmuir Blodgett Film An Introduction,** Michael C. Petty, Cambridge University Press, 1996.

[2] Nima Technology, **Tensiometers and Langmuir-Blodgett Troughs**, Operating Manual, 4th Edition, 1995.

[3] **An Introduction to Ultrathin Organic Films from Langmuir-Blodgett to Self Assembly**, Abraham Ulman, Academic Press, 1991.

[4] **Surfaces**, G. Attard and C. Barnes, Oxford University Press Inc., New York, 1998.

[5] **Surface Analyisis, The Principle Techniques**, J. C. Vickerman, Wiley, 1997.

[6] **Scanning Probe Microscopy and Spectroscopy**, Methods and Applications, Rolland Wiesendanger, Cambridge University Press, 1994.

[7] G. Binning, H. Rohrer, Ch. Gerber and E. Weibel, ***Physical Review Letters***, 49 (1982) 57-61.

[8] G Binnig, C F. Quate, Ch. Gerber, ***Physical Review Letters***., 56 (1986) 930.

[9] **Scanning Probe Microscopy Training Notebook**, Digital Instruments, 1998.

[10] **Spectroscopic Ellipsometry and Reflectometry**, Harland G. Tompkins, William A. McGahan, John Wiley & Sons, 1999.

[11] **Optics**, 4th edition, Eugene Hecht, Addison-Wesley, 2002.

[12] www.jawoollam.com

[13] **Ellipsometry and Polarized Light**, Paperback edition 1987, North-Holland, 1987.

[14] M.P. Seah, W. A. Dench, ***Surface Interface Analysis***, 1 (1979) 2-11.

[15] M. Iwan, E. E. Koch, ***Solid State Communications***, 34 (1980) 57-60.

[16] J. L. Dehmer, D. Dill, ***Physical Review Letters***, 35 (1975) 213.

[17] **X-ray Absorption: Principles, Applications, Techniques of EXAFS, SEXAFS and XANES**, Konigsberger, and Prins, Wiley, New York, 1988.

[18] **NEXAFS Spectroscopy**, Joachim Stohr, Springer, 1996.

Chapter 3

Experimental Setup

The various equipments used to synthesise and probe the LB films and evaporated films are outlined in Chapter 3. LB films were produced in DCU, Ireland, and Nottingham University, UK, using two different LB baths. A description of the baths is given in section 3.1 The experimental setups of the STM, AFM and ellipsometer are found in sections 3.2, 3.3 and 3.4, respectively. XPS experiments were conducted in the Daresbury Laboratories, UK, on station 4.1. Section 3.5 describes the setup of the XPS. NEXAFS experiments were carried out on the SX700 beamline in Aarhus, Denmark. Section 3.6 details the NEXAFS experiments.

3.1 Langmuir-Blodgett Experimental Setup

3.1.1 Setup of the LB baths

Two different types of LB baths were used in this research project. A Nima 2022 bath with a circular trough was used in DCU, while a smaller rectangular Nima 312D bath was used for the films prepared in Nottingham. The troughs were constructed from Teflon and both had movable Teflon barriers, a pressure sensor (Wilhelmy Plate) and a movable dipper. The trough was filled with the chosen subphase liquid. This could be ultrapure water or, for example, solutions containing metal salts. A monolayer of the chosen molecule was spread on the surface and compressed by moving the barrier. The pressure was monitored during compression and once the correct pressure was reached a layer of film was deposited by lowering the dipper into the subphase. As the LB technique involves the study of monolayers it is vital that all external vibrations are isolated.

The Nima 2022 Model trough was placed on a granite table which had wooden blocks and foam placed under the legs to improve vibration damping. In addition wooden blocks were also placed under the legs of the LB trough. Finally, the trough sat on an inflated rubber tube to further dampen vibrations. Photographs of the Nima 2022 and 312D baths are shown in figures 3.1 and 3.2 respectively.

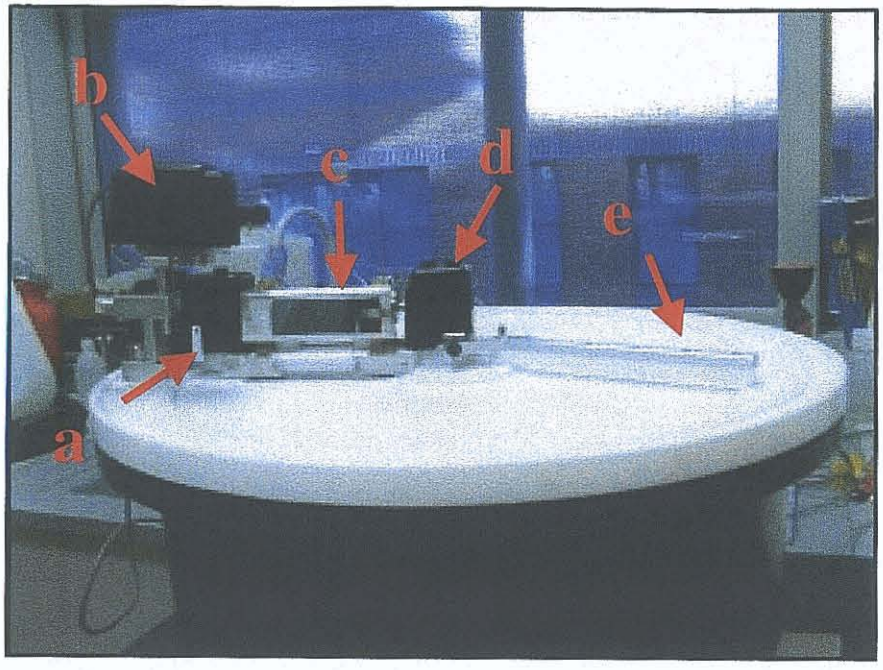

Figure 3.1: Experimental setup of the Nima 2022 LB bath where (a) is the Wilhelmy Plate, (b) is the pressure sensor, (c) is the substrate holder, (d) is the dipper mechanism and (e) is the movable barrier.

The Nima 312 D Model was smaller in size and situated in a fumehood. Its operating principle was the same as that of the Nima 2022 Model and it had the same accessories. Due to its compact size vibrations could be successfully isolated by placing foam under the legs of the bath.

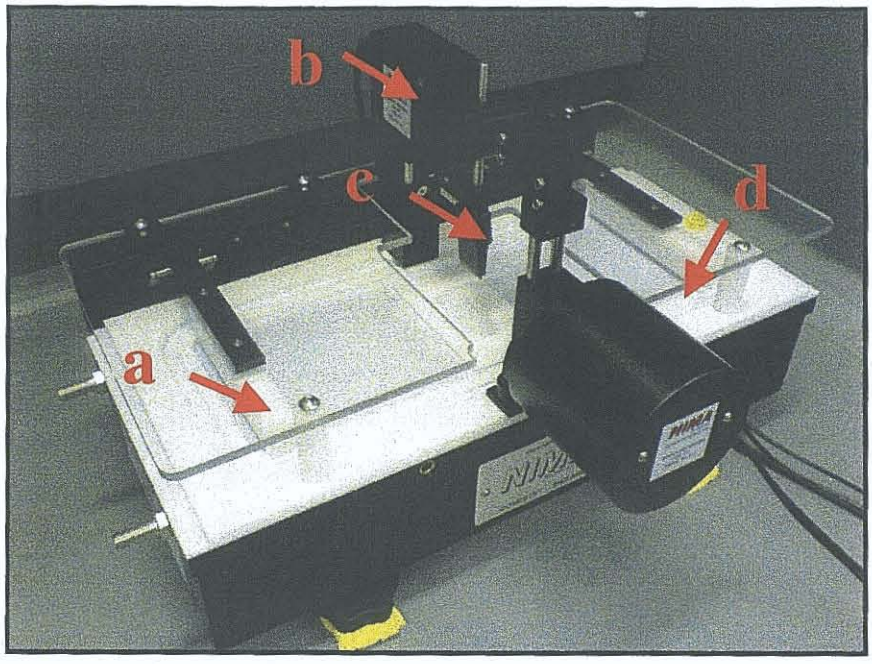

Figure 3.2: Experimental Setup of the Nima 312D LB bath where (a) is the moveable barrier, (b) the the pressure sensor, (c) is the substrate holder and (d) is the dipper mechanism.

3.1.2 Calibration Procedures

The calibration procedures are described in detail in the Operating Manual [1]. A short description of the procedures for the Nima 2022 bath are presented here. As the Nima 312D Model was new recalibration was not required.

The dipper and barrier are connected to continuous multiturn potentiometers. Through the potentiometers the position of the dipper and barrier are converted to voltages, which are then digitalized by an Analog to Digital Converter (ADC) and read by a computer. Calibration of the dipper and barrier speeds is performed automatically by the software. Typical values for the dipper and barrier speeds are shown below.

	Low speed	High speed
Dipper	0.2 mm/min	218.9 mm/min
Barrier	17.2 cm^2/min	1020.8 cm^2/min

Table 3.1 : The values obtained after calibration of the dipper and barrier.

The pressure sensor was calibrated by hanging a 100 mg mass from the sensor. If the sensor was working correctly a reading of – 49.1 mN/m should be obtained. If this

was not the case then the calibration procedure given in the manual was repeated. Errors in the calibration could arise by the moving arm of the sensor touching the sensor housing. While carrying out the calibration it was essential to minimize contamination of any of the part of the bath or any of it accessories.

The Nima 2022 Model was a circular alternate layer trough with two pressure sensors, two barriers and a dipper mechanism. All of these components were removable. The trough was also equipped with circular and domed acrylic covers, which were used to protect the trough from dust and contamination. The 312D model had a single layer rectangular trough with one pressure sensor, two barriers, a dipper mechanism and flat acrylic covers which sat about 1.5 cm above the subphase.

As the LB technique involves the transfer of monolayers onto a clean substrate it is vital that all parts of the trough are clean and free of any type of contamination, which may interfere with the making of ultra thin films. Although the troughs were of a different design they were both subjected to the same cleaning procedures. The troughs and barriers were constructed from Polytetrafluoroethylene (PTFE) which is one of the most inert and hydrophobic polymers known. Before cleaning the trough, the dipper, barriers and pressure sensors were removed. The trough was filled with a 0.1M solution of sodium hydroxide and left soaking overnight to remove any contaminants The trough was then thoroughly rinsed with Ultra pure water (Millipore, Milli Q-Plus model) with a resistivity of 18.2 MΩ-cm at 25°C to remove the sodium hydroxide and remaining contaminants. The trough was wiped out with Kimwipes (type 7105, which are surfactant free) which were soaked in chloroform (~ 99.8% pure, Sigma Aldrich, Ireland.). Finally, any excess chloroform was wiped away with Kimwipes soaked in ultrapure water to ensure that no surfactants were left in the trough. It was important to note that the filling of the bath with sodium hydroxide was only necessary when the bath was seriously contaminated or had not been used in a long time. It was normally sufficient to clean the bath with Kimwipes, chloroform and water. The Nima 312D Model was a more recent design and was cleaned with chloroform and water. The barriers were also cleaned using chloroform and water as they too were made from PTFE. After

cleaning, the individual components of the bath were reassembled and the bath was filled with ultra pure water.

3.1.3 Cleaning of the Subphase

The procedure for cleaning the subphase was the same for both baths. Ultrapure water was used as the subphase, or in the preparation of the subphase, e.g. $CdCl_2$. If there was too much water in the bath it was possible to actually push the monolayer off the surface of the subphase. On the other hand if there was not enough water in the bath the monolayer could leak under the barrier. Both extremes cause serious problems when obtaining isotherms and depositing films. To avoid these problems the bath was carefully filled with water until it almost overflowed.

Cleaning of the subphase was a relatively simple procedure involving the observation of Area-Pressure graphs. A Wilhelmy plate attached to the pressure sensor was the lowered into the subphase so that it was just submerged and its contact angle with the subphase was considered to be zero In order to eliminate drift in the pressure sensor readings the equipment was given adequate time to warm up and it was important to allow the paper plate to fully adsorb water from the subphase. The pressure reading was then zeroed in the software. The barrier was set to the fully open position and then swept to its minimum area position at a fixed speed (typically 50-100 cm^2/min). No change was be observed in the surface pressure, indicated by a flat isotherm, if the surface was free of contamination . If this was not the case then the surface was cleaned using a pipette which was attached to an aspirator pump and used to suck off any material no the surface The barrier was then reopened and the Wilhelmy plate was readjusted to zero contact angle. The surface pressure was reset to zero because a reduction in the water level changes the pressure reading. The trough required the addition of water if a large amount was removed with the aspirator pump. This cleaning procedure was repeated until the change in surface pressure was less than 0.5 mN/m. As this stage molecules could be deposited onto the surface of the subphase.

3.1.4 Preparation of Hydrophobic Substrates

Glass or silicon (purchased from Wacker–Chemitronic GMBH, Germany) could be rendered hydrophobic with the use of ***hexamethyldisilazane (HMDS,*** $C_6H_{19}NSi_2$*)*. HMDS is widely used to produce hydrophobic substrates because (i) it is an adhesion promoter, which allows for better film formation and coverage; (ii) the surface tension of the substrate is reduced by HMDS when the polar hydroxyl and oxide moieties on the substrate surface react with the trimethylsilyl groups to produce a non-polar surface monolayer [2]. HMDS works by reacting with the water molecules already present on the substrate to produce inert hexamethyldisiloxane ($(CH_3)_3SiOSi(CH_3)_3$) and ammonia (NH_3). Further reaction of the now dehydrated substrate with HMDS produces trimethylsilyl substituted hydroxyl or oxide species and unstable trimethylsilylamine. The trimethylsilyl then reacts with another surface hydroxyl to produce ammonia or an inert trimethylsiloxy species. The steric constraints produced by the large bulky trimethylsily groups do not permit the penetration of water, rendering the surface of the substrate hydrophobic, as illustrated in figure 3.3.

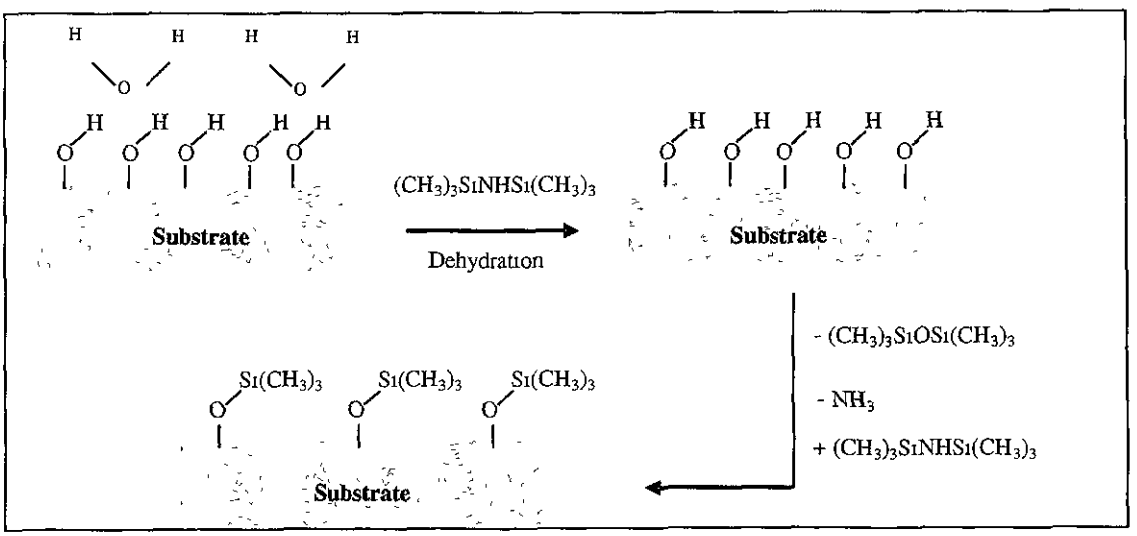

Figure 3.3: The reaction of HMDS with silicon to produce a hydrophobic surface.

Standard microscope glass slides (2.5 cm x 7.5 cm) which were rendered hydrophobic by HMDS were used as substrates in the Nima 2022 bath. The slide

was first cleaned in an ultrasonic bath for 10 to 15 minutes. It was then placed in a Petri dish and 2-3 drops of HMDS were spread on its surface and left soaking for 12 hours. Excess HMDS was removed by placing the slides in an ultrasonic bath in trichloroethylene, methanol, IPA, and ultrapure water for 10 to 15 minutes. The hydrophobic slides were dried in a stream of nitrogen.

3.1.5 Preparation of Hydrophilic Substrates

Silicon substrates with dimensions of 2 cm x 1 cm or 1 cm x 1 cm were used in the Nima 312D bath. The silicon was scribed with a diamond tip on its polished side and cleaved to the appropriate size. They were cleaned ultrasonically in ethyllactate, acetone, methanol and IPA respectively for 10 minutes, under cleanroom conditions. The substrates were then placed in an oxygen plasma etcher (Microwave Downstream Barrel Etcher IPLS205) for 10 minutes at 150°C. Finally, before use, a stream of nitrogen gas was passed over the surface.

3.1.6 Preparation of Monolayer Material

As an initial experiment ***Arachidic acid (AA)***, (Sigma Aldrich, > 99%), was used in the Nima 2022 bath. Katharine Blodgett was the first to report her work with AA in 1939 [3] and since then this molecule has been studied intensely as a prototypical molecule. An AA solution with a concentration 1mg per ml of chloroform was prepared in a volumetric flask with 10ml of chloroform. The flask is shaken vigorously in an ultrasonic bath to ensure the acid had dissolved. The structure of AA is shown in figure 3.4.

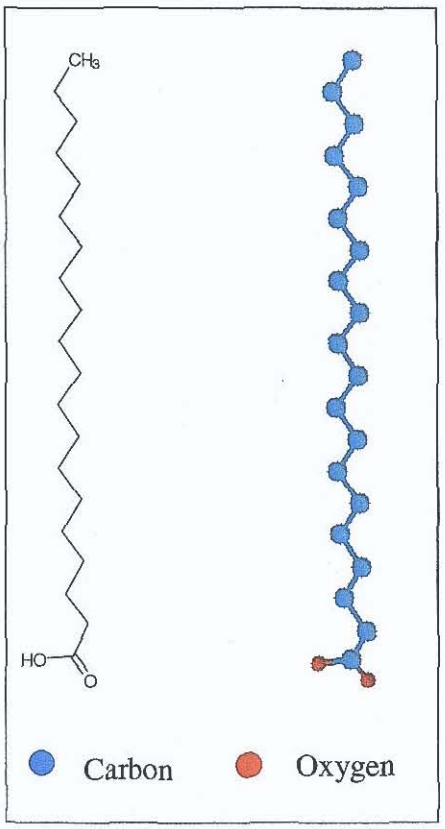

Figure 3.4: The 2D and 3D structures of AA, drawn using ChemSketch [4].

A 0.5 mg/ml solution of ***Copper(II) 2,9,16,23-tetra-tert-butyl-29H,31H-phthalocyanine (CuTTBPc),*** figure 3.5, purchased from Sigma Aldrich (> 97%), was prepared in a similar manner. Solutions containing different molar ratios of AA and CuTTBPc were made by mixing the appropriate volumes of 1mg/ml AA with 1mg/ml CuTTBPc. For example a 1:1 molar ratio of Pc:AA was prepared by mixing 2.56ml CuTTBPc with 1ml AA. Ultrapure water with a resistivity of 18.2 MΩ at room temperature, 25°C, was used for the subphase. The pH of the subphase was varied by adding concentrated HCl (Sigma-Aldrich, 37% fuming).

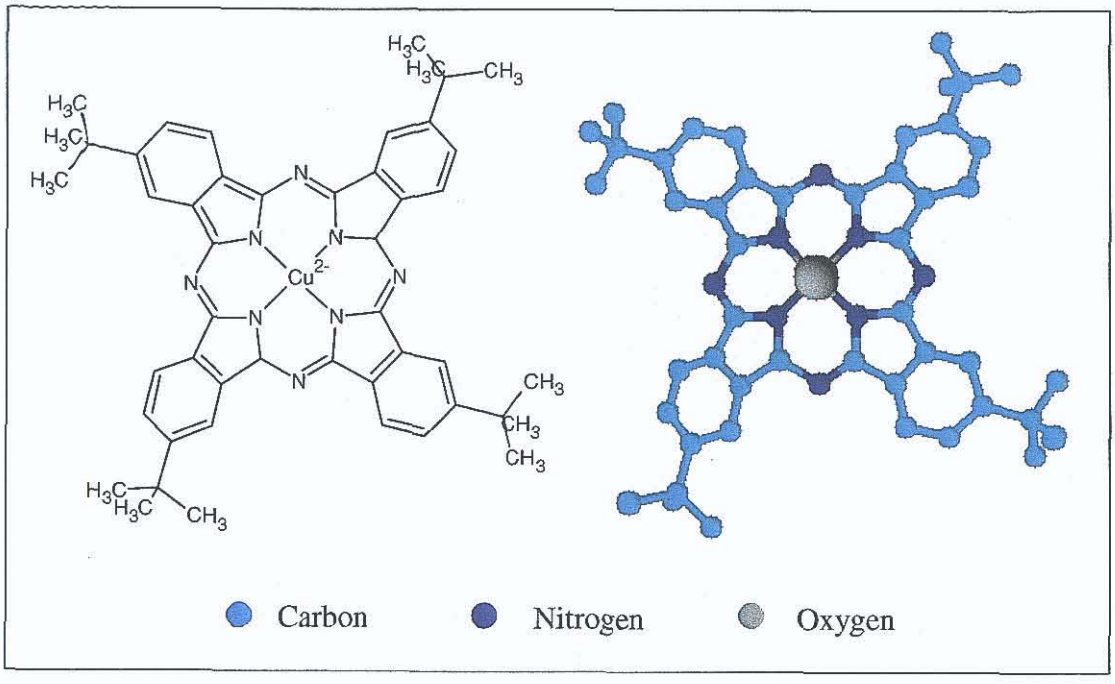

Figure 3.5: The 2D and 3D structures of CuTTBPc.

3.1.7 Obtaining Isotherms and Deposition onto a Substrate

A clean 50μL Hamilton-Bonaduz syringe was used to deposit solutions onto the subphase. The amount of solution used in the bath is critical so the syringe was held a few millimeters away from the surface to prevent drops accelerating and passing into the bulk of the subphase. The pressure reading must return to zero after evaporation of the chloroform as the molecules are then in their "gas phase" and therefore do not exert any pressure on the surface [5]. Once the reading had returned to zero the barriers were closed at a controlled speed and isotherms of the monolayer were recorded. Even though the subphase was ultra pure water it was possible that traces of ions or other contaminants were present. Any ions present in the subphase could react with the monolayer. The spreading and removal of monolayers removes most of these ions, so that the final spreading of the molecules should produce a "clean" monolayer.

In some cases lack of control over the evaporation of the film and the dissolving of the molecules in the subphase can lead to film loss [5]. If the experiment was carried out quickly after spreading the monolayer then film loss was

insignificant in the π- A isotherm. For this reason experiments should be carried out as soon as the monolayer has been deposited on the surface.

The target pressure, which was usually chosen to be in the liquid or solid phase, was determined from the isotherm. The monolayer should be stable at the target pressure to ensure that an ordered monolayer transfers to the substrate. With some molecules it is necessary to choose different pressures and to monitor the rate of change of area with respect to time. If the pressure was stable then no change in the area was observed typically over a 30 minute time period. A monolayer was then deposited by lowering and raising the substrate into the subphase at the chosen target pressure. Various parameter such as dipping speed and waiting times (i.e. the time interval between depositing successive layers) were determined experimentally. In some cases, as with CuTTBPc, it was beneficial to dry the first layer on a hotplate to improve the deposition of subsequent layers.

3.2 STM Experimental Setup

STM is a valuable technique which makes it possible to view and observe the behaviour of individual molecules on a given surface. Experimentally certain criteria must be met to make this possible. STM measurements must be carried out in a UHV environment and steps should be taken to minimise external noise. The tips used to probe the surface should be sharp and the feedback loop should be sufficient to produce clear images or spectra. The following sections detail the various aspects of the STM.

3.2.1 Scanning modes and tips

The scanning tunnelling microscope (STM) can operate in constant current or constant height mode. In constant height mode a constant voltage is applied to the z-piezo, the tip is scanned across the surface and changes in the tunnelling current between the tip-sample are monitored. The variations in the tunnelling current are of the order of 1nA, therefore necessitating the use of a sensitive amplifier.

In constant current mode the tunnelling current is maintained at a constant value by adjusting the tip height as it scans across the surface. Changes in the tip

height are monitored to provide a topographical image of the surface. The two different scanning modes are shown in figure 3.6.

The tips used in the STM were electrochemically etched polycrystalline Pt/Ir tips. Very little preparation is required when using these tips and they can be sharpened either by carrying out a control "tip crash" on the surface or by rastering the tip quickly across a surface. Both methods should ensure that any debris on the tip is removed.

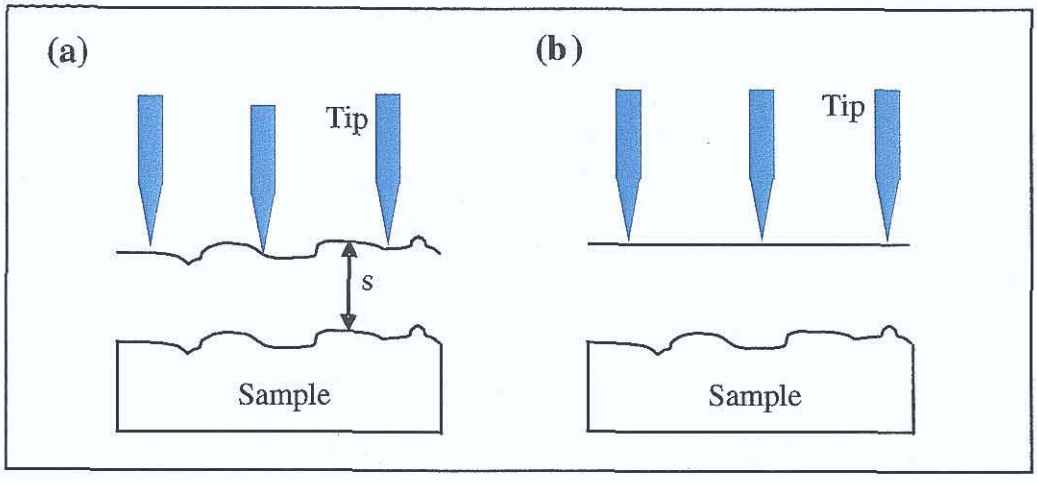

Figure 3.6: The different scanning modes in STM, where s is the tip-sample seperation. (a) Constant current mode and (b) constant height mode.

It is also possible to carry out spectroscopic measurements, or scanning tunnelling spectroscopy (STS). The tip is held at a fixed point on the surface, the voltage is varied while the tunnel current is measured generating a current-voltage *I(V)* spectrum. The features in the *I(V)* spectra can be related to the density of states, both filled and empty, of the surface. *I(V)* curve measurements are taken at a fixed tip-sample separation in order to correlate the surface topography with the local electronic structure.

3.2.2 STM Feedback Mechanism

The tunnel current is amplified and converted to a voltage. The distance dependence is then extracted by passing the signal through a logarithmic amplifier and the output signal is compared to a preset value, with corresponds to a specified gap width, s. The difference signal is fed to the z-piezo high voltage amplifier and

the tip is moved towards or away from the surface to bring the gap width back to the desired value. A topographical image can be attained from the changes in the z-piezo displacement during the scan assuming the barrier height remains constant over the scan area.

Constant current mode is limited by the stability of the feedback loop, figure 3.7. The tip begins to oscillate if the phase shift of the system exceeds 180°. When this happens the feedback loop is said to be positive. The cut off frequency of the feedback loop (or the maximum frequency at which the feedback loop can operate in negative feedback) is in the kHz range. The output of the I-V converter is fed into a low pass filter to suppress the high frequency signals. The scan speed is limited by time delays within the circuit, which can cause oscillations. Ideally the overall gain of the feedback loop should be as large as possible so that the tip accurately follows the contours of the surface. However, a compromise value is often chosen to ensure that the gain is less than unity, above the cut off frequency. The cut off frequency must be below the mechanical resonance frequencies of the STM head to prevent feedback instability due to transmitted vibrations.

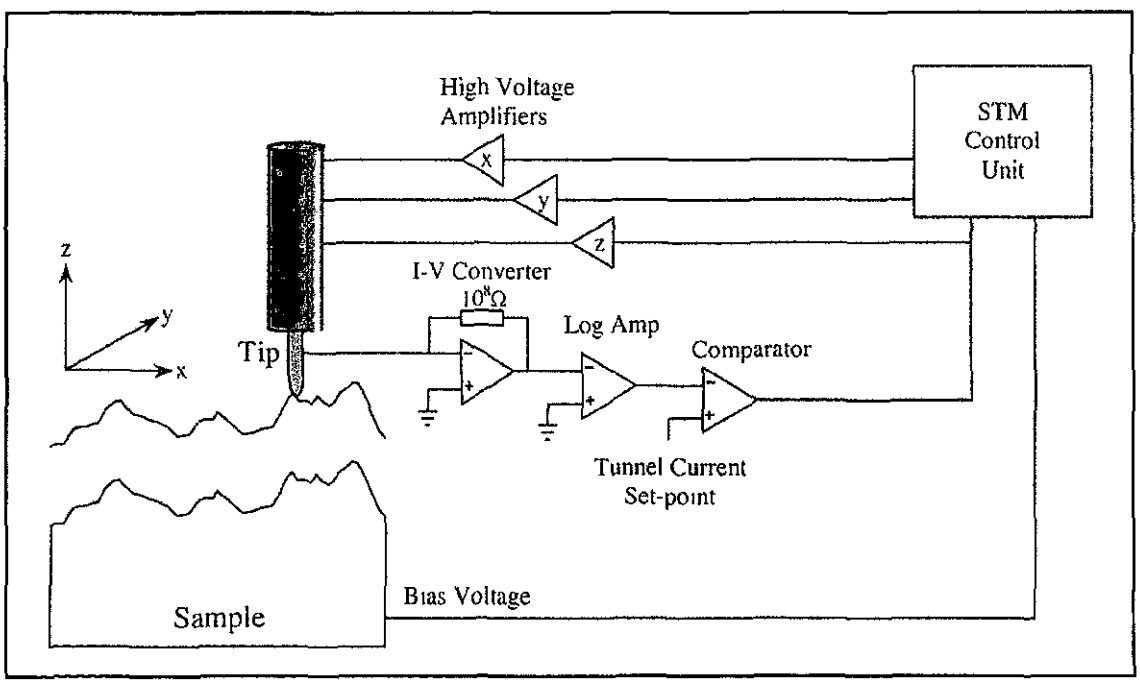

Figure 3.7: Feedback loop for the STM in constant current mode.

3.2.3 UHV System

The UHV system consists of three main chambers: the preparation chamber, the analysis chamber and the room temperature STM chamber. Samples and tips can be loaded through a fast-entry load lock attached to the preparation chamber. The layout of the system is shown in figure 3.8.

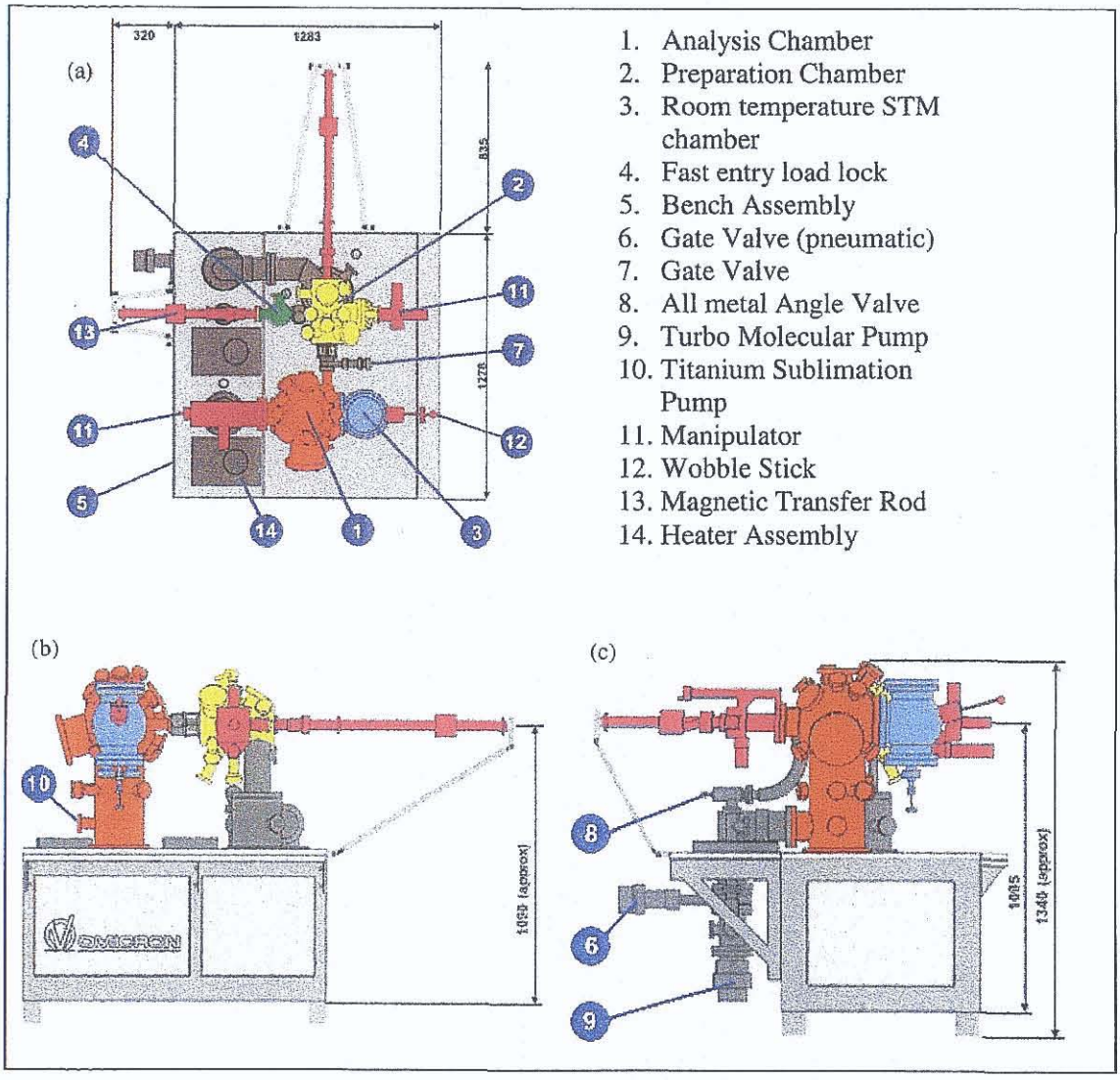

Figure 3.8: Diagram of UHV system showing the (a) top, (b) side and (c) side views [6].

3.2.4 STM Sample Holders

Sample holders for the STM were purchased from Omicron Vacuumphysik [6]. They are manufactured from tantalum and have a keyhole at the front so they can be captured and moved within the UHV system. The sample holder allowed for direct current heating of the sample.

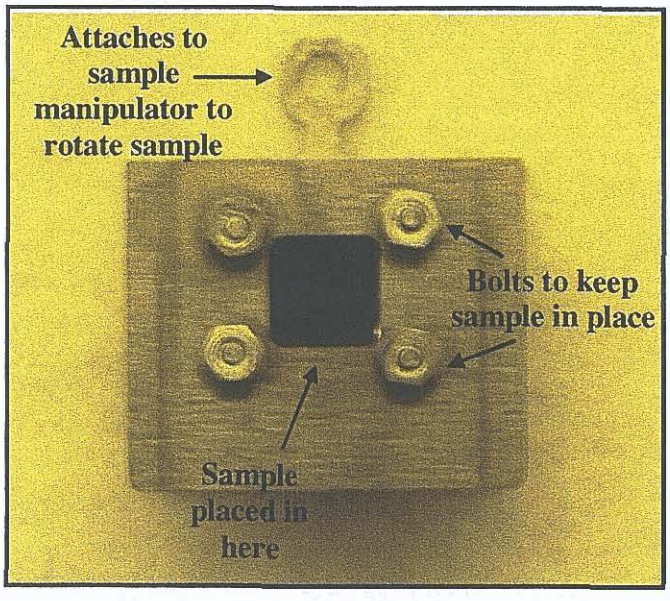

Figure 3.9: The STM sample holder

3.2.5 Vibration Isolation

Vibration isolation is crucial when imaging with the STM. To minimise external noise the STM head must have a high resonance frequency and be small, light and rigid in design. The STM should also be mounted on a spring vibration isolation system. An eddy-current damping system is also used in conjunction with the spring system. The spring system and the eddy-current damping system used in the Omicron VT-STM are shown in figure 3.10.

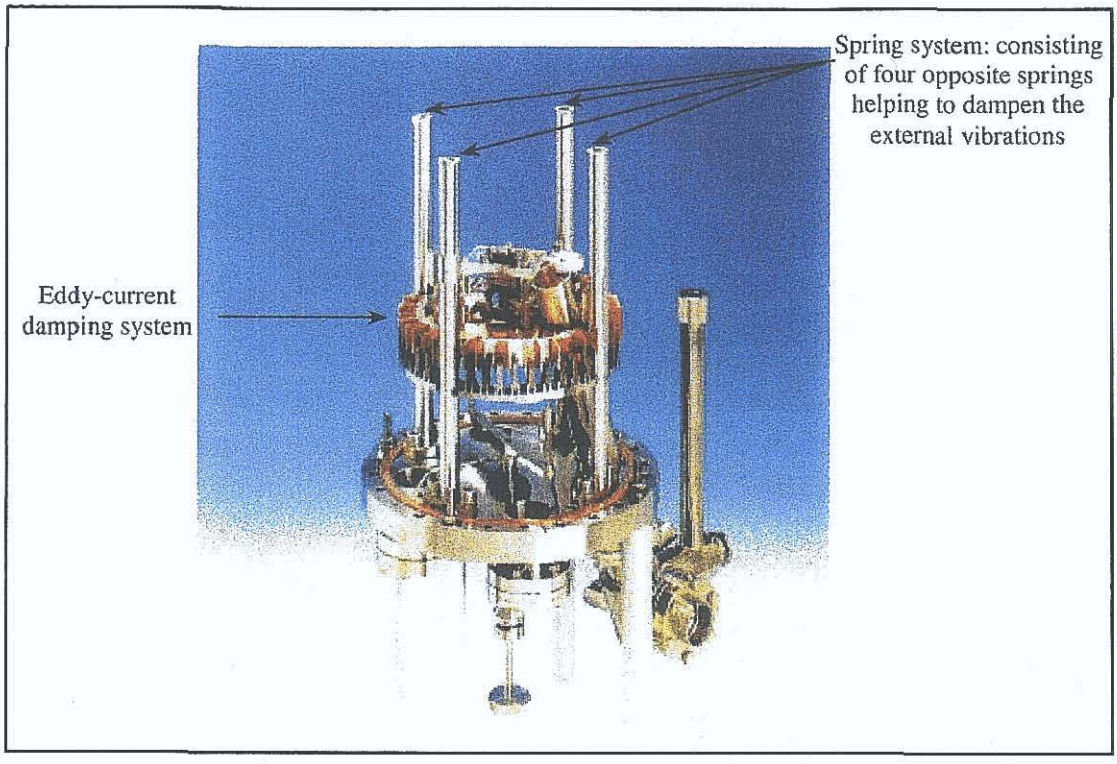

Figure 3.10: Picture of the STM showing the spring damping system and eddy current damping system [7].

3.2.6. STM Experimental Setup

The STM/STS experiments were performed at room temperature in an ultra-high-vacuum (UHV) system consisting of an analysis chamber (with a base pressure of 2×10^{-11} mbar) and a preparation chamber (5×10^{-11} mbar). STM images were recorded in constant current mode. The voltage V_{sample} corresponds to the sample bias with respect to the tip. The Si(111) substrate was p-type boron-doped with a resistivity in the range 0.1 – 1.0 Ωcm. Atomically clean Si(111)-(7 × 7) surfaces were prepared in the usual manner by *in situ* direct current heating to 1520 K after the samples were first degassed at 870 K for 12 hours. The clean Si(111)-(7 × 7) surface was checked by low-energy electron diffraction (LEED) and STM before preparation of the Ag/Si(111)-($\sqrt{3}$ × $\sqrt{3}$)R30° surface. Silver (Goodfellow Metals) was deposited by e-beam evaporation from a molybdenum crucible onto the Si substrate, which was maintained at 770 K during the deposition. The cleanliness of the Ag/Si(111)-($\sqrt{3}$ × $\sqrt{3}$)R30° surface was verified by STM and LEED before

phthalocyanine deposition. CuTTBPc (Aldrich Chemicals) was evaporated in the preparation chamber, isolated from the STM chamber, at a rate of about 0 2 ML (monolayer) per minute from a tantalum crucible in a homemade deposition cell operated at a temperature of approximately 600 K. The total pressure during phthalocyanine deposition was in the 10^{-9} mbar range. Before evaporation the phthalocyanine powder was degassed for about 12 h to remove water vapour.

Tunnelling spectra were acquired on a grid of specified points within an image. At each point where an *I(V)* spectrum was recorded, the scan was interrupted during imaging. The feedback loop was switched off and a voltage ramp was applied after a short delay time in order to allow stabilisation of the current preamplifier. In between these points the feedback was on and the STM operated in constant current mode. While recording *I(V)* spectra it was ensured that current measurements did not exceed the dynamic range of the current preamplifier. Before and after *I(V)* spectra acquisition the quality of the surface was verified by STM imaging in order to check that no damage was done to the measured layer during acquisition of the *I(V)* spectra. Data was averaged over 2, 500 spectra per image.

3.3 Atomic Force Microscopy

3.3.1 The Atomic Force Microscope

A Digital Instruments Dimension 3100 AFM was used for imaging substrates produced by the LB technique. Information regarding surface coverage, surface roughness and monolayer height can be established through analysis of AFM images. A tapping mode tip is mounted on a tip holder and the holder is placed on the end of a scanner tube constructed from piezoelectric material which expands and contracts in proportion to an applied voltage. Within the tube there are three electrodes for motion along the X, Y, and Z axes. In the Dimension 3100 AFM the sample remains stationary while the tube scanner rasters the tip across the sample surface The Dimension 3100 AFM has a maximum travel of 6μm in the Z direction and 90μm in the X and Y direction. Light, with a wavelength of 670nm, is emitted from a semiconductor diode laser down the center of the scanner tube [8]. The light

is aligned to the back surface of the cantilever and the reflected beam is focused onto a quadrant photodiode detector. Vibration isolation is vital when imaging so the AFM is mounted on a vibration isolation table which suspends the AFM stage by using nitrogen gas at a pressure of 4 bar in four pistons. The AFM is pictured in figure 3.11.

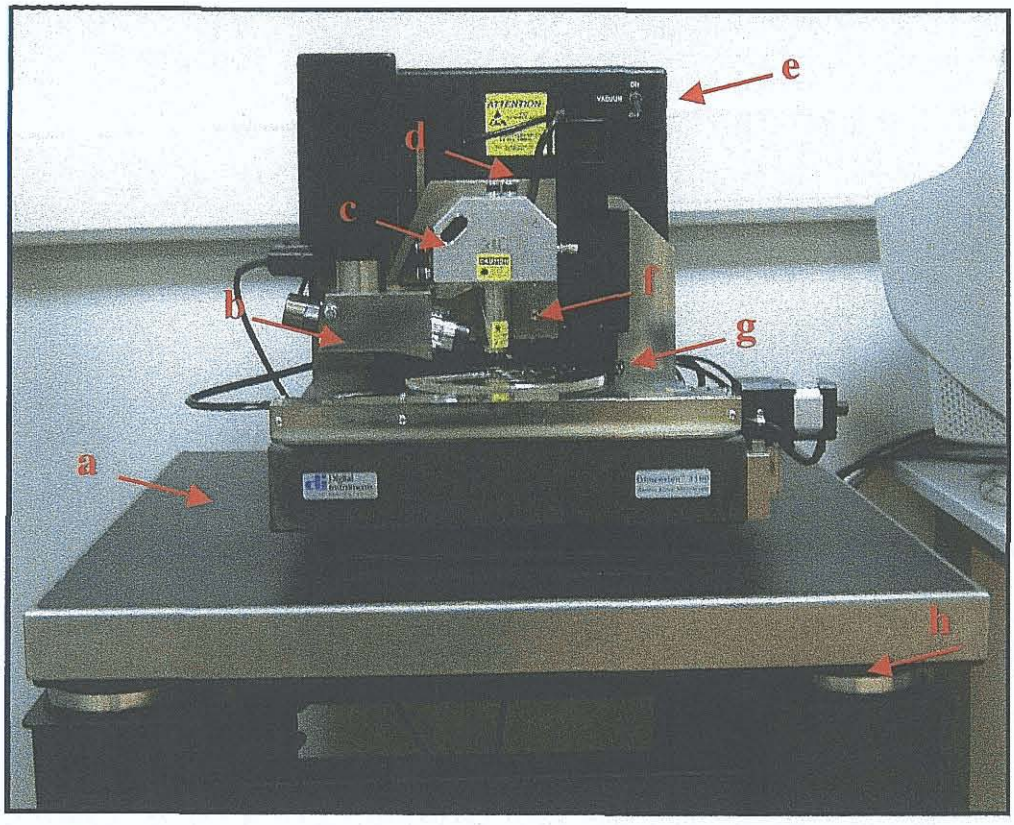

Figure 3.11: Setup of the AFM where (a) is the integrated vibration isolation table, (b) the camera adjusters, (c) the photodetectors adjusters, (d) the laser light adjusters, (e) the vacuum switch, (f) the scanner tube, (g) the tip holder and (h) pistons.

3.3.2 AFM Feedback System

Due to the displacement of the cantilever during scanning one half of the photo diode (either A or B) may receive more light than the other. The difference between the photodiode signals divided by their sum produces an output signal proportional to the cantilever deflection. The feedback loop for the tapping AFM acts to maintain a constant amplitude during operation and the Z position of the scanner is adjusted accordingly. The feedback loop for the AFM in tapping mode is shown in figure 3.12.

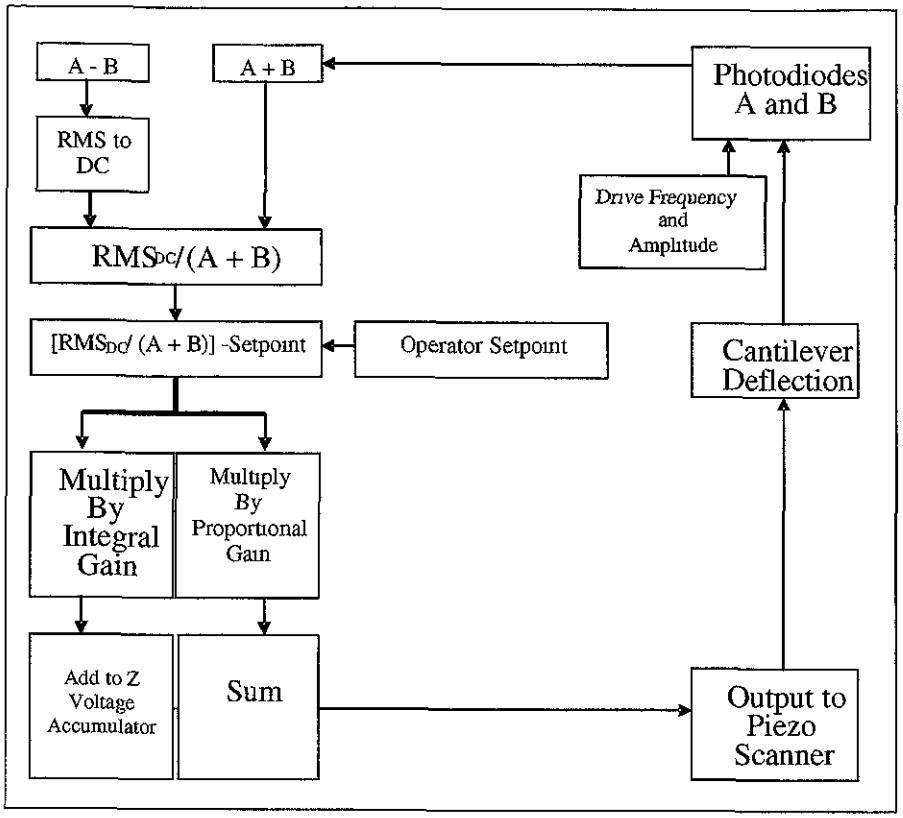

Figure 3.12: The feedback loop for the AFM in tapping mode.

3.3.3 AFM Probes

The silicon nitride tapping mode cantilevers, figure 3.13, were purchased from Olympus Optical Co , Ltd. They had resonant frequency of approximately 300 kHz and a spring constant in the range of 38-49 N/m.

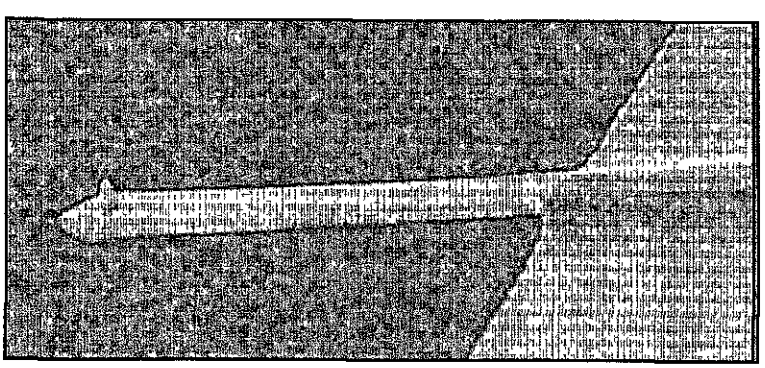

Figure 3.13: Silicon nitride tapping tip used in the AFM. The tip can be seen here at the end of the cantilever [9].

In tapping mode the cantilever is tuned to its resonance frequency before it approaches the surface. A voltage is applied to the piezoelectric, which oscillates the cantilever, and the tip is scanned through the resonance frequency while the amplitude is monitored. For a functioning tapping mode tip the response curve has a Lorentzian shape. The phase difference between the piezoelectric crystal and the laser light reflected from the tip (amplitude) is also monitored. It is found that the maximum amplitude occurs when there is a phase difference of 90° between these two signals. Figure 3.14 shows a plot of the amplitude and phase difference as a function of the drive frequency. At the resonance frequency the slope of the response curve is close to zero and this gives a low sensitivity. For this reason experiments are carried out with the drive frequency offset to sensitivity For the tapping tips used to image the LB films the resonance peak was found to lie in region of 282-305 kHz.

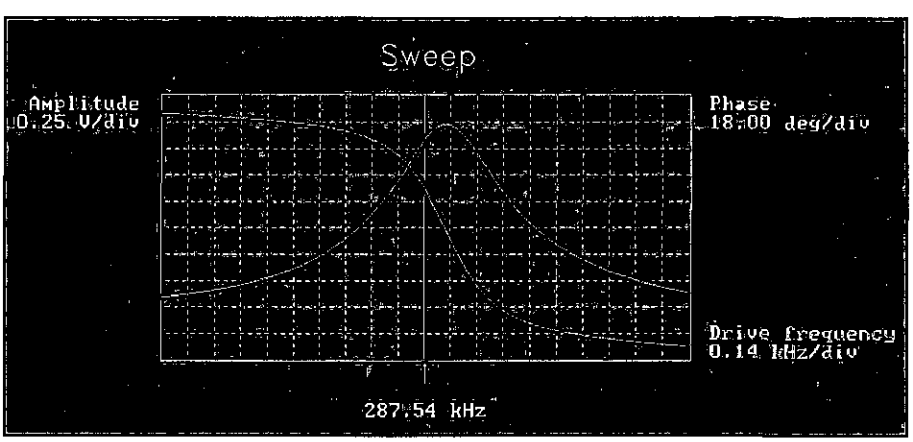

Figure 3.14: An example of a cantilever tune in tapping mode.

3.3.4 Scanning in Tapping Mode

Samples were mounted on the stage and held in place using a vacuum chuck. An optical microscope was used to focus on the surface and the tip was brought to within a 1mm of surface. It was possible to select a region of interest on the surface by moving the sample with a motorised stage. Once an area of interest was found the tip was brought into contact with the surface. The cantilever was stepped slowly towards the surface while oscillating. Changes in the oscillation amplitude of the cantilever indicated an interaction with surface.

During scanning the tip lightly taps the surface and a constant oscillation amplitude is maintain by the feedback loop. The scanner moves the tip in the vertical direction to ensure the amplitude is maintained and in doing so a topographical image of the surface is formed. By altering the amplitude setpoint it is possible to change the force exerted by the tip A minimum force was required for imaging the LB films. As the tip scans across the surface the height of surface may change significantly. The feedback loop maintains a constant deflection signal by adjusting the height of the piezo tube. When the tip encounters high surface features the tip is lifted. The tip overshoots and the response to this overshoot is related to the proportional gain. Ideally the proportional gain should be set high but not so high that it will feed noise into the signal. If the gains are set too high it can cause the piezoelectric scanner to oscillate. The integral gain controls the response of the cantilever as it travels over topographical features. As with the proportional gain the integral gain should also be set high. Typical values for the integral and proportional gains were 0.5 and 0.7 respectively for tapping mode operation.

Images were typically taken with a scan rate of 1 Hz and a scan size of 5μm. Maximum resolution was achieved by setting the number of lines per image to 512 and the number of samples per line to 512.

3.4 Spectroscopic Ellipsometery

3.4.1 Description of the Ellipsometer and Experimental Setup

A Jobin-Yvon Horiba, UVISEL ellipsometer consisting of a Xenon light source, polariser, sample stage, piezo-electric modulator (PEM), analyser, monochromator, photomultiplier tube (PMT) and data acquisition unit was used for this research. The Xenon light source provides a broad spectral range form FUV (190 nm) to NIR (1.7 μm). a photograph of the Jobin-Yvon Horiba, UVISEL spectrometer is shown in figure 3 15 and a schematic of the apparatus is shown in figure 3.16

The angle of incident of the incoming beam can be varied between 55-75°.Measurements were taken at an angle of 70°, however some variable angle spectroscopic ellipsometry scans (VASE scans) were also taken in the range of 55-

75° with a step size of 5° to check the goodness of fit for the mathematical model. Delta-Psi software Version 2 was used for all data analysis. The calibration of the ellipsometer is fully automatic and controlled by the computer software.

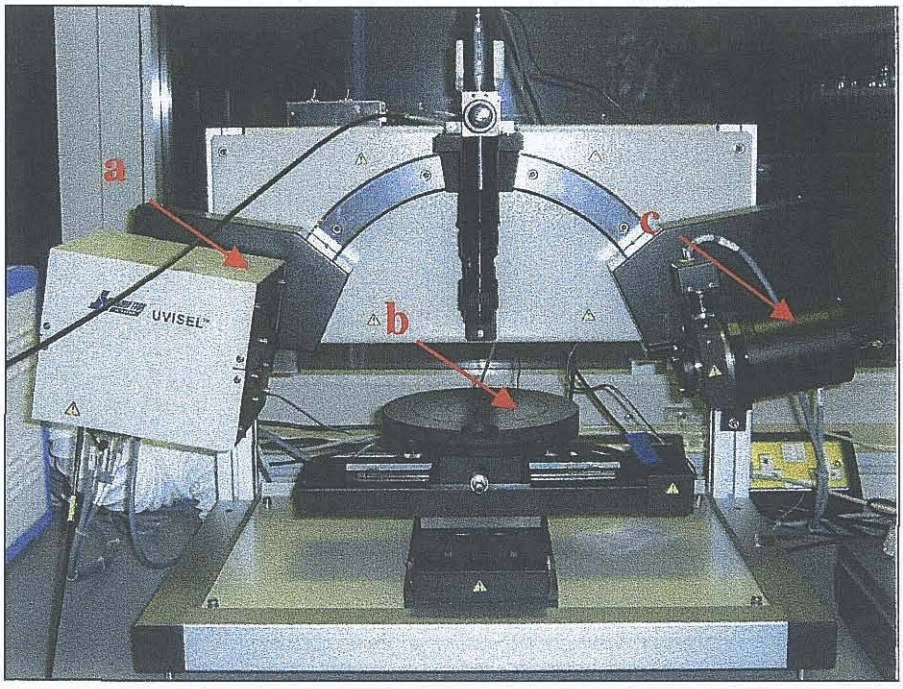

Figure 3.15: The setup of the ellipsometer where (a) is the PEM and analyser (which is linked to a monochromator), (b) is the sample stage and (c) is the polariser attached to an Xe lamp.

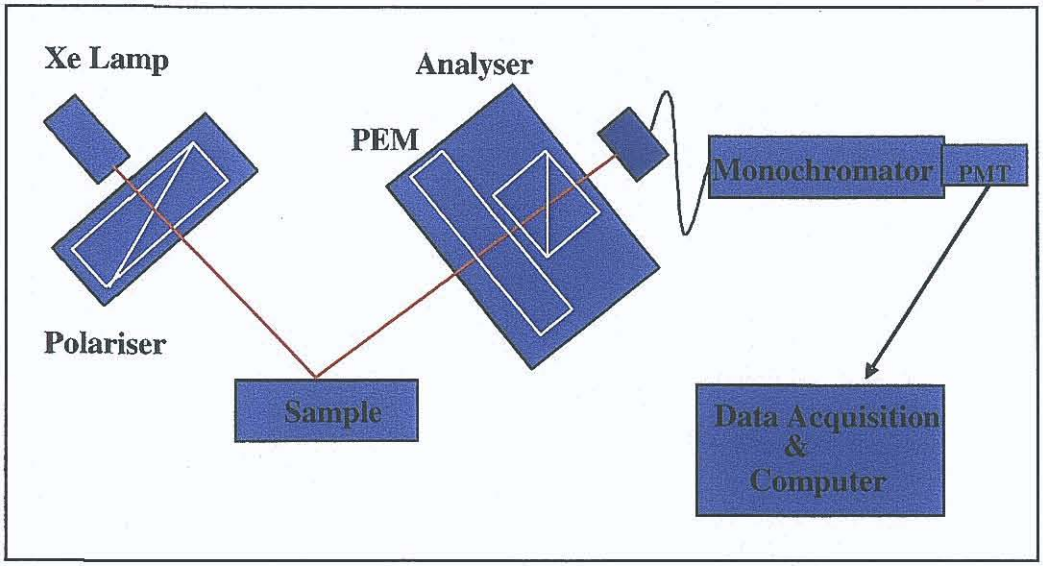

Figure 3.16: A schematic of the spectroscopic ellipsometer.

The incident beam was aligned on the sample and had a width of 1.5mm. The sample stage was levelled to ensure that a maximum signal was received by the detector. Experiments were carried out in the wavelength range of 300 - 1,000 nm. The number of accumulations was 1 and the integration time was 500 ms.

3.5 XPS Experimental Setup

3.5.1 Synchrotron Radiation

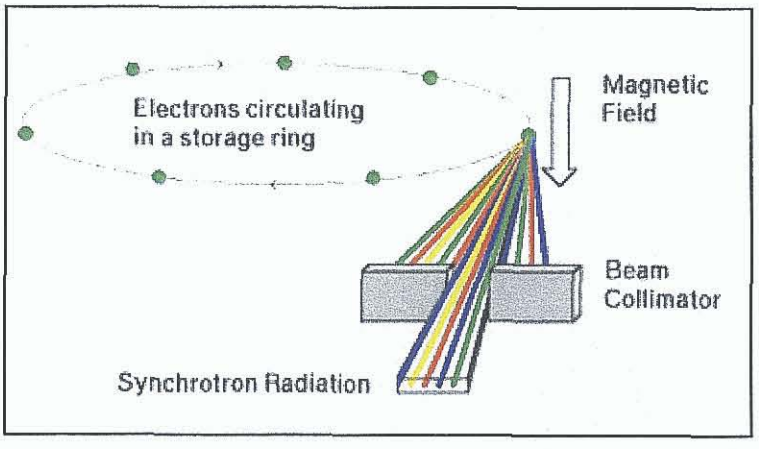

Figure3.17 The emission of synchrotron radiation.

Synchrotron radiation is emitted when charged particles moving at relativistic speeds are forced to follow curved trajectories, figure 3.17. The first visual observation of Synchrotron Radiation was in 1948 from the General Electric synchrotron in the USA during investigations into the design and construction of accelerators suitable for the production of very high-energy electrons. Over the next 50 years an explosive growth in the building of accelerators optimised for synchrotron radiation production has turned this interesting radiative energy loss into a valuable research tool [7].

The radiation emitted is extremely intense and extends over a broad wavelength range from the infrared through the visible and ultraviolet, and into the soft and hard X-ray regions of the electromagnetic spectrum. This is the energy range of radiation used in photoemission. Synchrotron radiation sources produce x-ray radiation which is of the order of 10^6 times more intense than that of

conventional light sources and are in addition continuously tuneable. A schematic diagram of the synchrotron ring at the Daresbury Laboratory is show in figure 3.18.

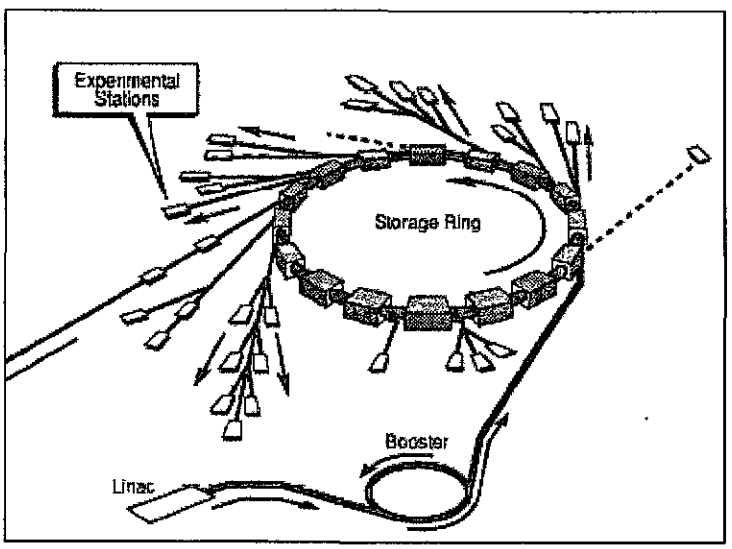

Figure 3.18: Synchrotron ring at Daresbury Laboratories [10].

Although the storage ring itself is under ultra high vacuum, electrons are removed by collisions with gas molecules so the beam current decays over time. The required radiation frequency is selected using a monochromator. The broad range of available frequencies means that synchrotron radiation is suitable for a wide range of experiments.

Not only does synchrotron radiation have high intensity but it is almost linear polarised in the plane of the storage ring as opposed to the unpolarised light from UV and X-Ray sources. Electrons in the synchrotron ring are "bunched" so the radiation will come as short pulses a few nano seconds long, which is useful for timing experiments.

3.5.2 Monochromator and Grating

Photoemission spectroscopy experiments require well-defined photon energies. The "white" synchrotron radiation must be monochromatised before entering the experimental chamber.

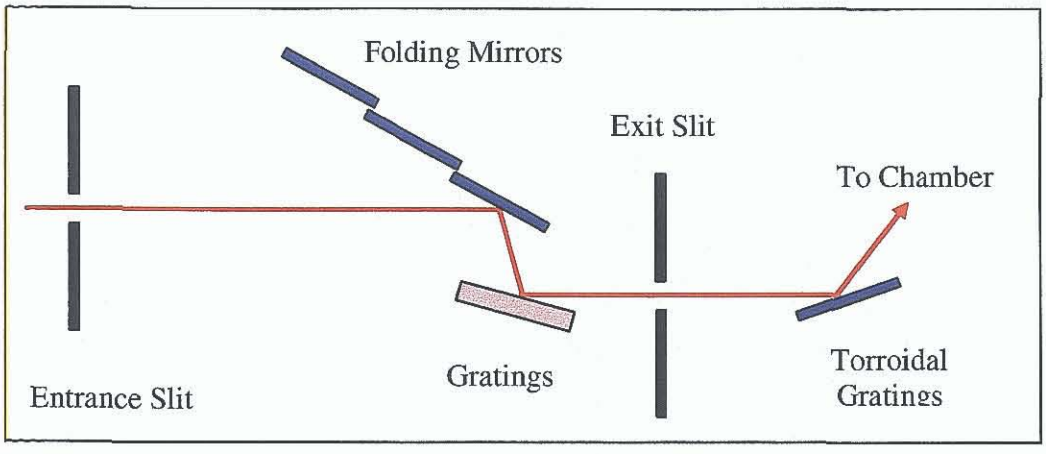

Figure 3.19: Layout of the monochromator

A reflection diffraction grating consists of a reflecting surface with a periodic array of lines separated by a distance d. If polychromatic light is incident on the grating at an angle of incidence, α and the exit slit is located at an angle β to the grating, the grating equation

$$n\lambda = d(\cos\alpha - \cos\beta) \qquad (3.1)$$

determines the wavelength passing through the slit. The first order light (n=1) is more intense than the higher order components and is therefore mostly used in experiments. The DL4.1 beamline has a spherical grating monochromator containing three gratings. The monochromator has a usable photon energy range from 30 eV to 400eV. Typical flux values are more than 10^{10} photons per second at 130 eV with 50 μm slits and are greater than 10^{9} photons per second at 350 eV with 100 μm slits.

3.5.3 The Electron Energy Analyser

The energies of the ejected photoelectrons are analysed using a SCIENTA SES200 electron energy analyser which permits fast acquisition of spectra with high-energy resolution, typically 100 meV for spectra taken at the excitation photon energy of 60 eV. A schematic of the system is shown in figure 3.20. An electrostatic field is applied between the inner and outer hemispheres. Electrons with an energy equal to the pass energy that are injected through the entrance slit are transferred from the entrance slit to the detector. The potential difference between the hemispheres determine the pass energy. A lens is used to transfer the electrons from

the sample to the entrance slit and the energy resolution is determined by the radius and width of the slits at the analyser entrance [11].

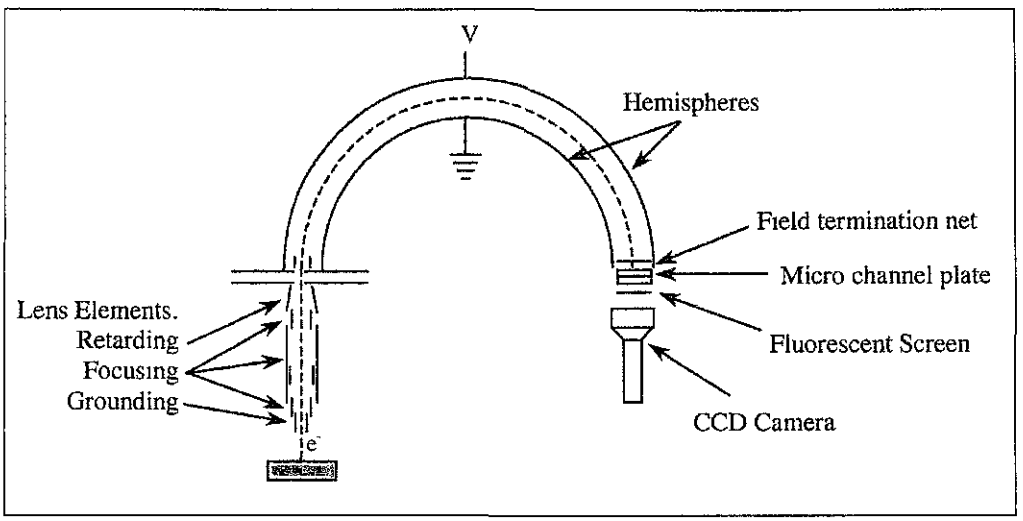

Figure 3.20: Diagram of SCIENTA spectrometer.

3.6 Near Edge X-ray Absorption Fine Structure

3.6.1 NEXAFS Experimental Setup

The NEXAFS experiments described in this thesis were carried out on the SX700 beamline at ASTRID storage ring in Aarhus, Denmark. The experimental station is used primarily for surface science experiments due to the 20-700 eV energy range. The estimated photon-energy resolution at the N 1s (~400 eV) and C 1s (~290 eV) absorption thresholds was better than 200 meV and 150 meV, respectively. A SCIENTA energy analyser was used. The layout of the SX700 beamline is shown in figure 3.21. The spectra were normalised to the incident photon flux monitored by a gold grid.

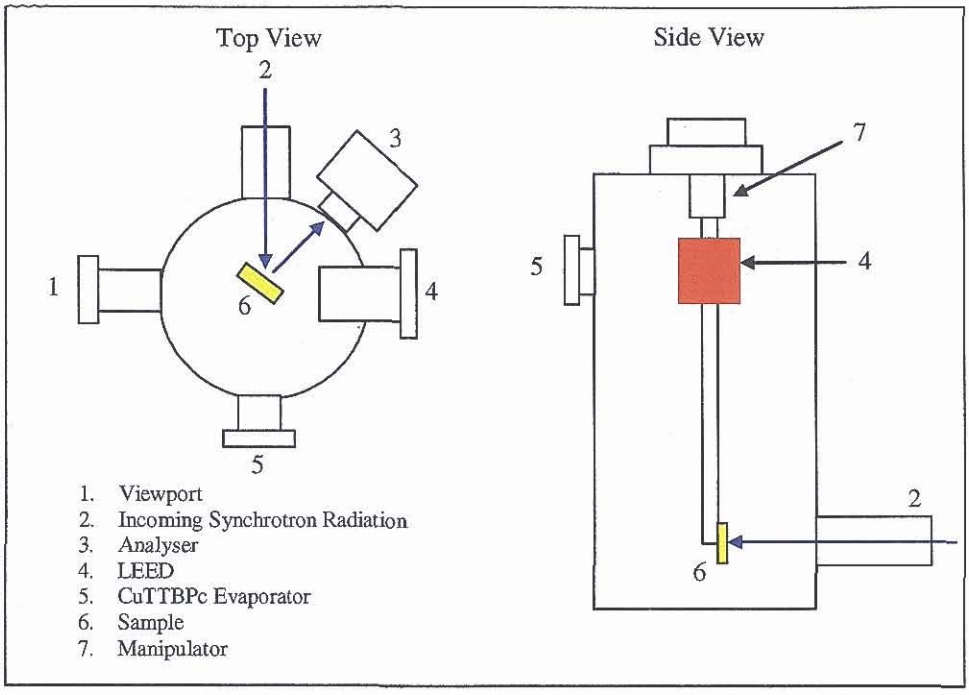

Figure 3.21: Layout of SX700 beamline.

Chapter Three References

[1] Nima Technology, **Tensiometers and Langmuir-Blodgett Troughs**, Operating Manual, 4th Edition, 1995.

[2] www.siliconresources.com

[3] K.B Blodgett, Physical Review, **55**, (1939) 391.

[4] ACD/ChemSktech Freeware, Product Version 10, www.acdlabs.com

[5] **An introduction to Ultrathin Organic Films from Langmuir-Blodgett to Self-Assembly,** Abraham Ulman, Academic Press, 1991.

[6] Omicron Vaccumphysik, www.omicron.de

[7] Darren Carty , **RAS and STM Investigations of Pentacene Molecules on Metal and Semiconductor Surfaces**, PhD Thesis, 2004

[8] **Scanning Probe Microscopy Training Notebook**, Digital Instruments, 1998.

[9] www.socgenmicrobiol.org.

[10] www.srs.ac.uk

[11] www.iap.tuwien.ac

Chapter 4

A Study of Thin Films, containing AA and CuTTBPc, produced via the LB Technique

Chapter 4 reports the findings of LB films produced using pure AA, pure CuTTBPc and mixed films of AA and CuTTBPc. AA films were grown to gain familiarity with the LB technique and experience in the interpretation and analysis of isotherms. A range of films were produced and, as predicted, were Y-type in configuration. A study was undertaken to investigate if changes in dip speed, pH or drying times between layers would affect the film quality. CuTTBPc exhibited strong aggregation which made the synthesis of smooth monolayers a cumbersome task. AA was incorporated into the CuTTBPc monolayer in differing molar ratios to try and reduce aggregation and improve film quality. A range of films were grown using a 1:1 molar ratio of CuTTBPc:AA. The transfer ratios would suggest that the films were Y-type in structure indicating that deposition was occurring on both the up- and downstroke. Further studies on the film quality, using molar ratios of 1:2 – 1·10 CuTTBPc:AA and 2:1 – 8:1 CuTTBPc:AA, were also undertaken. A series of 11 layer films were produced and in general it was found that the aggregation reduced as the amount of AA was increased.

4 Langmuir-Blodgett Films

4.1 Arachidic Acid LB Films

A vast amount of work spanning from 1939 [1] the present day [2]-[14] has been carried out on the ***Arachidic Acid (AA)*** molecule in the field of LB research. AA has a simple structure with very distinctive hydrophobic and hydrophilic properties. Such characteristics make this molecule suitable for first time users of the LB trough. A monolayer of AA will clearly exhibit the phase changes the monolayer will undergo upon compression. Through working with such a simple molecule valuable experience is gained in the manipulation of monolayers and the interpretation of isotherms. Experience is also gained in observing the behaviour of

the meniscus during film deposition, the effect of tweaking dipping parameters (such as dip speed, drying times etc.) and reading transfer ratios. These basics skills can then be applied when working with more complicated molecules. Sections 4.1.1 and 4.1.2 report the findings of work carried out in this research using AA.

4.1.1 Arachidic Acid Isotherms

Arachidic Acid (AA) was used on the Nima 2022 Model. A 1mg/ml solution of AA in chloroform was prepared and 50 µL of the solution was spread dropwise on the subphase using a Hamilton syringe. After each drop was spread the pressure reading increased from 0 mN/m to 0.2-0.4 mN/m and thereafter returned to zero as the chloroform evaporated. Any traces of excess chloroform evaporated upon leaving the monolayer to rest for five minutes before beginning compression of the film. This time delay also gave the molecules a chance to order on the surface. Compression of the AA monolayer was carried out at a speed of 10 cm^2/min and the isotherm obtained showed three very distinct regions where the molecules were in the gas, liquid and solid phases respectively. On the initial compression of the monolayer the molecules began a phase transition from the gas phase to the liquid phase at approximately 27.5 $Å^2$/molecule. Continued compression of the monolayer resulted in a steady increase in pressure indicating that the molecules are moving closer together. Figure 4.1 shows a single isocycle of the monolayer.

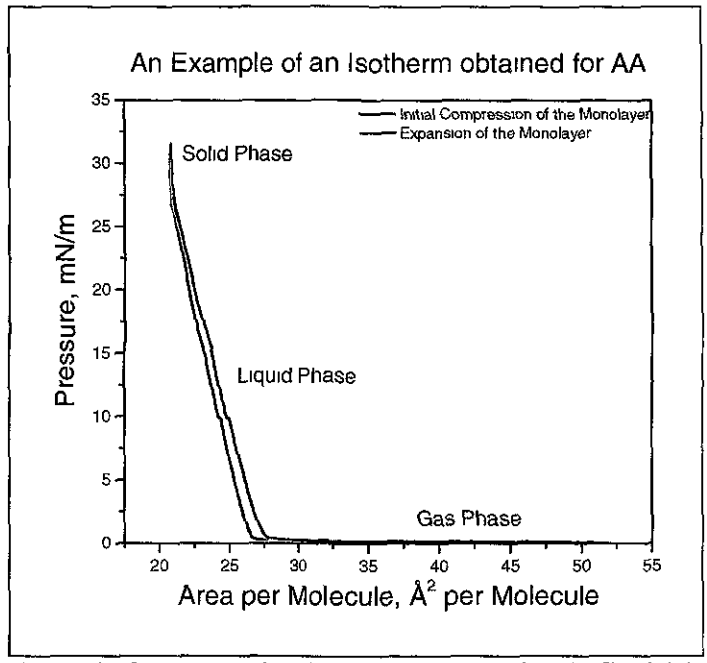

Figure 4.1: Showing a single compression (black) and expansion (red) of AA on an ultrapure water subphase. The gas, liquid and solid phase can clearly be identified. A slight kink in the isotherm at approximately 10mN/m may be a result of the molecules rearranging on the surface. However, the molecules still remain the liquid phase at this pressure.

The molecules were still considered to be in the liquid phase up to a pressure of approximately 27.5 mN/m After this point there was almost a vertical increase in pressure and the molecules entered the solid phase. Isotherms similar in shape and showing the different phases have been obtained by other groups [6,7,9,10,13-14].When comparing these isotherms one will see that the areas at which phase transitions occur and the ***limiting area per molecule (LAM)*** differ slightly in various publications [6,7,9,10,13-14]. LB films are sensitive to humidity, temperature change and pH. The nature of the subphase will also determine the shape and the position of phase changes in an isotherm. These factors were taken into consideration when obtaining and interpreting the data. The LAM was calculated by extrapolating a straight line to the x-axis. Figure 4.2 shows the determination of the LAM for AA at a pressure of 20 mN/m on ultrapure water. Note the LAM can also be calculated by extrapolation from the target pressure to the x-axis.

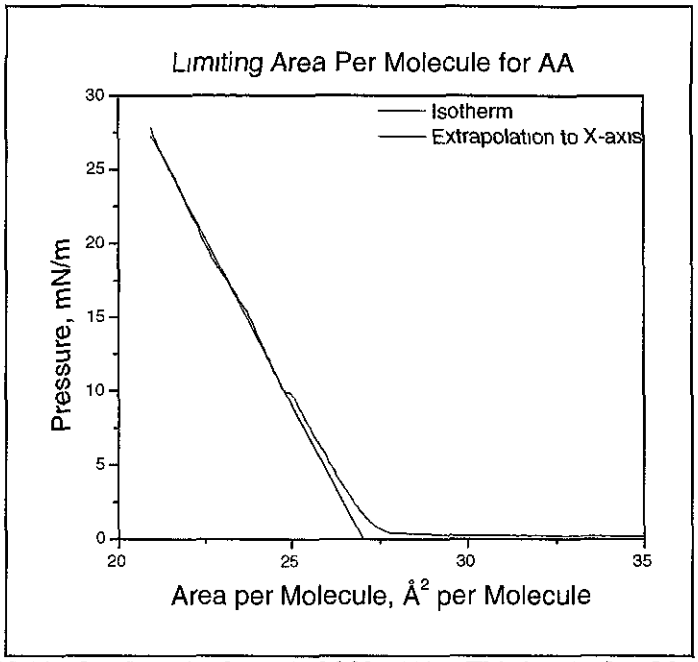

Figure 4.2: The LAM in the above isotherm is 26.93 mN/m. This is calculated by extrapolation to the x-axis.

Isocycles were used to check the reproducibility of isotherms. The monolayer was continuously compressed and expanded at a constant speed to a controlled pressure. Due to the constant compressions and expansions the molecules packed closer together and eventually the isotherm for one isocycle was be almost identical to that of the next. Molecules which do not aggregate should produce identical isotherms.When carrying out isocycles with AA the maximum pressure to which the monolayer was compressed was 45 mN/m. This is to ensure that the monolayer does not collapse. The collapse pressure for AA was found to lie between 60-65 mN/m. A similar collapse pressure was found by T. Kajiyama *et. al.* [6].

4.1.2 A Study of the effect of Subphase, pH, Dipping Speed and Drying Times

A study of how the subphase pH, the dipping speed and the drying time between layers was undertaken by Diaz *et. al* [12]. Measurements were made as to how changes in these parameters influenceed the transfer ratios of the LB films.

Three different types of films can be produced using the LB technique; they are namely X-, Z- and Y-type. X-type films are produced when deposition occurs predominately occurs on the downstroke. Z-type films are a result of deposition

occurring predominately on the upstroke and Y-type are a result of deposition occurring on both the downstroke and upstroke. High pH values and the film loosing its ability to deposit on the upstroke, for example due to slow dipping speeds, result in the formation of X-type films. Occasionally molecular rearrangement may take place if the film is held under water. The outer layer of the film will become hydrophobic meaning deposition will occur on the downstroke. This is another reason for the formation of X-type films. S. Evenson et. al. [8] observed this phenomenon when synthesising AA films a $CdCl_2$ subphase. Z-type films occur when water is entrained on the outer layer of the film as it is raised out of the subphase. By not giving the outer layer of the film sufficient time to dry deposition will not occur successfully on the downstroke. The layers will therefore deposit on the upstroke giving the film an over all Z-type structure [12]. In a separate study by Diaz *et. al.* and Cerro *et. al.* [15] water entrainment was found to exist in films of AA films produced on a $ZnSO_4$ subphase. This entrainment was shown to have an effected on the contact angle and transfer ratios.

Using a $CdCl_2$ subphase, Diaz and Johnson [21] observed how dipping speeds, pH changes and drying times can influence the type of film produced. They found that by dropping the pH from 6.8 to 5.5 to 4.5 the film changed from X-, to Z- to Y-type, respectively. At a pH of 5.5 it was found that variations in dipping speed can influence the type of film produced. Y-type films were produced at speeds of 3, 19 and 33 mm/min but when the speed was increased to 65 mm/min a Z-type film was produced as a result of the water entrainment between layers. By allowing the layers to dry between depositions the film reverted back to Y-type.

In this work an experiment, similar to that of Diaz *et. al* [12] was performed. 50μL of a 1mg/ml solution of AA in chloroform was spread on an ultrapure water subphase, with a pH of 6.2. The layer was compressed at a speed of 10 cm^2/min to a target pressure of 23.5 mN/m. Films were then deposited onto a HMDS hydrophobic glass slide using a dipper speed of 20 mm/min. A range of films of various thicknesses were produced for which the drying time where the film was held above the surface after each dip was varied. The delay time below the surface was also varied to monitor how these time delays affected the transfer ratio. In total eight

films with a thickness of 2, 4, 6, 12, 14, 16, 24 and 34 layers were synthesised. The 2,4,6,24 and 36 layer films were held for 1 minute above the subphase with no delay below the subphase,while the 12, 14 and 16 layer samples where held for 2 minutes above the subphase and 1 minute below.

Ideally the transfer ratio for each layer should be 100%. In reality this is rarely the case. Many factors can contribute to the transfer ratio being above or below 100%. The meniscus travels in the direction of the dipper, that is to say that if the dipper is traveling downwards then the meniscus will curve downwards and if the dipper is traveling upwards the meniscus will point upwards. The change in the meniscus direction is responsible for the transfer ratio differing on the downstroke compared to the upstroke. For this reason all the downstroke transfer ratios should be similar to each other and all upstrokes should, likewise, be similar. A good example of this can be seen in figure 4.3 for the 24 layer AA film, where the filled squares denote the transfer ratios on the downstroke and the open squares denote the transfer ratios on the upstroke. The average transfer ratio was 99.15% on the downward stroke and 118.10% on the upward stroke, indicating that the film was Y-type. In this example the average for the downward stroke was close to the ideal value, however the average value for the upward stroke was higher than expected. A transfer ratio over 100% indicates a layer collapsing on itself as it deposits. This can be a result of the target pressure being too high [16]. It was not possible to program the bath to have a different target pressure on the downward and upward strokes Although the transfer ratio on the upwards stroke averages to 118 10% this was not a serious problem as the layers were depositing successfully. The average transfer ratio for the 2, 4, 6, 24 and 34 layer samples were 110.00%, 100.00%, 105.34%, 108.63 and 108.12%, respectively.

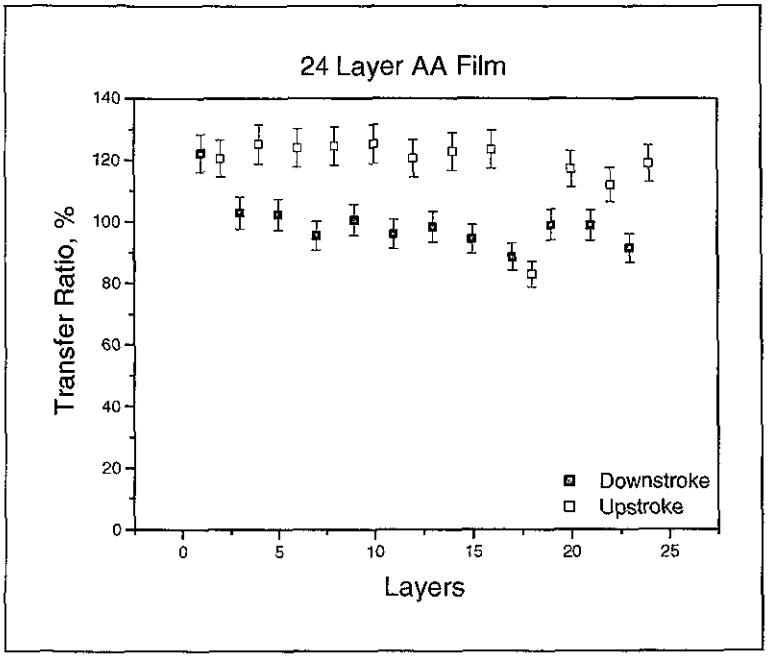

Figure 4.3: An example of the transfer ratios obtained for the 24 layer sample. Note how the difference in the transfer ratios for the upstroke compared to the downstroke.

The waiting times were then changed for 1 minute above and zero minutes below to 2 minutes above and 1 minute below to see if this would impact on the transfer ratios. Three films, with thicknesses of 12, 14 and 16 layers, were grown under these conditions. The 12, 14, and 16 layer samples gave average transfer ratios of 104.78%, 102.60% and 94.35%. These values were close to those obtained in the previous experiment. This indicates that changes in the waiting times had no significant affect on the transfer ratios obtained for these Y-type films.

The pH of the subphase was then systematically altered by the addition of concentrate HCl, to investigate its influence on the transfer ratio. The dip speed was 20 mm/min, the monolayer compression speed was 10 cm^2/min and the waiting time between layers was 1 minute above the subphase and zero minutes below. pH values of 2.9, 3.5, 3.7, 4.2 and 5.1 were used. A plot of the transfer ratios, for a series of films of different thickness, as a function of pH is shown in Figure 4.4. All films are Y-type. For each film produced, one layer partially peeled off causing a drop in the transfer ratio. This occurs at a different value of the thickness for each film. For pHs of 3.5, 3.7 and 5.1 the peeling occurs on the downstroke while it occurs on the upstroke when the pH is 2.9 and 4.2. This peeling could be an effect of

molecular reorganisation, similar to that observed by Diaz *et. al.* [12]. For the films produced at pHs of 3.5, 3.7 and 5.1 it was possible that they started off as Y-type, reordered to Z-type (because deposition partially failed on the downstroke) and then switched back to Y-type. This reorganisation could be a result of water entrainment [12]. For the films produced at a pH of 2.9 and 4.2 the film appeared to start off as a Y-type, reordered to X-type (because deposition partially fails on the upstoke) and then continued as a Y-type. Films tend to be X-type in nature if they reorder under water resulting in the film becoming hydrophobic and only depositing on the downstroke if the pH is high [8]. Kurnaz *et. al.* [7] found that changes in pH lead to the formation of pinhole defects in the film. This will be discussed in more detail in the AFM section.

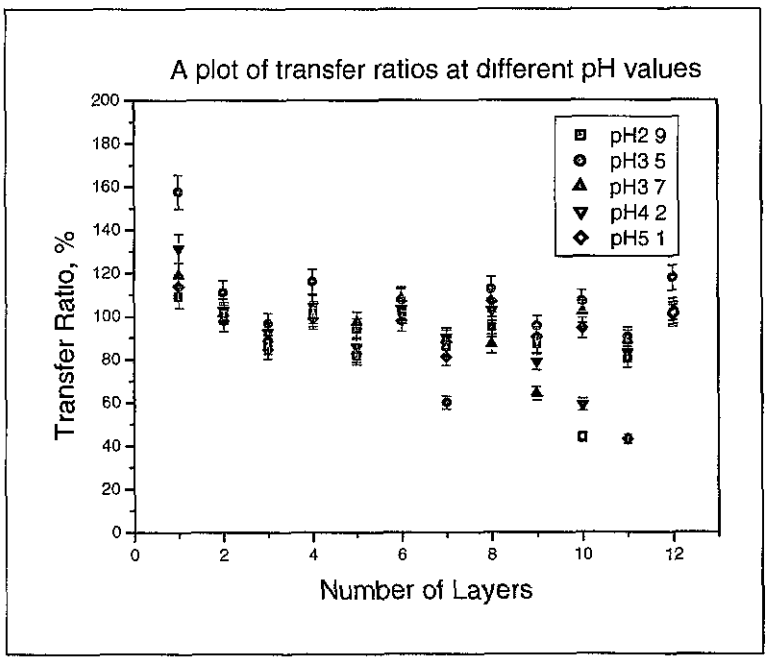

Figure 4.4: A plot of the target pressures over a pH range of 2.9 to 5.1.

The dipper speed during deposition can also play a crucial part in how the monolayer deposits. If the dipper is traveling too fast the monolayer may not have time to deposit fully, on the other hand if it is traveling too slow the monolayer may collapse on itself as it deposits. Experiments were carried out on an ultra pure water subphase with a pH of 6.2. 50 μL of 1mg/ml AA/chloroform was spread on the surface and the layer was compressed to a with a speed of 10 cm^2/min. Films with a

thickness of 12 layers were deposited onto HMDS hydrophobic glass as the dip speed was varied over a range of 10, 15, 20 and 30 mm/min. The results of the experiment are shown in figure 4.5.

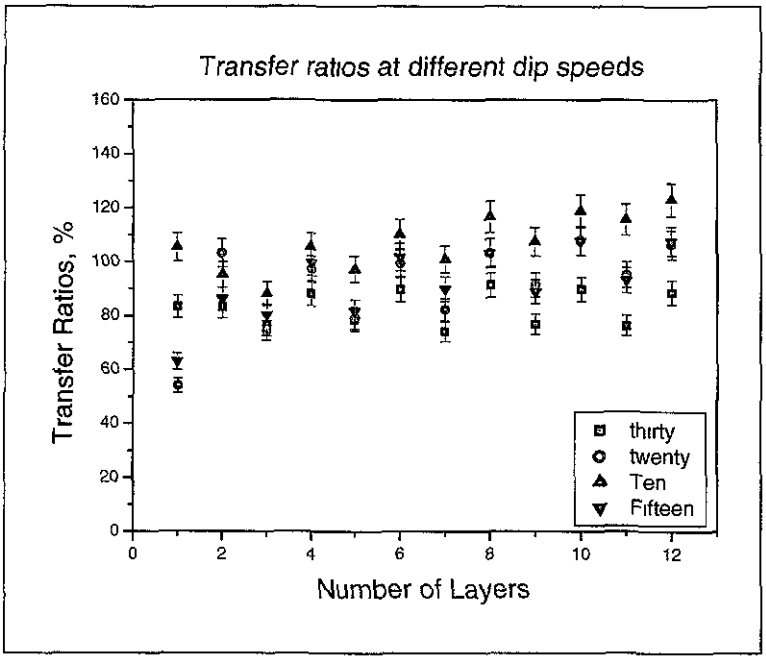

Figure 4.5: A plot of the transfer ratios versus the number of layers when varying the dip speed.

The graph shows that a dip speed of 30 cm^2/min was too fast as the transfer ratios lay around 80%; contrary to this a dip speed of 10 cm^2/min was too slow as the transfer ratios lay above 100%; The optimum dip speed was between 15 cm^2/min and 20 cm^2/min. This experiment was a good example of how the downstroke and upstroke transfer ratios should be similar to each other. Note how there was no layer peeling in this experiment compared to the pH experiment. The films were perfect Y-type films.

As a final experiment, 12 layer films were produced on HMDS treated glass. The dip speed was 20 mm/min and the compression of the monolayer was 10 cm^2/min. 50 µl of AA in chloroform was spread on the surface and the drying time between layers was altered to monitor any significant changes in the transfer ratio. The substrate was held above the subphase anywhere from zero to 6 minutes while there was no delay below the subphase. From figure 4.6 it can be seen that the 9^{th} layer (where the substrate held for 5 minutes) and 10^{th} layer (where the substrate

held one minute) did not follow the general trend of the graph. These layers seem to have deposited poorly in a random fashion. Despite this the overall deposition is satisfactory.

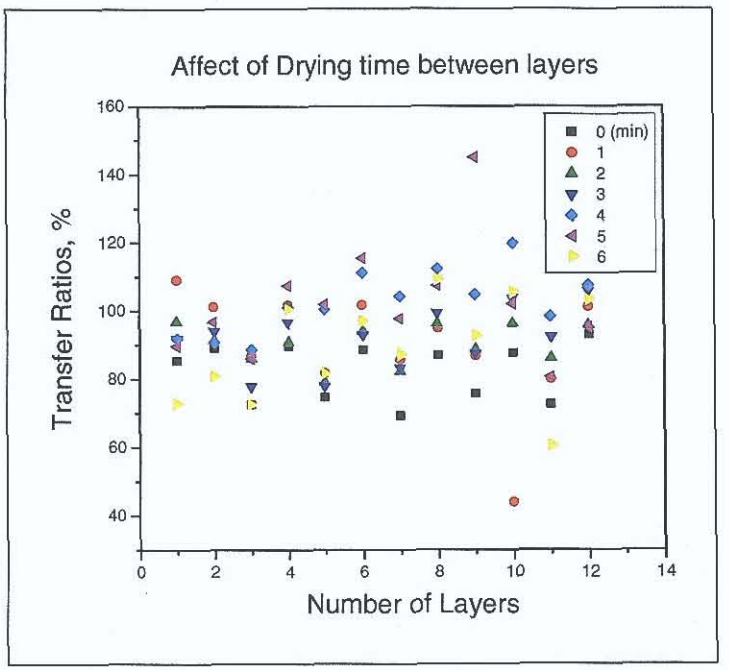

Figure 4.6: A plot of the transfer ratios verses number of layers. The time the substrate was held above the subphase was altered to monitor chances in the transfer ratio.

The best results were obtained by holding the dipper 4 or 5 minutes. Here the transfer ratio is approximately 102%, while for a waiting time of between 1 and 3 minutes the transfer ratio were in the range of 89 to 92%. Since holding the dipper for 4-5 minutes was time consuming and offers no vast improvement in film quality it was felt that holding the dipper by 1-2 minutes would be sufficient in producing LB films.

The above results show how varying the experimental parameters can influence the film quality. The changes due to these parameters were considered when optimising the quality of the CuTTBPc films.

4.2 LB Films of Pure CuTTBPc and mixed CuTTBPc:AA

In recent years interest has grown in use of phthalocyanines (Pcs) in the synthesis of LB films. They have attracted considerable attention in the field of photoconductors, electronic devices and gas sensors [17]. In particular CuTTBPc has been studied, due to its chemical and thermal stability [17], however, aggregation of the CuTTBPc molecules is a problem when trying to produce smooth molecular films. It has been found that the incorporation of fatty acids, such as arachidic acid, stearic acid, can reduce aggregation to some degree and in general improve film quality [17- 20]. Baker *et. al.* [21]were the first to study films of pure CuTTBPc and since then research continues in LB films of pure CuTTBPc films and mixed CuTTBPc films.

4.2.1 Pure CuTTBPc LB Films

For this study all films containing CuTTBPc were produced with the Nima 312D trough. LB films were prepared by spreading 50 μL of a 0.5 mg/ml solution of CuTTBPc in chloroform on ultra pure water. All experiments involving CuTTBPc were carried out at a target pressure of 20 mN/m with a compression speed of 10 cm^2/min. A typical isotherm is shown figure 4.7. In comparison to the isotherm for AA there was no clear distinction between the liquid and solid phase and no obvious collapse of the monolayer could be seen, unlike the AA isotherm where there was a sharp drop in pressure at the point where film collapse occurs. For CuTTBPc it was not possible to run isocycles due to aggregation of the molecules within the monolayer, an example showing the aggregation hysteresis of the CuTTBPc monolayer is found in [22]. Isotherms similar in shape to that in figure 4.7 have been obtained by other groups [17]- [19]. The estimated limiting area per molecule (LAM) of the pure CuTTBPc monolayer was calculated to be 44 $Å^2$ per molecule. This value was in good agreement with those reported by Lee *et. al.*[22] (42 $Å^2$ per molecule), Ku *et. al.* [17] (52 $Å^2$ per molecule) and Emelyanov *et. al.* [23] (66 $Å^2$ per molecule). The variation in the LAM values reported by different groups was attributed to the degree of aggregation within the individual monolayers [17][22]. It was also found that Pc molecules are sensitive to external conditions such as pH and

temperature [24] with slight variations in these parameters giving different LAM values. The collapse of the monolayer occurred at a pressure of ~50 mN/m. The surface pressure continued to rise even after the monolayer had collapsed. This was attributed to the lack of amphiphilic characteristics within the CuTTBPc molecule [17].

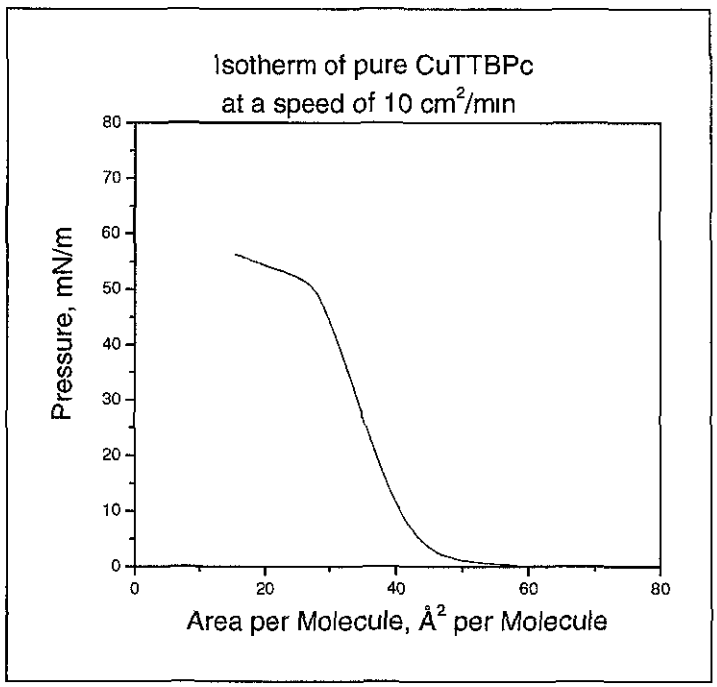

Figure 4.7: The isotherm obtained for pure CuTTBPc on ultrapure water at a compression speed of 10 cm^2/min.

Two 12 layer CuTTBPc LB films were synthesised at a dipping speed of 5mm/min and target pressure of 20mN/m on plasma cleaned hydrophilic silicon for analysis with XPS and NEXAFS. One film had 12 layers deposited continuously onto the substrate. The other film had one layer of CuTTBPc which was allowed to dry on a hotplate at 60°, for 1 hour, before the next 11 layers were transferred. The transfer ratios for both 12 layer films were low (<100%) indicating poor coverage. Figure 4.8 gives the transfer ratios for the 11 layers which were deposited on top of the dried layer. The poor transfer ratios could be attributed to a number of reasons but aggregation was the most likely cause. It appeared from the transfer ratios that both films of pure CuTTBPc were Y-type because deposition is roughly equal on both the up and downstrokes. However, Emelianov *et. al.* [20] found that pure

CuTTBPc films were Z-type, indicating poor deposition on the downstroke but with the incorporation of AA into the monolayer they were able to achieve Y-type films.

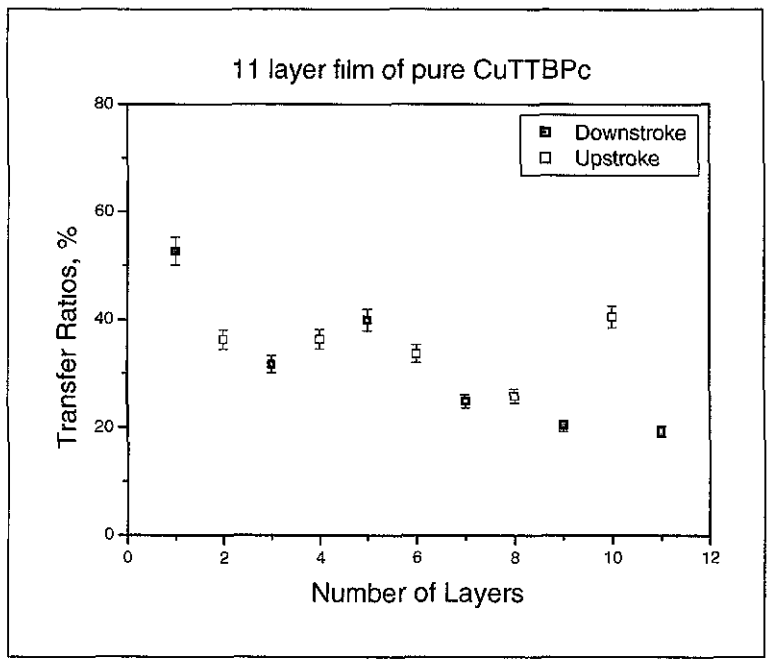

Figure 4.8: An example of the transfer ratios for a Y-type pure CuTTBPc film.

A. V. Nabok *et. al.* [25] stated that the tilt angle of a molecule in a floating monolayer could be calculated using the following equation

$$\theta = \sin^{-1}\left(\frac{l_2 l_3}{A}\right) \tag{4.1}$$

and the thickness of the floating monolayer, d_L, could be calculated using

$$d_L = l_1 \sin\theta + l_3 \cos\theta \tag{4.2}$$

where θ is the tilt angle relative to the subphase surface, l_1 and l_2 are the length and width of molecule, respectively, l_3 is the through plane width of the molecule and A is the limiting area per molecule. T. Wada *et. al.* [26] gave the dimensions of the CuTTBPc molecule to be $l_1 = l_2 = 2.17$ nm and $l_3 = 1.54$ nm. Using these values the tilt angle and thickness were calculated to be 49.42° relative to the subphase surface (or 40.58° relative to the normal) and 2.65 nm, respectively. These values were only rough estimates as they refer to the floating and not the transferred monolayer. More reliable and accurate techniques such as XPS and NEXAFS were used to determine

the tilt angle of CuTTBPc in the 12 layer LB film of pure CuTTBPC, while AFM and ellipsometry was used to calculate thickness in the mixed LB films of CuTTBPc:AA.

4.2.2 LB Films of 1:1 Molar Ratio of CuTTBPc:AA

In an attempt to overcome the aggregation problem a 1:1 molar ratio of CuTTBPc:AA was prepared by mixing appropriate volumes of a 1 mg/ml AA solution in chloroform with a 1 mg/ml Pc solution in chloroform. This was previously found to reduce aggregation [17][18][20] but it should be noted that even within the mixed film of CuTTBPc:AA highly aggregated domains of CuTTBPc still exist [18]. Films ranging in thickness from 1 monolayer to 21 monolayers were grown and studied by ellipsometry (section 5.2) to provide an independent determination of the film thickness. It was found that deposition can be greatly improved by allowing the first layer to dry fully before proceeding with additional layers [18][20][27]. For the films examined here, the first layer was deposited and the substrate was then placed on a hotplate and allowed to dry for one hour at 60° C. Compared to previous experiments this drying did have a positive influence on the deposition of subsequent layers. An experiment was carried out to determine if holding the substrate above the subphase resulted in an improvement in the film quality. The 1, 3 and 5 ML films were held above the subphase for 1 minute as the layers were deposited. This showed no marked improvement in the transfer ratios so the remaining films (7-21 ML) were not held above the subphase.

The shape of the isotherm obtained for the 1:1 molar solution of CuTTBPc:AA was in good agreement what that found by Sheu *et. al.* [18] In figure 4.9 the isotherm for this work showed characteristics of both of the CuTTBPc isotherm and the AA isotherm. There did however seems to be a difference in the LAM which changed from 44 $Å^2$ per molecule for the pure CuTTBPc to 79 $Å^2$ per molecule for the mixed 1:1 molar ratio of CuTTBPc:AA. Sheu *et. al.* obtained a value of approximately 50 $Å^2$ per molecule for 1:1 CuTTBPc:AA. This increase in area indicated that the AA reduces the aggregation of CuTTBPc in the monolayer.

These differences in the LAM values may have been a result of slight variations in experimental procedures or external conditions (pH, temperature etc.).

For the 1:1 CuTTBPc:AA monolayer it appeared that two collapse pressures existed. Emelianov *et. al.* [19] proposed that the mixed monolayer consists of AA molecules with domains of CuTTBPc clusters dispersed throughout the monolayer. Therefore *two* collapse pressures should be found in isotherms of mixed CuTTBPc:AA monolayers. The first collapse was found to occur at approximately 40 mN/m. This was close to the value of 50 mN/m obtained for the collapse of the pure CuTTBPc monolayer. The collapse pressure of a pure AA monolayer was around 60 mN/m. It could be seen that after the collapse at 40 mN/m the pressure rose steadily to a second collapse at 60 mN/m. As the barrier moved in and compressed the monolayer the non-amphillic CuTTBPc molecules could be easily compressed out of the monolayer leaving just AA molecules on the surface. Further compression of the monolayer would therefore exhibit characteristics of an AA monolayer [19].

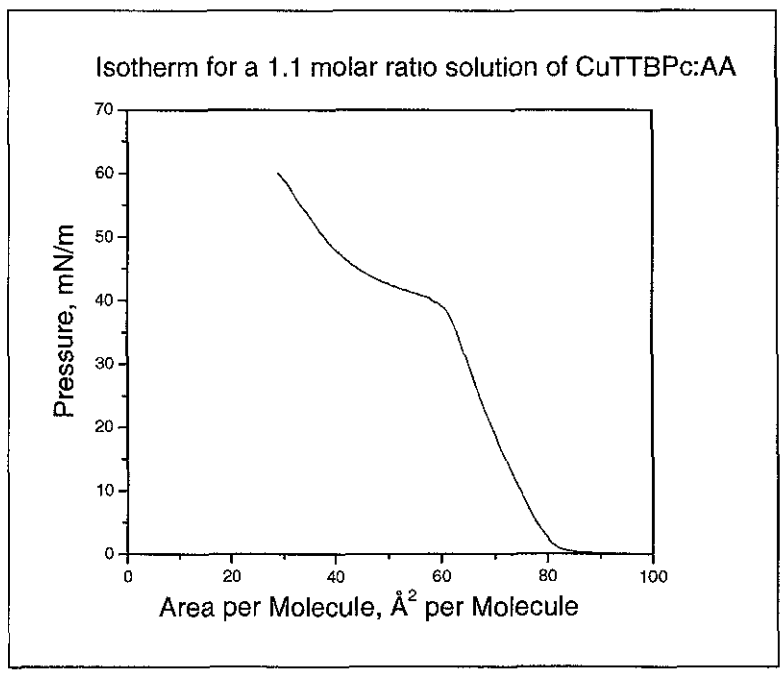

Figure 4.9: Isotherm for a 1:1 molar ratio solution of CuTTBPc:AA.

From the transfer ratios of the 1-21 ML 1:1 CuTTBPc:AA films it was determined that most of the films were Y-type but that they were of poor quality, as

indicated by the relatively low transfer ratios. Emelianov *et. al.* [20] also found that films of CuTTBPc:AA were Y-type in structure. Interestingly, the 17 and 19 layer films appeared to be Z-type. Both films had a much higher transfer ratio on the upstroke in comparison to the downstroke. No explanation can be given for this as it was assumed that they would deposit in a similar fashion to the other films.

Table 4.1 summaries transfer ratios obtained for the 1-21 ML films of 1:1 CuTTBPc.AA. No systematic trend was observed from the transfer ratios.

Thickness, MLs	Upstroke, %	Downstroke, %	Overall Average,%
1	179 34	–	179.34
3	108.91	71 46	96 43
5	78.56	49.13	66 79
7	63.22	42 43	54.31
9	68 57	40.2	55.96
11	48 68	32 57	41.35
13	60 86	34.59	48 73
15	42.09	33 28	37.98
17	121.92	38.39	82.62
19	129.05	53.29	93.16
21	50.99	29 34	40 68

Table 4.1: The average transfer ratios for the 1-21 ML films of 1:1 CuTTBPc:AA. In general the average upstroke and average downstroke are less than 100% indicating a poor surface coverage. From the transfer ratios it appears that the films are Y-type with the exception of the 17 and 19 layer films which appear to be Z-type.

4.2.3 Variation of the Molar Ratio of AA in CuTTBPc:AA

Different molar ratios of CuTTBPc:AA were studied to examine the effect of AA concentration on the shape of the isotherm and on the transfer ratios. Films were produced at a dipping speed of 5mm/min and target pressure of 20mN/m. The isotherms for 1:2, 1:3, 1:4, 1:5, 1:6, 1:7, 1:8, 1:9 and 1:10 molar ratio solutions of CuTTBPc:AA are shown in figure 4.10. The isotherms showed characteristics of both the pure AA and CuTTBPc films. Since the monolayers contained more AA than CuTTBPc the isotherms showed clear characteristics of the AA isotherm with a visible conversion from the liquid to solid phase in the range 27-37 $Å^2$ per molecule. As with isotherms for pure AA the liquid to solid phase transition occurred at approximately 25 mN/m. Characteristics of the CuTTBPc isotherm were also present, with the isotherm collapsing at approximately 40 mN/m. There was a very obvious collapse of the film in the 1:5 and 1:10 isotherms where both isotherms

showed a very sudden and sharp collapse. This was characteristic of the AA isotherm. Emelianov *et. al.* [19] and Sheu *et. al.* [18] obtained similar isotherms for mixtures of CuTTBPc:AA.

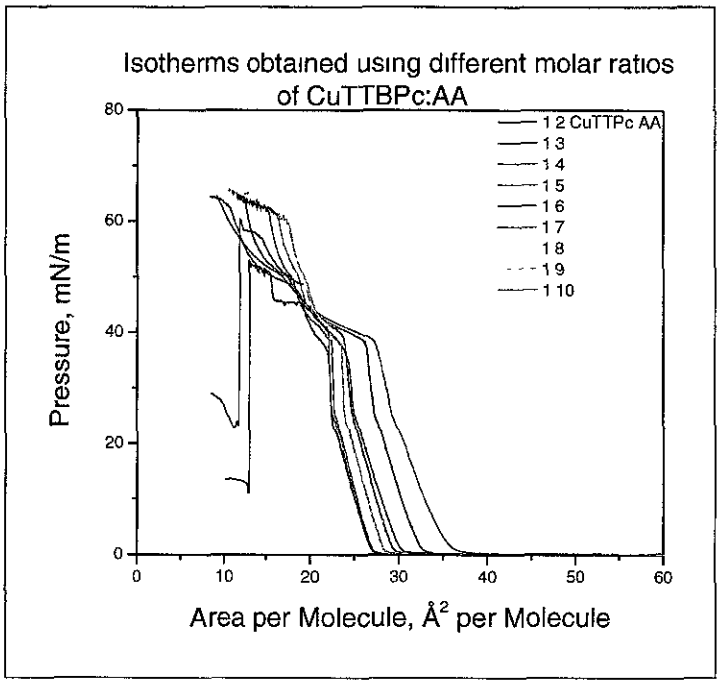

Figure 4.10: The isotherms obtained for 1:2, 1:3, 1:4, 1:5, 1:6, 1:7, 1:8, 1:9 and 1:10 molar ratio solutions of CuTTBPc:AA.

The transfer ratios indicated that the films produced at different molar ratios of 1:X CuTTBPc:AA were poor Y-type. A summary of the transfer ratios transfer is given in table 4.2. As with the 1:1 CuTTBPc:AA no systematic trend was observed with the transfer ratios. It was assumed that the aggregation of the CuTTBPc molecule was responsible for the poor transfer ratios.

Ratio of CuTTBPc:AA	Upstroke, %	Downstroke, %	Overall,%
1 2 Pc·AA	39 64	26.90	33.85
1:3 Pc:AA	19 05	21.02	19.94
1.4 Pc AA	86.03	38 59	64 47
1·5 Pc:AA	70.26	62.06	66.53
1.6 Pc:AA	40.47	9.21	26.26
1 7 Pc:AA	49.67	34.66	42.85
1.8 Pc:AA	32.88	15.73	25.08
1 9 Pc:AA	66.87	18.56	44 91
1:10 Pc:AA	46 19	24.58	36.37

Table 4.2: The transfer ratios for 11 layer films produced using 1:2, 1:3, 1:4, 1:5, 1:6, 1:7, 1:8, 1:9 and 1:10 molar ratio solutions of CuTTBPc:AA

4.2.4 Variation of the Molar Ratio of CuTTBPc in CuTTBPc:AA

Solutions were prepared in which the amount of AA was constant and the amount of CuTTBPc was varied. A series of 11 layer X:1 CuTTBPc:AA films were grown at a dipping speed of 5mm/min and target pressure of 20mN/m. These films appeared to be Y-type from the transfer ratios. Isotherms for 2:1, 3:1, 4:1, 6:1 and 8:1 molar ratio solutions of CuTTBPc:AA are shown in figure 4.11. These isotherms exhibited the characteristics of a CuTTBPc isotherm more than that of an AA isotherm. This was to be expected as the amount of CuTTBPc had increased compared to AA. All the isotherms reached a plateau at approximately 30 mN/m and collapsed around 60 mN/m with the exception of the 4:1 and 8·1 films. Similarities in the shape of theses isotherms and those of Sheu *et. al.* [18] were observed.

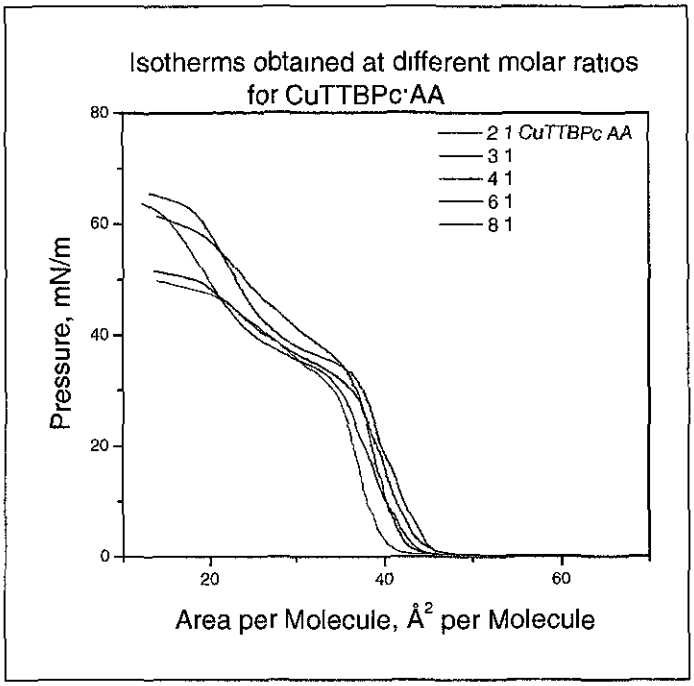

Figure 4.11: The isotherms obtained for 2:1, 3:1, 4:1, 6:1 and 8:1 molar ratio solutions of CuTTBPc:AA.

There was slight improvement in the transfer ratios compared to the 1:X CuTTBPc:AA films. A summary of the transfer ratios is shown in table 4.3.

Ratio of PC:AA	Upstroke, %	Downstroke,%	Overall, %
2 1 Pc:AA	59.20	53.58	56.65
3 1 Pc AA	56.33	48.18	52.62
4 1 Pc AA	59.40	46.34	53 46
6 1 Pc AA	89 52	55.06	73.85
8 1 Pc.AA	57 76	56.53	57.2

Table 4.3: The transfer ratios obtained for 11 layer films produced using 2:1, 3:1, 4:1, 6:1 and 8:1 molar ratio solutions of CuTTBPc:AA.

4.3 Conclusions

For the pure AA films, grown in DCU on the Nima 2022 bath, Y-type films were usually formed regardless of speed, pH or drying time. Certain dipping conditions such as the dip speed could be optimised to improve the transfer ratio. Alterations in the drying time showed that allowing the film to dry between dips improved the film quality. Changes in pH did not play a significant role in the film quality or film type. It should be noted that to see a significant change in the film

(both on the subphase and on the substrate) due to pH changes the addition of cations to the subphase is necessary [6][9][10][11][12].

The isotherms obtained for both the pure and mixed films were in good agreement with other publications [17][18][19][22]. The presence of both CuTTBPc and AA could be seen in the mixed monolayer isotherms. Films produced with the pure CuTTBPc showed evidence of aggregation both in the isotherms and in the transfer ratios. These films were predominantly Y-type in configuration. The pure LB films of CuTTBPc were studied by AFM, NEXAFS and XPS to determine the surface topography, tilt angle and molecular orientation of CuTTBPc. These results are discussed sections 5.1.1, 6.4 and 6.5, respectively. The NEXAFS and XPS results for the LB film were compared to the results of evaporated films of CuTTBPc.

The incorporation of AA into the CuTTBPc films was investigated as a method of reducing film aggregation and improving the transfer ratios. These film were grown in Nottingham University on the Nima 312D bath. It was oberved from the isotherms that the AA decreased aggregation slightly but there was little improvement in the transfer ratios when AA was mixed with the CuTTBPc. It should be noted that the Nima 312D Model trough uses a dipper where ***both*** the front and back surfaces of the substrate are coated with the monolayer.The transfer ratio is then averaged for both sides. For these experiments polished silicon wafers were used but only one side of the silicon was polished and plasma cleaned. In this case the films transfer differently on to each side of the substrate and hence there would be an error in the transfer ratio. For this reason the film quality was not judged solely by the transfer ratio but also from AFM and ellipsometry measurements, as discussed in sections 5.1.2 and 5.2.

Chapter Four References

[1] K.B Blodgett, ***Physical Review***, 55, (1939) 391.

[2] R H Tredgold, ***Reports on Progress in Physics***, 50 (1987) 1609-1656.

[3] L. Bourdieu, P. Silberzan and D. Chatenay, ***Physical Review Letters***, 67, No 5 (1991) 2029-2031.

[4] D. K. Schwartz, J. Garnaes, R. Viswanathan, S. Chiruvolu and J. A. N. Zasadzınski, ***Physical Review E***, 47, No. 1 (1993), 452-460.

[5] A. Schaper, L. Wolthaus, D. M. Bbius, and T M. Jovin, ***Langmuir***, 9 (1993) 2178-2184.

[6] T Kajiyama, Y. Oishi, M. Uchida and Y. Takashima, ***Langmuir***, 9 (1993) 1978-1979.

[7] M. L. Kurnaz and D. K. Schwartz, ***Journal of Physical Chemistry***, 100 (1996) 11113-11119.

[8] S. Evenson, J. P. S. Badyal, C. Pearson, and M. C. Petty, ***Advanced Materials***, 9, No. 1 (1997) 58-61.

[9] H-G Liu, C-G Yang, K-Z Yang, ***Colloids and Surfaces A: Physicochemical and Engineering Aspects***, 150 (1999) 137-142.

[10] S. Katholy, J Reiche , L. Brehmer, ***Colloids and Surfaces A: Physicochemical and Engineering Aspects,*** 171 (2000) 87–95.

[11] D. Y. Takamoto, E. Aydil, J. A. Zasadzinski, A. T. Ivanova, D. K. Schwartz, T Yang, P. S. Cremer, ***Science***, 293 (2001) 1292-1295

[12] M. Elena Dıaz, B. Johnson, K. Chittur, and R. L. Cerro, ***Langmuir***, 21 (2005) 610-616.

[13] R. Çapan , Y. Açıkbaş, M. Evyapan, ***Material Letters***, 2006 Article ın press

[14] C-W Chen, T-J Liu, ***Journal of Colloid and Interface Science***, 298 (2006) 298–305.

[15] M. Elena Diaz and Ramon L. Cerro, ***Thin Solid Films,*** 460 (2004) 274–278.

[16] Nima Technology, **Tensiometers and Langmuir-Blodgett Troughs**, Operating Manual, 4th Edition, 1995.

[17] Y-L Lee, Y-C Chen, C-H Chang, Y-M Yang, J-R Maa, ***Colloids and Surfaces A: Physicochemical and Engineering Aspects,*** 191 (2001) 223-231.

[18] C-W Sheu, K-M Lin, I-H Ku, C-H Chang, Y-L Lee, Y-M Yang, J-R Maa, ***Colloids and Surfaces A: Physicochemical and Engineering Aspects*** 207 (2002) 81–88.

[19] I.L. Emelianov, V.V. Khatko, ***Thin Solid Films***, 354 (1999) 237-244.

[20] I Emelianov , V Khatko, A Tomchenko, ***Sensors and Actuators B***, 47 (1998) 158–163.

[21] S. Baker, M. C. Petty, J. J. Roberts, M. V. Twigg, ***Thin Solid Films***, 99 (1983) 53-59.

[22] Y-L Lee, Y-C Chen, C-H Chang, Y-M Yang, J-R Maa, ***Thin Solid Films,*** 370 (2000) 278-284

[23] Yu. L. Emelyanov, V. V. Khatko, A. A. Tomchenko, ***Synthetic Metals,*** 79 (1996) 173-175.

[24] J. J. Burack, J. D. LeGrange, J. L. Markham, W. Rockward, ***Langmuir***, 8 (1992) 613.

[25] A. V Nabok, A. K. Ray, A. K. Hassan, J. R. Travis, ***Supramolecular Science***, 4 (1997) 407-411.

[26] T. Wada, T. Higo, K. Irokawa, T. Kimura, M. Yamashita, ***Japanese Journal of Applied Physics***, 43, No. 7A (2004) 4312-4315.

[27] I.L Emelianov, V. V. Khatko, ***Sensors and Actuators B***, 60 (1999) 221-227.

Chapter 5

An AFM and Ellipsometry Study of CuTTBPC:AA LB Films plus an STM study of pure CuTTBPc

Chapter 5 reveals how topographical, orientation and height studies were carried out using the AFM, STM and ellipsometer. The AFM images of the mixed films of CuTTBPc:AA are discussed in sections 5.1.2 to 5.1.3 where the films possessed both AA and CuTTBPc characteristics. The change in surface roughness was studied as the thickness of the films increased Ellipsometry was used to calculate film thickness and to investigate the presence of a layer-by- layer growth structure. The results are given in section 5.2.2 and 5.2.3. An STM study of pure CuTTBPc, section 5.3.3, on Ag/Si(111)R30°(√3 x √3) revealed a highly ordered and densely packed surface which has previously been unreported in literature. Section 5.3.5 reports on the findings of an STS study of CuTTBPc on Ag/Si(111)R30°(√3 x √3) which was used to calculate the HOMO-LUMO bandgap.

5. 1 An AFM Study of LB films

5.1.1 AFM Study of Pure CuTTBPc LB films

Films with a thickness of 12 MLs of pure CuTTBPc were grown on plasma cleaned silicon. The isotherms recorded for the CuTTBPc suggested that aggregation within the CuTTBPc monolayer existed. This aggregation was therefore expected to be observed in the AFM images of these films. Tapping mode AFM is a non-destructive technique and is ideal for imaging these films. In agreement with other researchers [1][2][3] and the LB isotherms measured in this work, clusters of material were found in AFM images of pure CuTTBPc as shown in figure 5.1 taken from a 12 layer film. The surface coverage is good and spherical clusters varying in size are uniformly distributed on the surface. The width of the clusters varied from a maximum of 560±1.49 nm to a minimum of 150±2.62 nm.

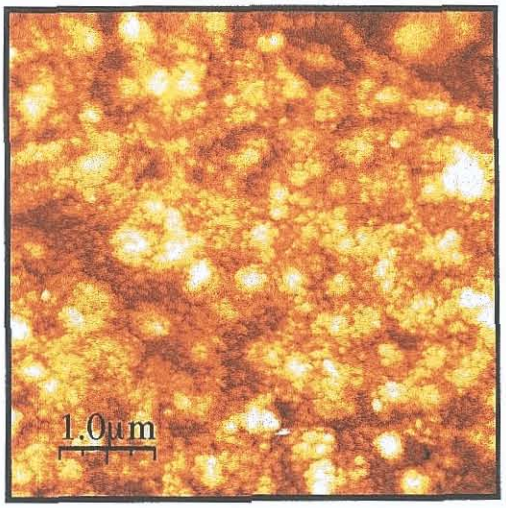

Figure 5.1 : A 5 µm^2 scan of a pure CuTTBPc film with a thickness of 12 monolayers.

5.1.2 AFM Study Mixed LB Films of 1:1 CuTTBPc: AA

By mixing the CuTTBPc with AA, in a molar ratio of 1:1, the clusters were expected to disperse as AA reduces aggregation. The films were expected to have characteristics of both the AA surface and the CuTTBPc surface as seen with the LB isotherms. Emelianov *et. al.* [2] proposes that the height of the mixed film is determined by the AA as the CuTTBPc molecules are hydrophobic and are squeezed out of the film by the AA molecules, as shown in figure 5.2. This suggests that a mixed monolayer height should be approximately 2.7 nm. In other work carried out by Emelyanov *et. al.* [3], a 25 layer 1:1 CuTTBPc:AA film was studied by means of X-ray reflectrometry and the monolayer height was calculated to be 2.39 nm. They suggested a tilt in the AA molecule is responsible for this reduction in height.

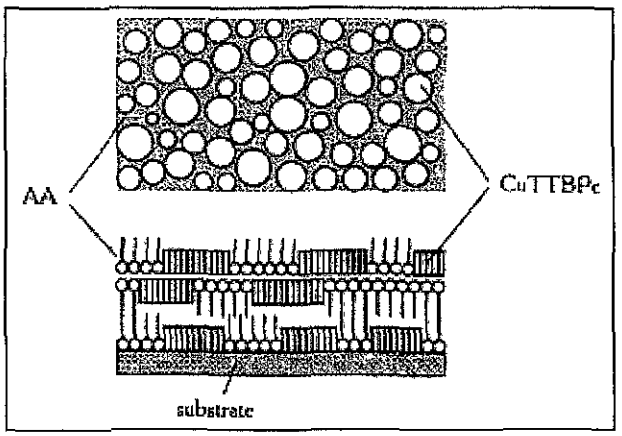

Figure 5.2: The proposed structure of a mixed CuTTBPc:AA film [2].

In contrast to these finding where the AA determines the height of the monolayer the 1 layer film of 1:1 CuTTBPc: AA in this research had a height of 1.70 (±0.04) nm, which was in good agreement with the height of the pure CuTTBPc monolayer as found by Li *et. al.* [4] (1.7 nm) and Emelianov *et. al.* [5] (1.65 nm) using XRD. Figure 5.3 shows a 5 μm^2 AFM image and height profile for a monolayer of 1:1 CuTTBPc:AA. The differences in thickness could be a result of the varying degree of aggregation within the individual films. The height of approximately 1.7 nm found in this research would suggest that the CuTTBPc molecules were the determining factor where height was concerned. In chapter 4 equation 4.1 was used to calculate the thickness of the floating monolayer of pure CuTTBPc and this was found to be 2.65 nm. Therefore there was a difference between the thickness of the floating and transferred monolayers which was attributed to a difference in the tilt angle of the molecule on the subphase and substrate. The one ML 1:1 CuTTBPc:AA film did resemble an AA film in that the surface appears smooth and pinhole defects were present. In addition, small clusters were uniformly distributed throughout the surface which could result from CuTTBPc molecules. A surface roughness analysis gave an RMS (route mean square) roughness of 0.64 nm. Lee *et. al.* [1] obtained a roughness value of 0.74 nm for a pure CuTTBPc monolayer. RMS roughness is a measure of the surface roughness/smoothness of a material. The RMS roughness describes the fluctuations around an average surface height and is the standard deviation or the square root of

the second cumulant (or variance) in terms of statistics. The higher the RMS value the rougher the surface.

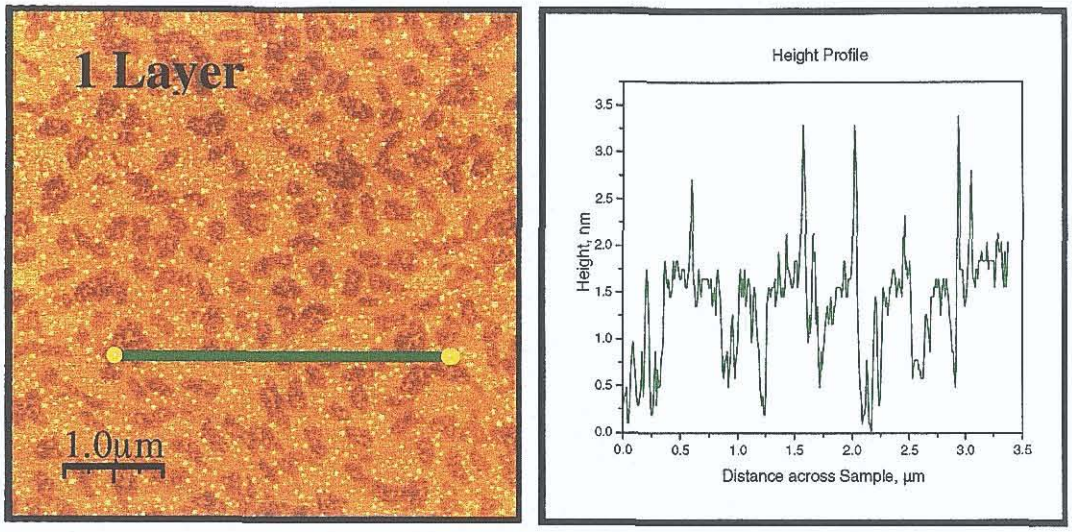

Figure 5.3: 5 µm^2 scan of a 1 layer film of 1:1 CuTTBPc:AA and its height profile.

An AFM image of a 3 layer film, shown in figure 5.4, had a rougher surface than the 1 layer sample. As the layers deposited it was possible that they breaking up due the surface roughness of underlying layers. The 3 layer film did, however, exhibit both AA and CuTTBPc characteristics in that smooth AA domains exist along side clusters of CuTTBPc.

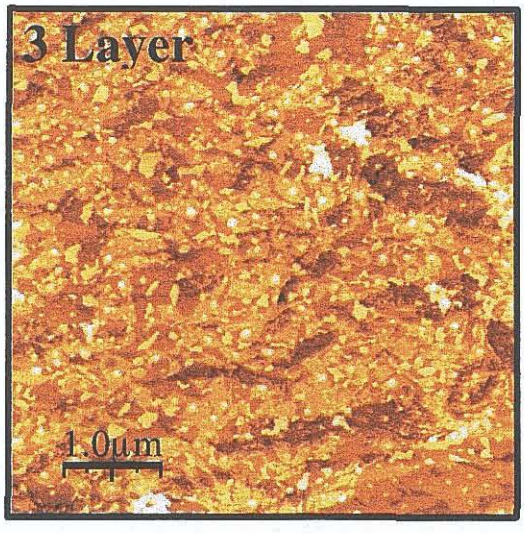

Figure 5.4: 5 µm^2 of a 3 layer 1:1 CuTTBPc:AA film. This film appeared to have a rougher surface than the monolayer film. Domains of CuTTBPc can be seen on the surface and the layer seemed to be disintegrate upon deposition, possibly due to the increasing roughness of the underlying layers.

The clusters of CuTTBPc were very evident in the 5 layer film. They were found on top of the AA regions of the film, as predicted by Emelianov *et. al.* [2]. These clusters also appear in the 7, 9 and 11 layer films but they were less obvious and smaller in the 7 layer film, as can be seen in figure 5.5.

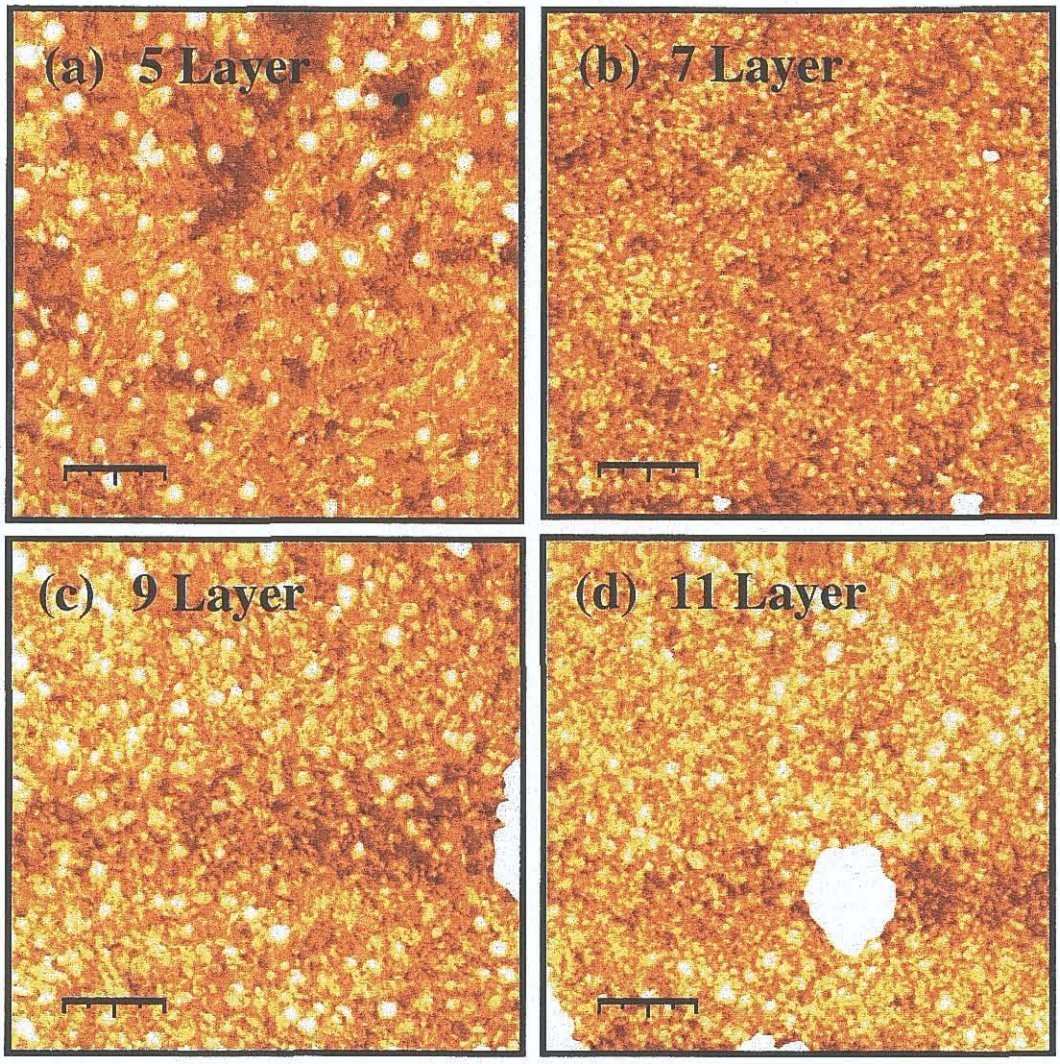

Figure 5.5: 5 μm^2 AFM scans of 1:1 CuTTBPc:AA where (a) is a 5 layer film, (b) is a 7 layer film, (c) is a 9 layer film and (d) is an 11 layer film.

For the higher coverage films the surface appeared rougher and possessed more CuTTBPc characteristics than AA. It should be noted that these films usually had large pieces of debris on the surface, again a sign the film was disintegrating as it deposited. Figure 5.6 shows typical AFM images of the 13, 15, 17, 19 and 21 layer films.

For the higher coverage films the surface appeared rougher and possessed more CuTTBPc characteristics than AA. It should be noted that these films usually had large pieces of debris on the surface, again a sign the film was disintegrating as it deposited. Figure 5.6 shows typical AFM images of the 13, 15, 17, 19 and 21 layer films.

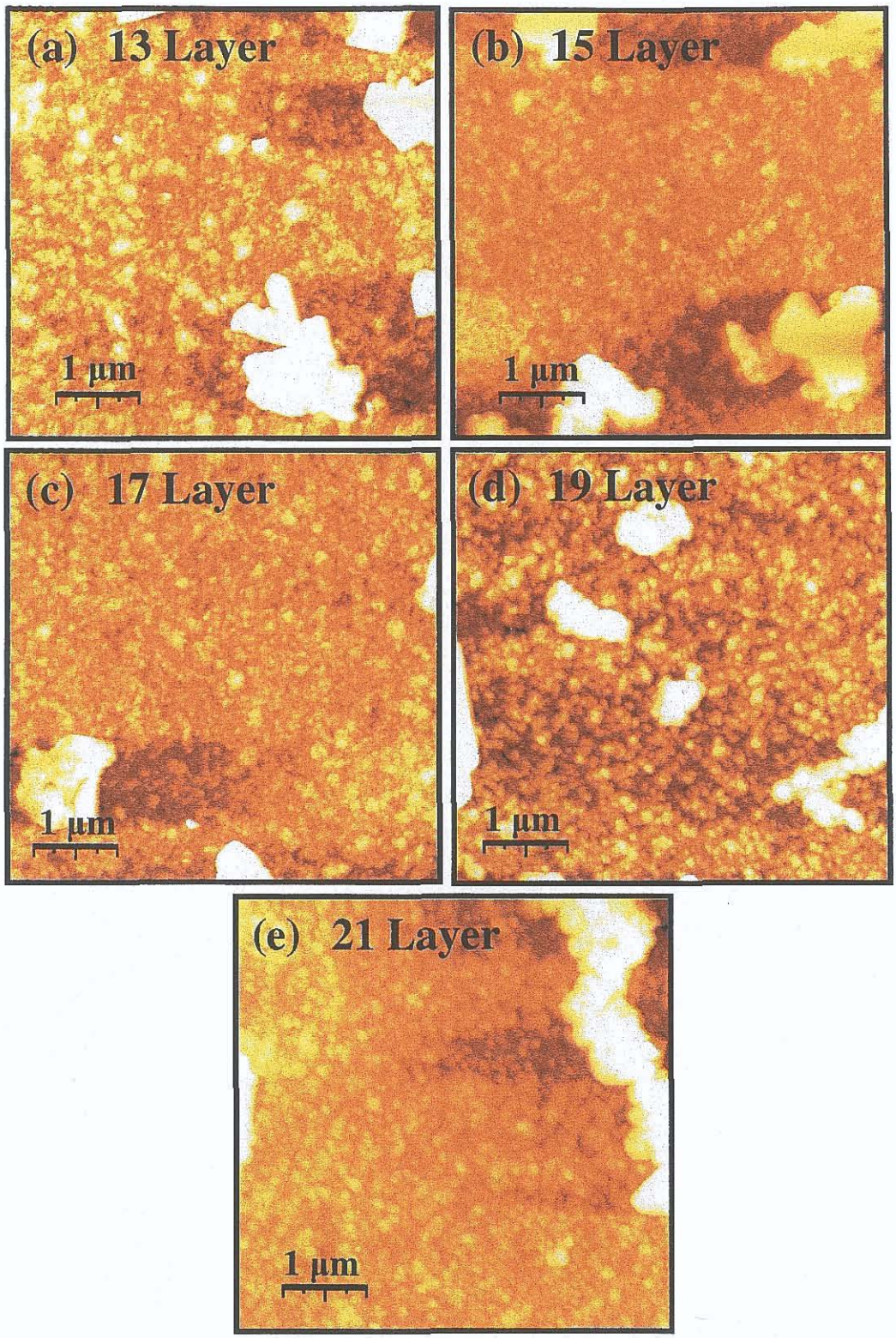

Figure 5.6: 5 µm^2 images for the (a) 13, (b) 15, (c) 17, (d) 19 and (e) 21 layer films. Note the presence of debris on the surface.

5.1.3 AFM Study of 1:X and X:1 LB Films of CuTTBPc: AA

A systematic study was carried in which the amount of AA was increased with respect to the amount of CuTTBPc to grow 11 layer LB films. When the molar ratio lay between 1:2 and 1:6 the surfaces tended to be uneven with the presence of clusters. When the molar ratio of AA was increased in the range of 1:7 to 1:10 of the films took on a smoother appearance.

Films with molar ratios of 2:1, 3:1, 4:1, 6:1 and 8:1 CuTTBPc:AA were also studied. In these films clusters of CuTTBPc could be seen on the surface. The 2:1 CuTTBPc:AA film appeared to be the smoothest but the remaining films look similar regardless of the amount of CuTTBPc used.

Figure 5.7 shows some examples of the films produced using different molar ratios of CuTTBPc:AA. Extreme examples are shown here to highlight how the change in the molar ratio can affect the surface composition

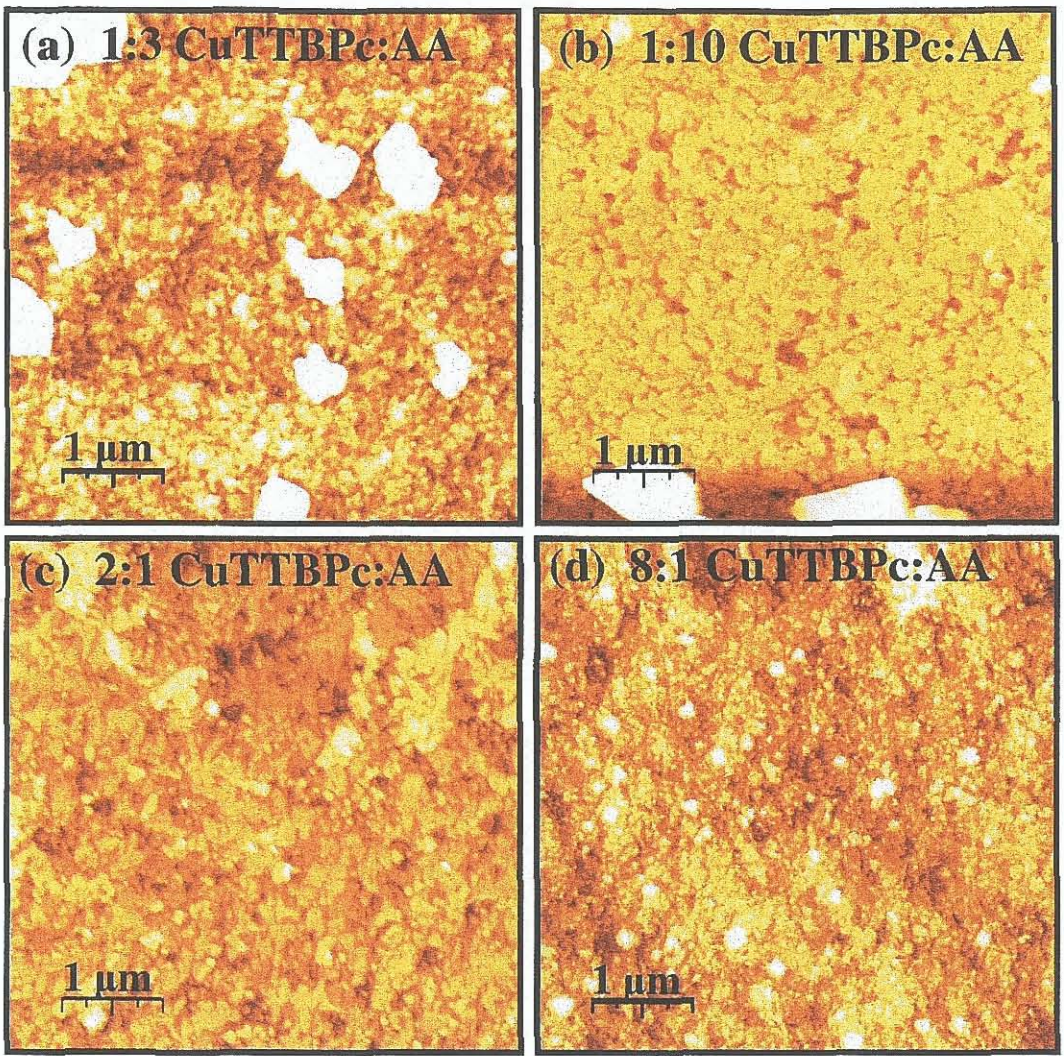

Figure 5.7: 5 µm^2 scans showing how the topography of the surface changes with changing the molar ratio of CuTTBPc:AA. Going from 1:3 CuTTBPc:AA (a) to 1:10 CuTTBPc:AA (b) produced a smoother surface as while going from 2:1 CUTTBPc:AA (c) to 8:1 CuTTBPc:AA (d) produced a rougher surface with the presence of more clusters.

Table 5.1 gives the RMS values for the above AFM images. These values confirm that the roughness of the surface for the 1:1 CuTTBPc films increased as the thickness increased. They also show that the RMS values decreased as the amount of AA in the film increased and that the RMS values increased and as the amount of CuTTBPc increased.

Film Type	Thickness, ML	RMS value (±0.05)
Pure CuTTBPc	12	7.45
1:1 CuTTBPc:AA	1	0.64
1:1 CuTTBPc:AA	3	1.56
1 1 CuTTBPc.AA	5	2.65
1:1 CuTTBPc AA	7	3.17
1:1 CuTTBPc:AA	9	6.90
1:1 CuTTBPc:AA	11	8.25
1:1 CuTTBPc:AA	13	9.59
1:1 CuTTBPc:AA	15	9.40
1 1 CuTTBPc.AA	17	9.22
1:1 CuTTBPc.AA	19	8.73
1:1 CuTTBPc:AA	21	10 53
1 3 CuTTBPc:AA	11	10.26
1:10 CuTTBPc.AA	11	9.36
2:1 CuTTBPc AA	11	2.24
8:1 CuTTBPc:AA	11	3.41

Table 5.1: The RMS roughness values for the various LB films.

5.2 An Ellipsometry Study of CuTTBPc:AA LB films

Ellipsometry is a non-destructive technique used to determine the thickness of the mixed CuTTBPc:AA films. LB films ranging from 1-21 MLs were grown using a 1:1 molar ratio of CuTTBPc:AA. The AFM results suggested that the 1 ML film was relatively smooth with the presence characteristic pinhole defects. As the thickness of the film increased it appeared that islands were forming on the surface. This would indicate that films were Stranski-Krastanov in nature. By calculating the exact thickness of each LB film and observing the layer by layer growth it was possible to determine the presence of molecular ordering within the LB films. An investigation of the effect of varying the molar ratio on the film thickness was also performed. This was done by studying the thickness of a set of 11 layer films produced using different molar solutions of CuTTBPc:AA. The optical constants, n and k, were determined for each film.

5.2.1 Ellipsometry Model

To extract the film thickness and the optical constants, n and k, from the ellipsometrical data a model of the film was proposed. The model allows the user to fit a curve to the experimental data.

The software for the Jobin Yvon ellipsometer contains a library which has pre-installed models for different materials and geometries. Phthalocyanines are considered to be dyes by nature and therefore should exhibit a high optical absorption in the visible range. Literature has shown that two absorption peaks exist for CuPc [6][7] and its various derivatives, such as tetrabromo-tetraalkoxyl substituted CuPc (TBTACuPc), tetraalkoxyl substituted CuPc (TACuPc)[8], copper-tetrakis(3,3-dimethylbutoxycarbonyl phthalocyanine (Cu(dmbc)Pc) [9][10] and CuTTBPc [4]. The absorption peaks for CuTTBPc are found at around 340-350 nm and 620 nm and are attributed to the Soret band and Q-band respectively. It is widely accepted that these peaks results from the $\pi \rightarrow \pi^*$ transitions of the macrocyclic system of the Pc ring which is made up of carbon and nitrogen atoms. Wu *et. al.* [8],Manno *et. al.* [9]. and Rella [10] *et. al.* studied Cu(dmbc)Pc and suggested that the Q-band absorption peak at 620 nm was "caused by the formation of dimmers or higher aggregates", while Li *et. al.* [4] undertook a study involving CuTTBPc and suggested the broad Q-band peak is linked to the 1D linear stacking of the Pc system. This indicated a certain degree of ordering in the films. The Q- and Soret bands were observed in the fit for the LB model for this work. A double amorphous dispersion formula was used for the CuTTBPc:AA film. Since the LB films were prepared on silicon the crystalline silicon data from the materials library was used as the substrate. A silicon oxide layer was also included as part of the substrate. The reference files provided for the crystalline silicon and the silicon oxide layer were sufficient to model the substrate. When building a model of the LB layer a number of factors were taken into account. The chi squared value was used to check the reliability of the model. Any value below 10 is an acceptable value for the chi squared. The correlation of the fit was also examined and was within reasonable limits suggesting that the model was accurate. Since it was known that the CuTTBPc molecule formed aggregates allowance was made for this by means of incorporating

a "void" into the model. A void provided for gaps or pits on the surface. In the model the surface consisted of 50% void and 50% CuTTBPc. Observations were made on correlation and chi squared value to check if the void improved the goodness of the fit. There was no marked improvement by the introduction a void. This was also observed by Djurisica *et. al.* [7] when they studied CuPc so for simplicity the void on the surface was ignored. Figure 5.7 shows a typical output from the modelling software for the one layer 1:1 CuTTBPc:AA film. The chi squared value of 0.116 indicates a good fit. It should be noted that as the films increased in thickness (greater than 15 layers) the chi-square value increased. This is attributed to aggregation in the film.

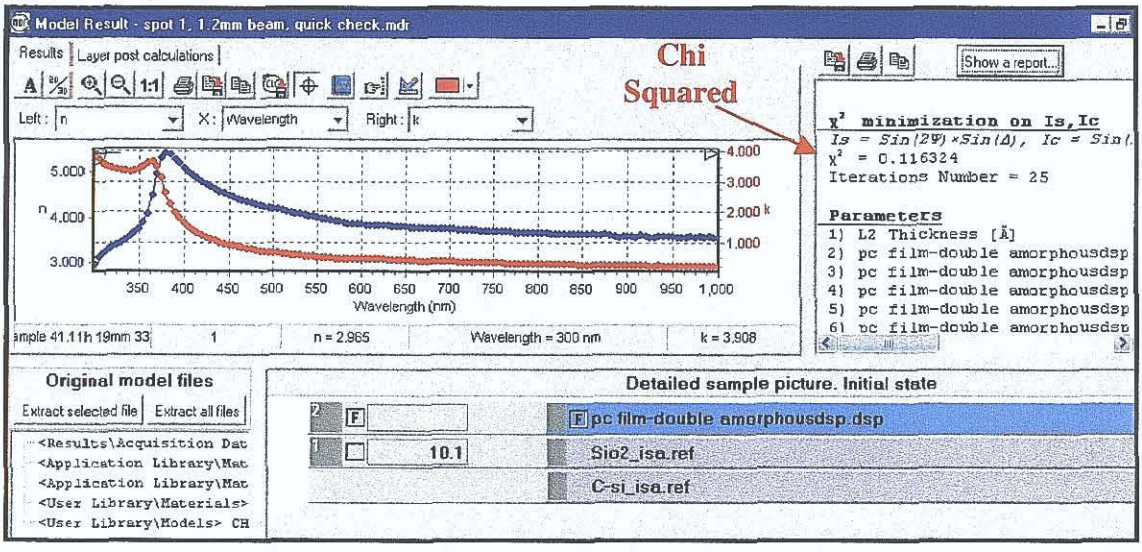

Figure 5.8: A screen capture of the model used.

An example of the fit for a one layer 1:1 CuTTBPc:AA film is shown in figure 5.9. The experimental data is represented by blue and red dots while the fit is drawn as a continuous line. I_s represents $\sin^2\Psi\sin\Delta$ while I_c is $\sin^2\Psi\cos\Delta$.

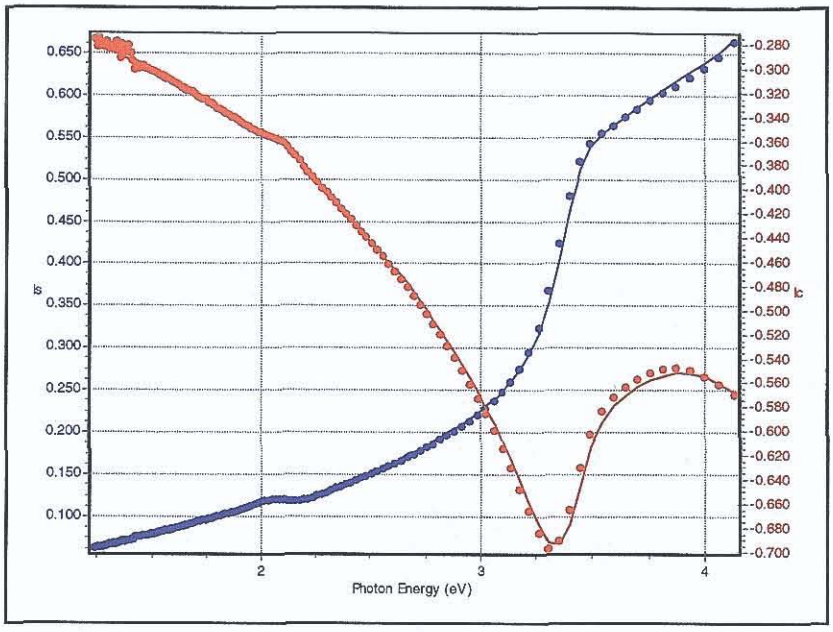

Figure 5.9: The fit for the one layer 1:1 Pc: AA film. The experimental data is represented in blue and red dots while the fit is drawn in a continuous line. From visual inspection this is a satisfactory fit.

For this particular set of mixed CuTTBPc and AA LB films it appeared that there is a small peak around 300 nm and no peak at 340 nm. The presence of AA could have shifted the peak from 340 to 300 nm but due to experimental limitations a scan of the peak at 300 nm was not possible. Nabok *et. al.* [11] studied octa-substituted metal free phthalocyanines where the substitution groups contained alkyl chains which had different lengths. It was found that even small changes in the alkyl chain length (ie C6 to C8) produced large changes in the Q-band shape. The absorption peaks for this research are shown in figure 5.10.

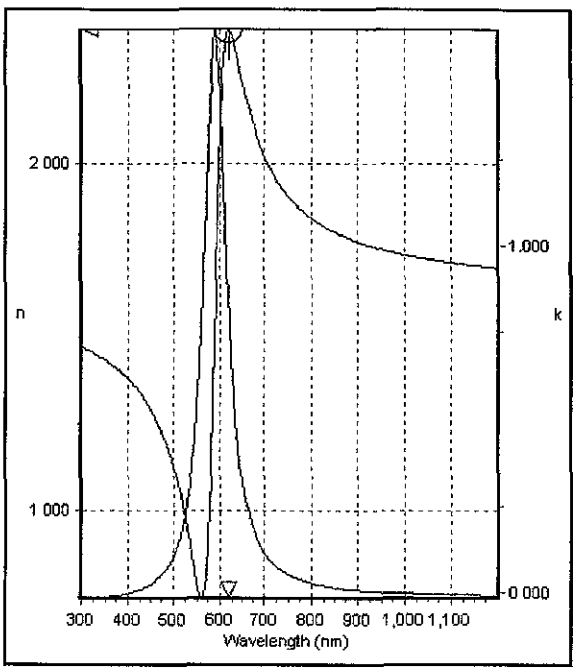

Figure 5.10: The absorption peaks for the Pc:AA films.

5.2.2 Ellipsometry Study of 1:1 CuTTBPc:AA LB films ranging from 1-21 MLs.

Figure 5.11 shows the thickness of the 1:1 CuTTBPc:AA films, extracted from the model results and plotted as a function of the number of monolayers. The linear graph indicates that the film grew in a layer by layer fashion despite the obvious aggregation that has been discussed in the LB and AFM sections. Lee *et. al.* [1] observed a linear growth pattern when carrying out ellipsometry measurements on films of pure CuTTBPc films. Linear growth has also been found in LB films of Cu(dmbc)Pc [10].

It should noted the scan size of the AFM images was 5 μm, while the spot size of the ellipsometer was 1.2 mm. The measurements taken with the ellipsometer were averaged, so that high areas (or clusters) would be averaged against low areas (or pits in the case of the LB films). This explains why the thickness of the one layer film of 1:1 CuTTBPc:AA is 1.7 nm in the AFM image and approximately 4 nm in the ellipsometer. For this reason the slope of graph was used to calculate the average layer thickness instead of relying on individual ellipsometry data points. The average layer thickness, as calculated from the slope of the graph, was 2.19 (± 0.16) nm. This

value was in better agreement with the average AFM value of 1.7 nm and the theoretical value of 1.7 nm. The difference in the ellipsometry and AFM value was due to the averaging process discussed above.

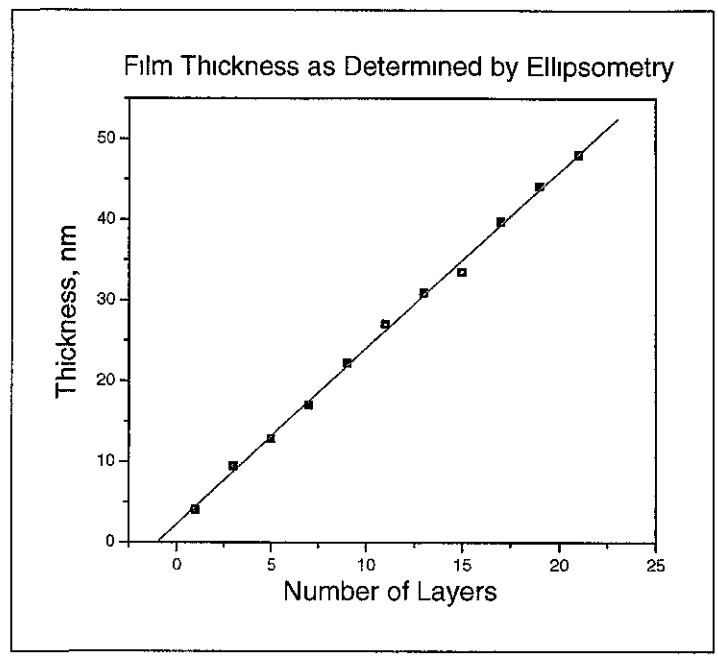

Figure 5.11: A plot of thickness versus number of layers for films grown with 1:1 Pc:AA.

The n and k values were extracted from the model and are shown in figure 5.12. It can be seen that the k values gradually increased and reached a constant value of 1 57 after the 11^{th} layer. The value of the refractive index decreased and had not attained a constant bulk value even after 20 layers had been deposited. The average n and k values for films with a thickness of 11 layers or higher were 2.21 and 1.57, respectively.

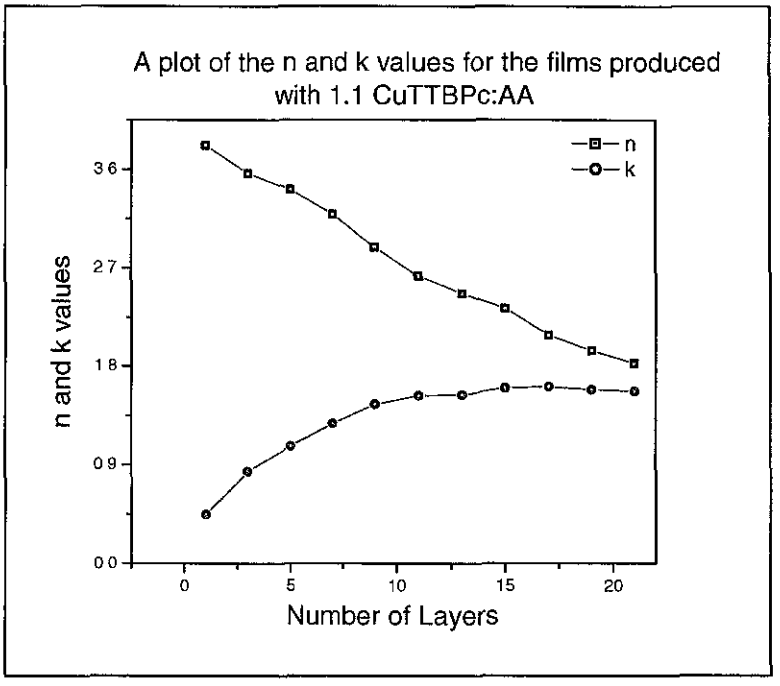

Figure 5.12: A plot of n and k versus number of layers for the 1:1 Pc:AA films.

5.2.3 Ellipsometry Study of 11 ML 1:X and X:1 LB Films of CuTTBPc: AA

The thickness and n and k values were studied for a series of 11-layer films produced by varying the CuTTBPc concentration while keeping the AA constant and vice-versa. The thickness of the 1:X CuTTBPPc:AA films were almost independent of AA concentration with an average thickness of 25.87 nm for the 11 layer film, giving an average monolayer thickness of 2.35 (± 0.14) nm. Variations in aggregation and changes in the film quality may be responsible for this value being higher than 2.19 nm noted above. Also note that the 1:6 CuTTBPc:AA film was of poor quality. Even with the naked eye this particular film showed non uniform regions across the surface. The ellipsometry results for 11 layers 1: X CuTTBPc:AA films are shown in figure 5.13. The average values determined for n and k were 2.84 and 1.52, respectively.

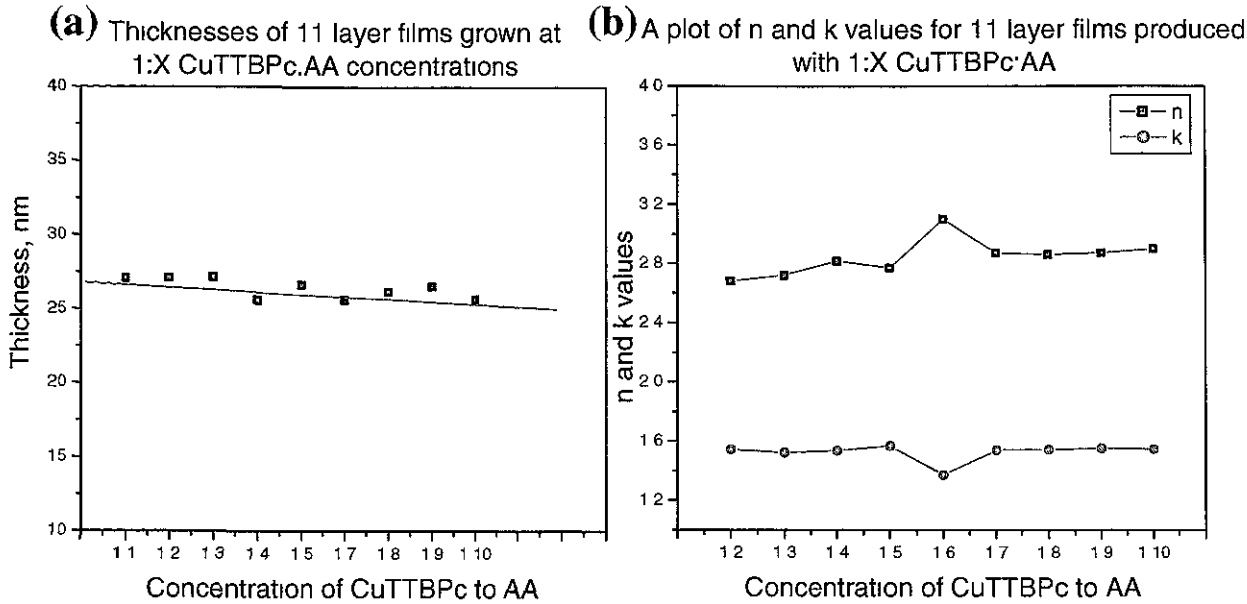

Figure 5.13: (a) The thickness of the 11 layer films grown at different concentrations. The films have an almost constant thickness with the exception of the 1:6 CuTTPc:AA film. (b) The n and k values are almos constant, again with the exception of the 1:6 CuTTBPc film, which appeared to be a bad film.

The thickness of the 11 layers of X:1 Pc:AA films was studied as a function of CuTTBPc concentration. Again the thickness was found to be almost independent of Pc concentration with an average value of 26.2 nm, giving an average monolayer thickness of 2.38 (± 0.16) nm. The results are shown in figure 5.14. The n and k values for the X:1 films were found to be 2.66 and 1.51, respectively. There was a decrease in n and an increase in the k value for the 8:1 film, this is possibly a result of problems with dipping during LB deposition.

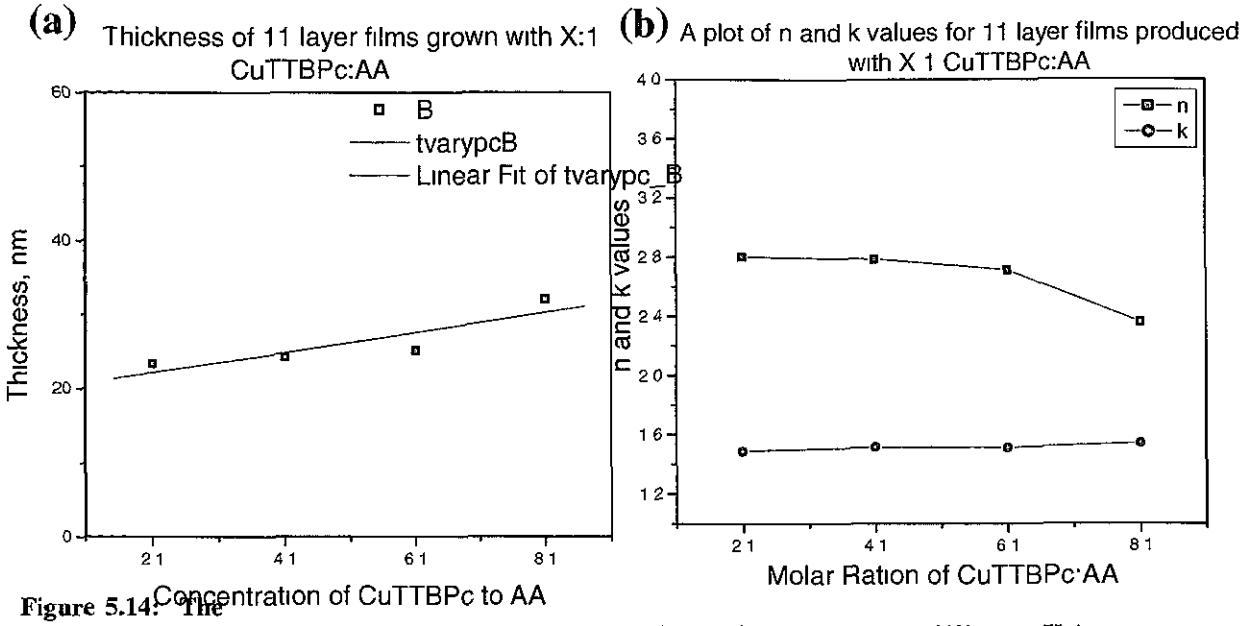

Figure 5.14: The thicknesses (a) and n and k values (b) of the 11 layer films grown at different X:1 CuTTBPc:AAconcentrations.

A summary of the results for the 1:1 CuTTBPc:AA, 1:X CuTTBPc:AA and X:1 CuTTBPc:AA is shown in table 5.2.

Ratio of CuTTBPc:AA	MLThickness,nm	n	k
1 1	2.19 (±0 70)	2.21	1 57
1:X	2.35 (±0 14)	2.84	1.52
X:1	2.38 (±0 16)	2.66	1.51
Overall Averages	2.31	2.57	1.53

Table 5.2: The ellipsometry results 1:1 CuTTBPc:AA, 1:X CuTTBPc:AA and X:1 CuTTBPc:AA LB films.

Manno *et. al.* [9] found that the refractive index of Cu(dmdc)Pc varies from 1.3 to 2 5 across a spectral range of 300-800 nm. At 633 nm Nabok *et. al.* [11] found the refractive index of $AmPc_6$ (bishydroxybutyl hexaalkyl phthalocyanine, where the alkyl group is C_6H_{13}) to be 1.4 and the extinction co-efficient to be 0.146. They found the refractive index of $AmPc_8$ (bishydroxybutyl hexaalkyl phthalocyanine, where the alkyl group is C_8H_{17}) to be 1.5 and the extinction co-efficient to be 0 272. The LB films of $AmPc_6$ and $AmPc_8$ had an average monolayer thickness of 2 nm and 2.4 nm respectively. The average values for the refractive index and extinction co-efficient of CuTTBPc:AA, in this work, were found to 2.57 and 1.53,

respectively, at 620 nm. These values were calculated for films 11 MLs or more in thickness with the overall ML thickness working out at 2.31 nm.

5.3 STM study of evaporated CuTTBPc films

While numerous papers have been published on the STM and STS studies of CuPc on surfaces [12]-[18] very little has been published regarding CuTTBPc. In this experiment the STM technique was used to study the orientation of individual CuTTBPc molecules on two different surfaces, Si(111)-(7x7) and the silver passivated Si(111) surface, Ag/Si(111)-($\sqrt{3}$x$\sqrt{3}$). Scanning Tunnelling Spectroscopy (STS) studies were also undertaken to measure the position of the HOMO and LUMO states of the CuTTBPc on the silver terminated silicon surface.

5.3.1 The Si(111)-(7x7) Surface

The structure of Si (111) – (7x7) was studied in detail by Takayanagi *et. al.* [19] using transmission electron diffraction (TED), which enabled them to determine the atomic arrangement in the unit cell of a reconstructed surface layer. Using the ***Dimer Adatom Stacking (DAS)*** fault model they explained the reconstruction of Si (111)-(7x7). The surface consists of dimer bonds, adatoms, rest atoms and subsurface stacking faults as can be seen in figure 5.15. The left hand side of the top view represent stacking on the faulted side while the right hand side represents stacking on the unfaulted side.

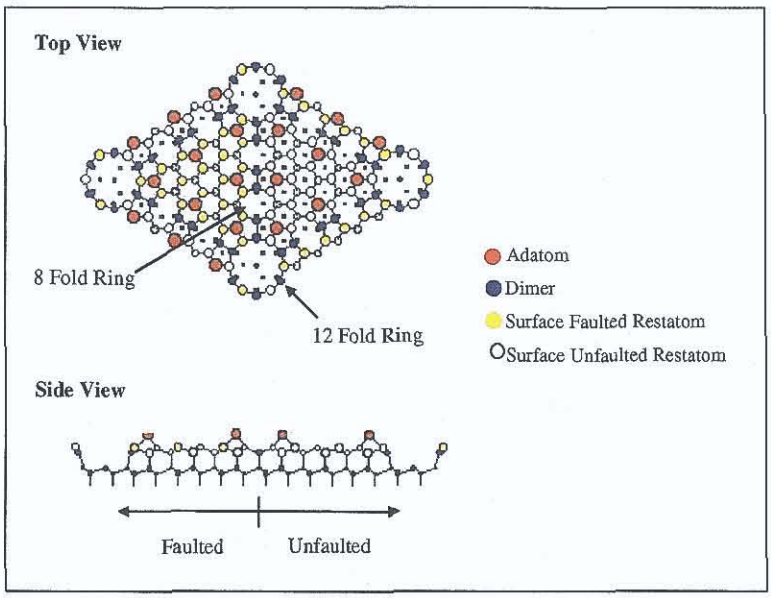

Figure 5.15: The DAS model for the Si(111)-(7x7) with the stacking fault on the left hand side of the image [20].

The Si(111)-(7×7) surface was prepared by repeated cycles of flashing to a temperature of ~1,200°C. This removed the native oxide from the Si(111) surface. The final flashing cycle was followed by a rapid cooling to 950°C and then a slow cooling at a rate of 100°C/minute to room temperature. Figure 5.16 shows filled and empty state STM images of the atomically clean Si(111)-(7×7) surface.

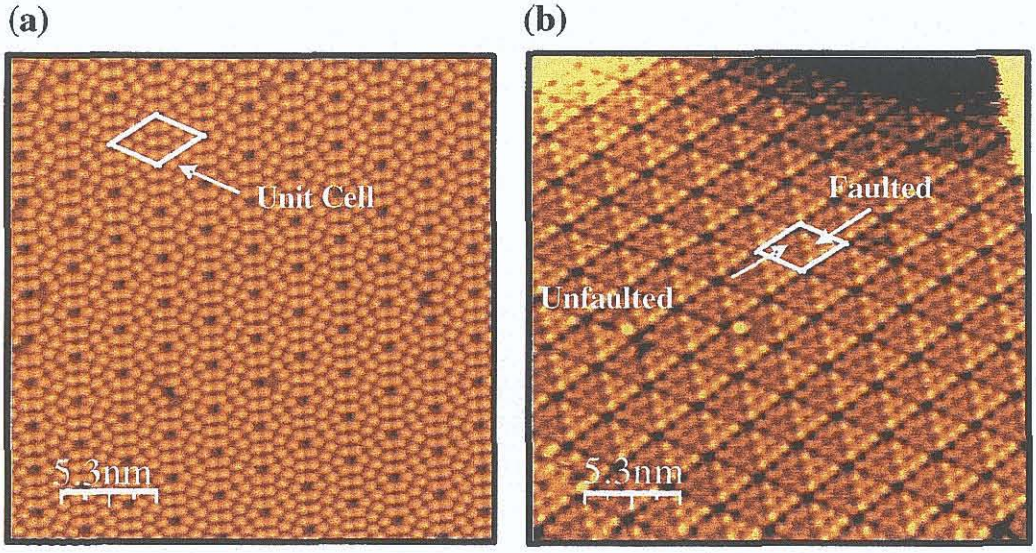

Figure 5.16: (a) Filled and (b) empty states of the (7x7) reconstruction where the tunnelling current in (a) was 1.0 nA and the bias was 1V and in (b) the tunnelling current was 0.5 nA and the bias was -1V. The scan size was 26.6 nm^2 in both cases.

5.3.2 The Ag/Si(111)-(√3 x √3) Surface

The deposition of Ag onto Si (111) – (7x7) held at a temperature of ~700K lead to the formation of a (√3x√3)- R30° reconstruction [21][22][23] which will be referred to as Ag/Si-√3 from now on. The resulting structure is known as the ***Honeycomb-Chain-Trimer (HCT)*** model [21][22][23]. A typical empty state STM image, shown in figure 5.17 reveals a hexagonal structure consisting of six protrusions, which make up the honeycomb structure. The honeycombs relate to the charge density at the centre of the Ag trimers and the dark regions relate to the underlying silicon trimers. The unit cell has a length of 0.648±0.002 nm.

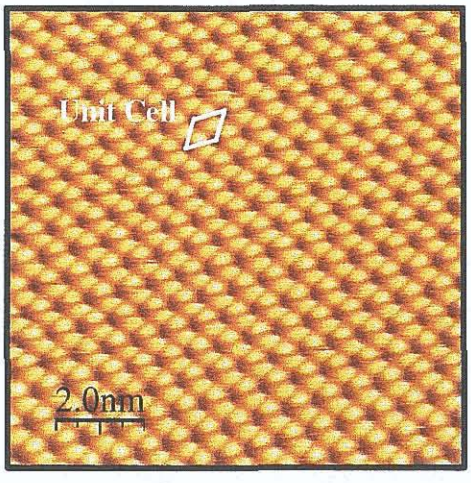

Figure 5.17 : A 10nm^2 STM image of Ag/Si(111)- (√3 x √3) R30°, taken at a tunnelling current of 0.75 nA and a voltage of 1.5 V.

5.3.3 An STM Study of CuTTBPc on Ag/Si(111)-√3

STM and STS can provide information regarding the bonding between the molecule and the substrate, charge distribution and the geometric configuration of the molecule. At 600k a monolayer of CuTTBPc was evaporated onto the Ag/Si (111)-√3 surface at a rate of 0.2ML per minute from a tantalum crucible in a homemade deposition cell. The total pressure during phthalocyanine deposition was in the 10^{-9} mbar range. Before evaporation the phthalocyanine powder was degassed for about 12 h to remove water vapour. CuTTBPc deposited on the surface forming rows of molecules as can be seen clearly in figure 5.18. The rows were made up of groups of two molecules aligned together to give a dimer structure. The dimers had a

very organised structure and they grew in lines parallel to each other. The STM images showed that CuTTBPc formed a highly ordered and tightly packed molecular arrays on the surface. Figure 5.18 shows two STM images, one taken with a positive sample bias (a) and one taken with a negative sample (b). In image (a) the tetra-tert-butyl (TTB) groups could be seen as bright dots, where each TTB group contributed to the diamond shaped features, while the Pc ring was imaged as the dark region. In image (b) filled states are shown as the bright regions which exhibit the four fold symmetry of the Pc ring. The unit cell is shown in white where the dimensions of the cell are 3.36 nm (± 0.02nm) by 1.86 nm (± 0.01nm) and the ratio of the sides is 1.81, as calculated using the WsXm software package [24].

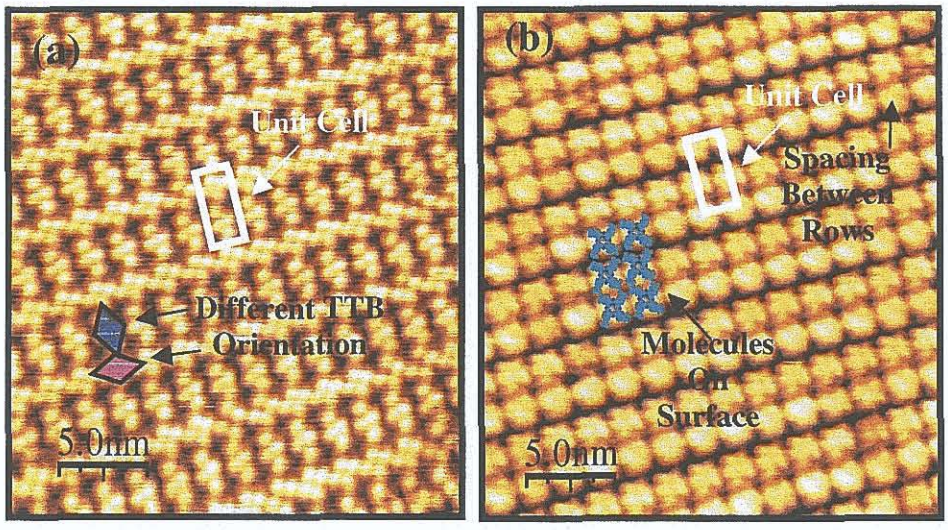

Figure 5.18: The 25x25nm STM images, both taken with a tunnelling current of 1.0nA, showing the (a) empty and (b) the filled states of the CuTTBPc molecule on Ag/Si-√3. (a) was taken with a sample bias of +2.0V while (b) was taken with –2.0V. When imaging the empty states two different orientations of the TTB group can be seen (a). In (b) the alignment of the Pc ring shown.

A proposed structure of the CuTTBPc surface, drawn in ChemSketch [25], is shown in figure 5.19. It was apparent that the TTB groups had two different orientations, in one the spacing between the groups is close together and a second where the spacing is larger. This was a result of a discrete shift in one row of molecules compared to another. The pink diamond represents the region where the shift occurs and where the TTB groups are tightly packed together. The blue diamond represents the TTB groups situated within a row of molecules and they

were spaced further apart than those between the rows. The unit cell is outlined in black. The two grey lines running parallel to each other represent the dark rows observed in the filled state image (b). Intermolecular distances, calculated in ChemSketch [25], the dimensions of the unit cell in figure 5.18 were found to be 3.35 nm by 1.86 nm and gave a ratio of 1.80. This was in good agreement with the WsXm measurement taken for STM images in figure 5.18.

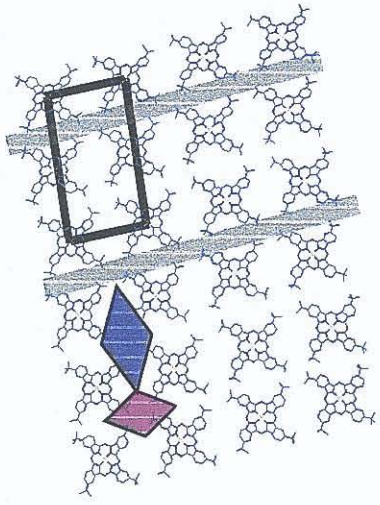

Figure 5.19: The proposed structure of the CuTTBPc surface on Ag/Si (111)-√3. The unit cell is shown in black and the spacing between the rows in grey. The pink and purple diamonds represent the TTB groups between the rows and within the rows, respectively.

Three sets of measurements were taken on both the empty and filled state images. The horizontal distance across four Pc rings (a), the vertical distance up four Pc rings (b) and the diagonal distance across one Pc ring (c). Figure 5.20 shows the empty states STM image (a) and the profile analysis (b) for a (12 x 12) nm^2 scan taken with a sample bias of 2.0V and tunneling current of 0.15 nA.

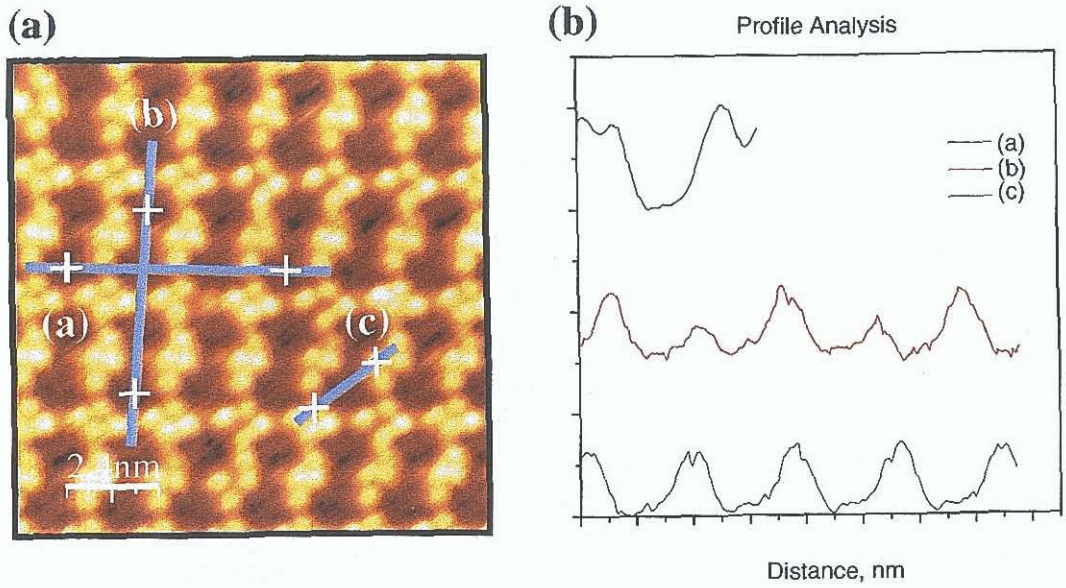

Figure 5.20: (a) STM and (b) profile analysis of a (12x12)nm image with a sample bias of +2.0V and tunneling current of 0.15nA.

Figure 5.21 shows the filled states STM image (a) and the profile analysis (b) for a (12x12)nm^2 scan taken with a sample bias of -1.75V and tunneling current of 0.75 nA.

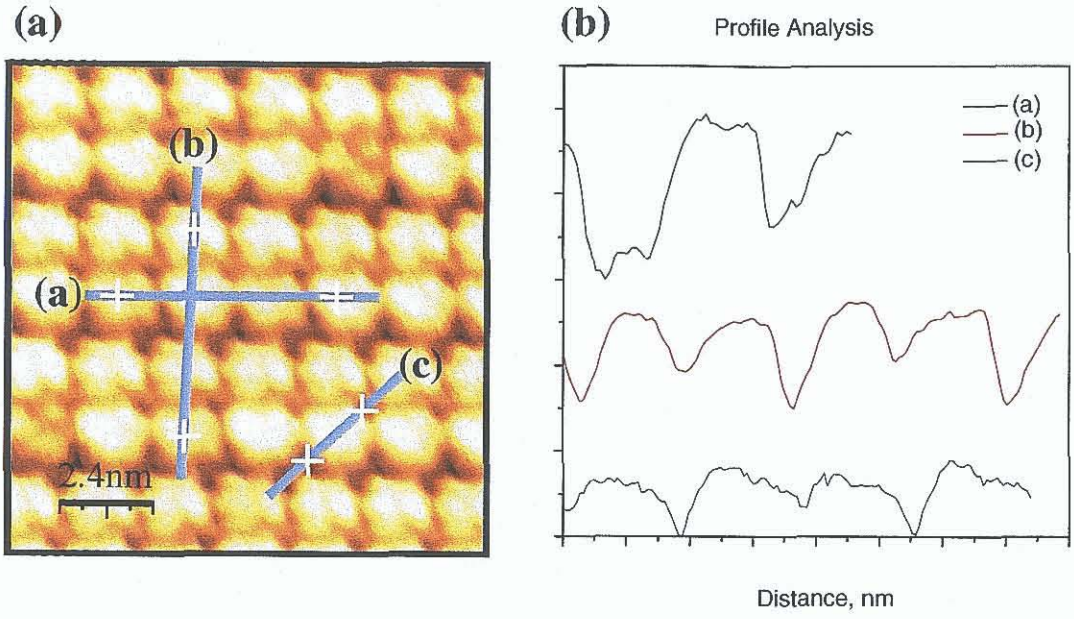

Figure 5.21: (a) STM and (b) profile analysis of a (12x12)nm image with a sample bias of -1.75V and tunneling current of 0.75nA.

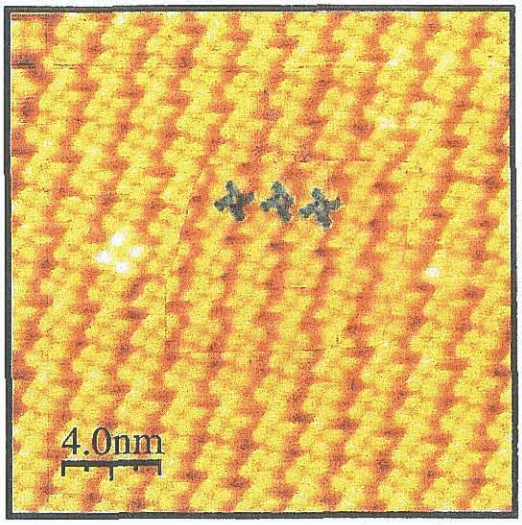

Figure 5.22: A (20x20)nm STM image of the filled states, taken with a sample bias of -2.0V and a tunneling current of 0.25nA. The four fold symmetry of the ring is clearly visible.

When the CuTTBPc surface was imaged on a larger scale, the formation of molecular domains was observed. Figure 5.23 shows a (40x40) nm^2 image. Two domains could be seen at an angle of 102° to each other. It is interesting to note that the rows, for the most part, consisted of two molecules side by side which lead to the formation of dimers on the surface. There were however, rows which were made up of three molecules, or trimers, and in the boundary of the two domains the molecules had a random orientation.

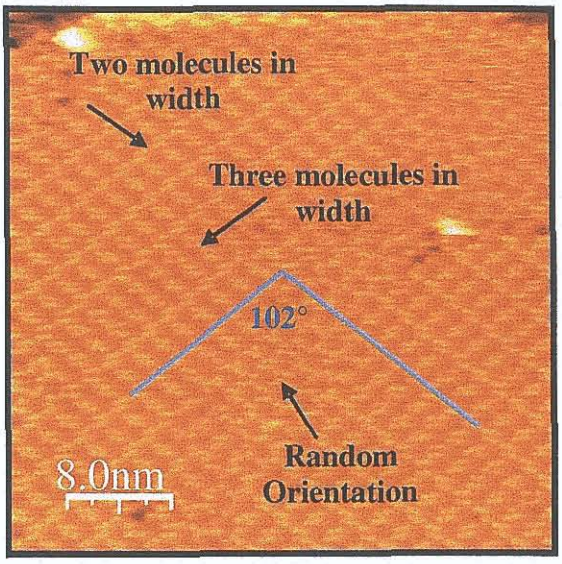

Figure 5.23: Domain formation within the CuTTBPc surface, (40x40)nm scan with a sample bias of +2V and tunneling current of 0.1nA.

5.3.4 An STM Study of CuTTBPc on Si(111)-(7x7)

A low coverage of CuTTBPc was also deposited on the clean Si (111)-(7×7) and imaged by STM, however this proved to be difficult. Lippel *et.al.* [16] deposited CuPc on Cu (100) but encountered difficulties with imaging and surface coverage when working with CuPc on Si (111) and Au (110). Yu Suzuki *et. al.* [17]also found that there was no ordering when they deposited CuPc on Si (111) but when they passivated the surface with hydgrogen the CuPc formed wire like growths on the surface. Nakamura *et. al.* [18] found that the adsorption of CuPc on H-Si (111) was random when the coverage was below one monolayer but that the ordering improved once the coverage exceeded one monolayer. CuPc is found to bond on the silicon surface via two different routes involving the dangling silicon bond. The first route is the stationary route which gives STM images were the four fold symmetry of the CuPc ring can seen, as shown in figure 5.19. The second route involves the interaction of the dangling bond with the phenyl ring of the CuTTBPPc molecule and this gives rise to a circular image of CuPc instead of a four fold image [13]. This is illustrated in figure 5.24.

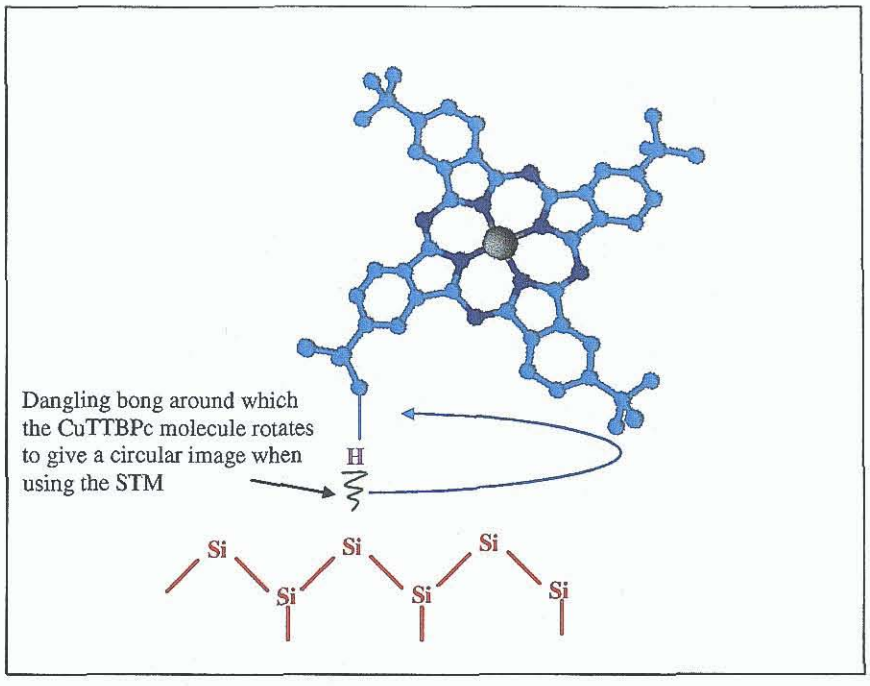

Figure 5.24: The rotation of theCuTTBPc molecule which gives rise to circular images.

Figure 5.25 shows an example of an STM image obtained for CuTTBPc on Si(111). In this image the surface coverage was very low in contrast to the images for CuTTBPc on Ag/Si(111)-$\sqrt{3}$. The diameter of the circular regions was found to be, on average, 4.50 nm ± 0.41 nm. This result was approximately twice the diameter of the CuTTBPc molecule suggesting that the molecule was rotating in a circular path around a dangling bond. Since the surface coverage was poor very few instances of circular images were observed.

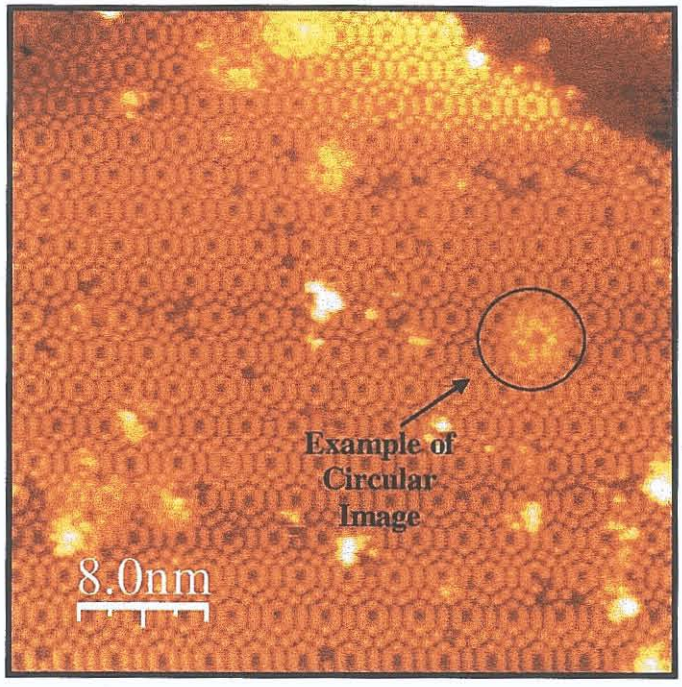

Figure 5.25: 40x40nm STM image of CuTTBPc on Si(111)-(7x7) where circular images of CuTTBPc can be seen. This image was taken with a +1.5V and a tunneling current of 0.5nA.

5.3.5 STS Results for CuTTBPc on Ag/Si-√3

STS spectra were recorded to probe the density of states of 1 ML of CuTTBPc on a Ag/Si-√3 surface. The *I(V)* and *(dI/dV)/(I/V)* spectra shown in figure 5.26, were taken and compared to the XPS and XAS data discussed later in Chapter 6. The *(dI/dV)/(I/V)* spectra are normalised conductivity spectra representing the density of states. Each STS spectra is the result of the averaging of over 2,500 spectra within an image.

Figure 5.26 (b) shows that there is excellent agreement between the spectra This strong reproducibility was observed when scanning other parts of the sample.

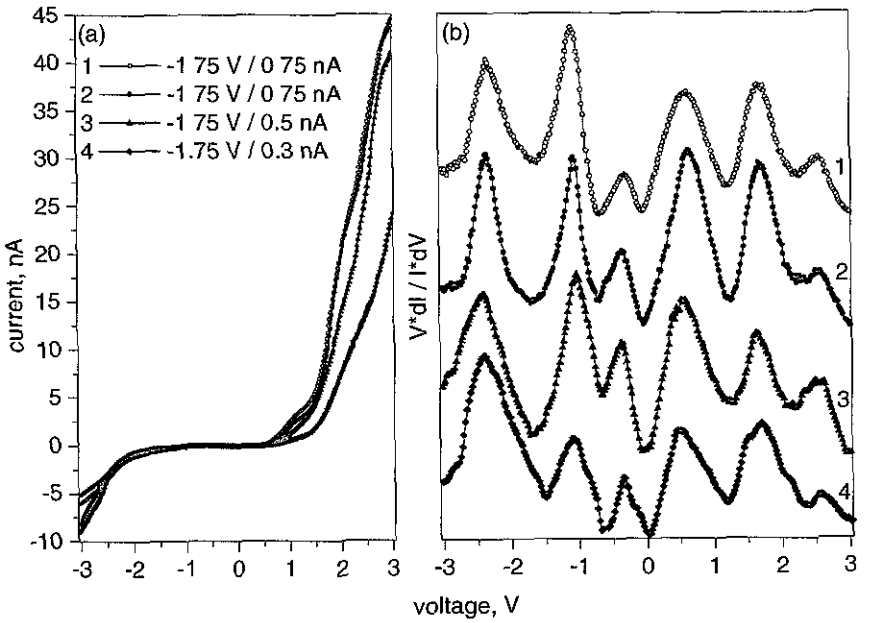

Figure 5.26: The *I(V)* spectra (a) and the corresponding normalised conductivity spectra *(dI/dV)/(I/V)* representing the density of states (b). Spectra 1, 3 and 4 were averaged over 2,500 points in one area of the sample, while spectrum 2 was acquired in a different area of the sample and was averaged over the same number of points.

Six distinct features were observed in the *(dI/dV)/(I/V)* spectra. The peaks at -2.3 V, -1.1 V and -0.4 V corresponded to the occupied states of the molecule while the peaks at 0.7 V, 1.7 V and 2.6 V corresponded to the unoccupied states [26].

Figure 5.27 shows the normalised conductivity spectra for CuTTBPc (1 and 2), clean Ag/Si-$\sqrt{3}$ (3 and 4) and the valence band XPS spectrum for an Ag(100) single crystal. It can be concluded that spectra 1 and 2 are purely a result of the CuTTBPc layer. One peak, at 1.7 V, was present in both CuTTBPc layer and the Ag/Si-$\sqrt{3}$ substrate spectra. In the case of the Ag/Si-$\sqrt{3}$ surface this peak had two additional shoulders, which were absent in the STS spectra of the CuTTBPc layer. This indicated that no spectral features related to a signal from the substate were present in the STS spectra measured from the ordered phthalocyanine layer.

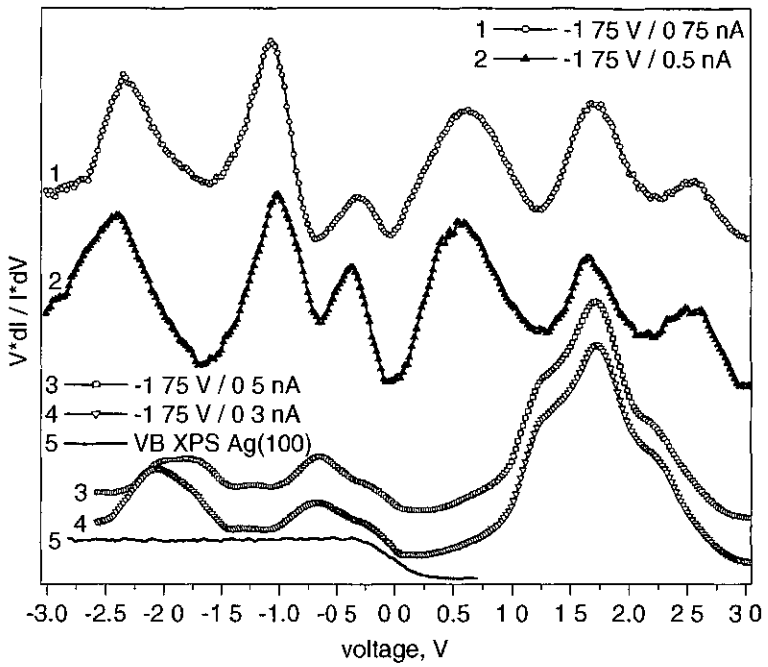

Figure 5.27: Comparison between the normalised conductivity spectra for CuTTBPc (1 and 2) and clean Ag/Si-√3 (3 and 4). The solid line (5) show the valence band XPS spectrum for a Ag(100) single crystal.

Assignment of the peaks in the STS spectra was achieved by comparison of the STS results with that of the XPS and XAS results, figure 5.28. There was a good overall correlation in the results with the energy positions of the carbon and nitrogen peaks found in the XAS spectra agreeing well with those found in the STS spectra.

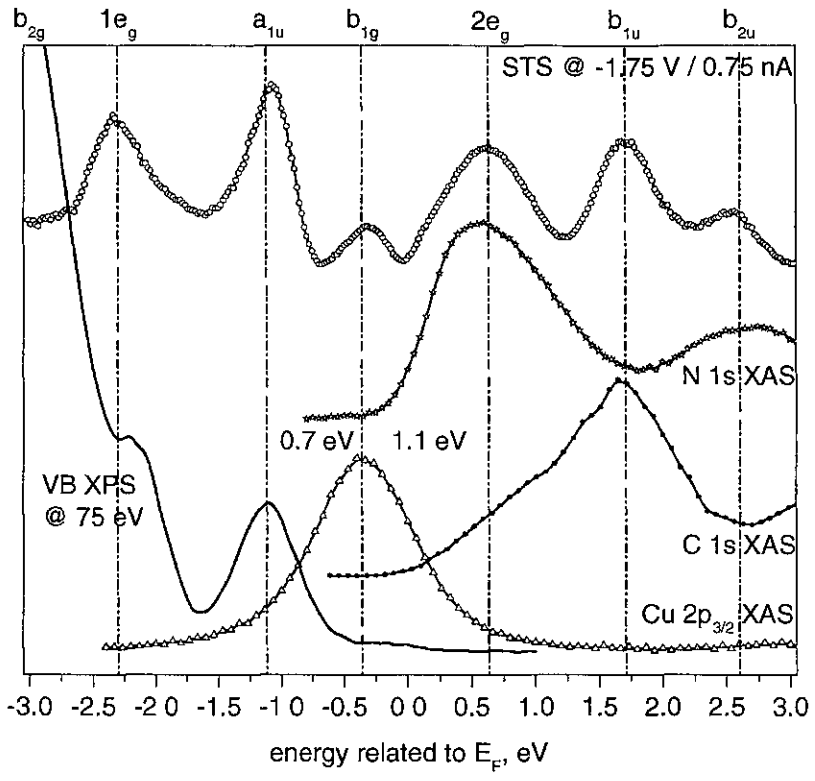

Figure 5.28: Comparison of the normalised conductivity spectrum from the 1 ML CuTTBPc on Ag/Si(111)-√3 to that of the XPS VB spectrum and XAS of CuTTBPc (10-20 ML) prepared in-situ on clean Si(111). The energy scales of the absorption spectra are aligned using the core level energies, E (C 1s) = 284.45 eV, E(N 1s) = 398.5 eV and E(Cu $2p_{3/2}$) = 934.5 eV.

The assignment of the peaks in figure 5.28 was carried out by comparison to theoretical calculations using the density functional theory [27][28]. The peak at -0.4 V was the occupied state of the HOMO having a b_{1g} symmetry. It was a half occupied σ molecular orbital and had characteristics of both Cu $3d(x^2-y^2)$ and ligand 2p [27]. The main peak in the Cu $2p_{3/2}$ XAS spectrum was a result of the dipole-allowed transition of the $2p_{3/2}$ to an empty 3d state. The empty 3d state was associated with the electron configuration of Cu which is missing one 3d electron. The energy position of the Cu $2p_{3/2}$ XAS peak correlated well with the energy of the position of the STS peak at -0.4 eV. This confirmed the HOMO was half occupied and mainly 3d in character.

The peak at -2.3 eV was due to the occupied state of the π molecular orbital having an e_g symmetry and the peak at -1.1 eV was due to an a_{1u} symmetry. The a_{1u} π molecular orbital consists mostly of C 2p states [27][29] which had both e_g and a_{1u}

symmetry. The peaks found at 0.7 V, 1.7 V and 2.6 V were the molecular orbitals with symmetries of e_g, b_{1u} and b_{2u} respectively. The lowest unoccupied molecular (LUMO) peak was the $2e_g$ π-molecular orbital. Comparing the STS and XAS showed that the $2e_g$ and b_{2u} molecular orbitals had a mixed ligand 2p character. The b_{1u} molecular orbital consisted mainly of empty C 2p states.

Using a complete density of states picture from the STS, VB XPS and XAS data analysis, the band gap of CuTTBPc, a_{1u} (π) $\rightarrow$ $2e_g$ (π^*), was found to be 1.8 eV in this research. This was in good agreement with that of CuPc, a_{1u} (π) $\rightarrow$ e_g (π^*), which was reported to be 1.7-1 75 eV [30][31] [32]. The HOMO-LUMO ($b_{1g} \rightarrow 2e_g$) gap of 1.1eV corresponded to the transport band gap in CuTTBPc. This value agreed with the z(V) spectroscopy results for CuPc using STM [33] and density of functional theory calculations [27][28]. Two discrete occupied states (a_{1u} and b_{1g}) separated by 0.8 eV and located near the Fermi level were observed during X-ray emission measurements performed on 200 nm thick CuPc films prepared on the P Si(100) substrate [34][35]. In these experiments the energy position of the a_{1u} peak was found to agree well with UPS data known in literature [36]-[43] which, in turn, had excellent agreement with STS and VB XPS spectra obtained in this work. The peak related to the b_{1g} MO was hardly visible in CuPc UPS and the VB XPS spectra reported in literature. This could be connected to an ionization character of these spectroscopic techniques leading to strong final state effects, which could modify the binding energy of the b_{1g} state. In this case a photoemission from the a_{1u} and b_{1g} states could overlap in energy resulting in a broad asymmetric feature, which could be correctly observed using high-resolution measurements only [39]. In the case of STS there was no final state effect influence, since the kinetic energy of the outgoing (or incoming) electrons recorded in photoemission experiments was irrelevant for this type of measurements. Only the total number of such electrons was important resulting in the amplitude of a tunnelling current.

5.4 Conclusions

Aggregation within the monolayer of pure CuTTBPc was expected following the analysis of the LB isotherms. In agreement with this the AFM images for the 11 layer pure CuTTBPc film showed that clusters of CuTTBPc were present. A range of films with varying thickness were studied using a 1:1 molar ratio of CuTTBPc:AA. In the 1 layer sample the height of the film was approximately 1.7 nm which coincides with the height of the pure CuTTBPc molecule. The surface of such a film does, however, exhibit some characteristics of the AA monolayer. As the thickness of the film increased the topography exhibited both smooth domains of AA and clusters of CuTTBPc. At higher coverage the surface lost it AA appearance and took on a CuTTBPc appearance, as can be seen in the 19 and 21 layer samples.

Films with a thickness of 11 layers were grown using different concentrations of CuTTBPc:AA. The molar ratio of CuTTPc:AA was varied in the range of 1:2 to 1·10. It was found that the topography of such films tended to become more like the AA monolayer as the concentration of AA increased. Likewise 11 layer films were produced where the amount of CuTTBPc was varied in the molar ratios of 2:1 to 8.1. It was found that films took on a CuTTBPc topography as the amount of CuTTBPc was increased. RMS roughness analysis confirmed these results, as shown in table 5.1

Ellipsometry results indicated that the 1-21 ML films of 1:1 CuTTBPc.AA deposited in a uniform fashion. From figure 5.11 it is reasonable to suggest that there was layer by layer growth, regardless of the aggregation associated with the CuTTBPc molecule. This has been observed by others researchers who have synthesised LB films containing derivates of CuPc [1][10]. The AFM image of the 1 layer sample looked relatively smooth but the images of the thicker films showed clear evidence of clusters. The films consisted of a smooth first layer and subsequent layers of clusters making them Stranski-Krastanov type. When studying the n and k values it became apparent that thick films were needed to accurately determine these optical constant. Films should be 11 layers or more in thickness. The 11 layer films produced with 1:X and X:1 of CuTTBPc:AA did not show any dependency on the molar ratio of the solution used to synthesis the films. Table 5.2 shows that the

overall results were in good agreement with each other with the average monolayer thickness being 2.31 ± 0.14 nm, which agrees well with the thickness of 2.65 nm for the floating ML. Analysis of the AFM height profile gave a ML thickness of 1.70 (±0.04) nm, which had been found for films of CuPc, but with the AFM the heights were not averaged across the sample as they were in ellipsometer. Hence the thickness of an aggregated film would be calculated more accurately using the averaging process in ellipsometry compared to line profile analysis in AFM.

The STM images of evaporated CuTTBPc on Ag/Si(111) showed a highly ordered surface with tighly packed molecular arrays. Such high quality images and reports of such high surface coverage have not been found in the literature to date. It was possible to image the empty and filled states of the CuTTBPc molecule by altering the voltage bias therefore making it possible to image the TTB groups or the phthalocyanine ring. The unit cells dimensions were found to be 3.36 (± 0.02) nm and 1.86 (± 0.01) nm. WsXm and ChemSketch measurements confirmed that the molecule was lying flat on the surface Rows of extremely organised molecules were found running parallel to each other. These rows were 2-3 molecules in width leading to the formation of dimmers and trimer, respectively. When imaging on a larger scale the formation of domains was apparent. Imagining of CuTTBPc on Si (111) proved to be difficult with low surface coverage. Imaging this type of surface revealed the presence of circular images caused by the CuTTBPc molecule rotating around a dangling bonding which formed between the phenyl group of the CUTTBPc and the silicon surface

STS data for CuTTBPc on Ag/Si(111)$\sqrt{3}$ was in excellent agreement with XPS and XAS data for thin films (10-20 ML) of evaporated CuTTBPc. The results also agreed well with the X-Ray emission spectroscopy (XES) data, optical band gap measurements and density functional theory calculations. The HOMO in the CuTTBuPc was a half-occupied σ-MO of b_{1g} symmetry with mixed Cu $3d(x^2-y^2)$ and ligand 2p character. The LUMO was a π-MO of e_g symmetry with mainly ligand (C and N) 2p character. A HOMO-LUMO ($b_{1g} \rightarrow 2e_g$) gap of 1.1eV corresponded to a transport band gap in CuTTBPc.

In general it can be said that the ellipsometry data for LB films of CuTTBPc:AA demonstrated layer-by-layer growth despite strong evidence of aggregation as seen by the AFM. STM images of evaporated CuTTBPc on Ag/Si(111) showed a highly organised surface. In chapter 6 NEXAFS and XPS will be employed to probe this ordering in a more detailed manner with NEXAFS being used to calculate the exact molecular orientation of CuTTBPc in a pure 12 ML LB film and XPS being used to investigate molecular ordering in evaporated films of CuTTBPc and H_2TTBPc on SiO_2 and Si(111)

Chapter Five References

[1] Y-L Lee, Y-C Chen, C H Chang, Y-M Yang, J-R Maa, ***Thin Solid Films***, 370 (2000) 278-284.

[2] I. L. Emelianov, V. V. Khatko, ***Thin Solid Films***, 354 (1999) 237-244.

[3] Yu. L. Emelyanov, V. V. Khatko, A. A. Tomchenko, ***Synthetic Metals***, 79 (1996) 173-175.

[4] C-Q Li, T Manaka, X-Cheng, M Iwamoto, ***Japanese Journal of Applied Physics***, 42 (2003) 2516-2522.

[5] I. L. Emelianov, V. Khatko and A Tomchenko, ***Sensors and Actuators B***, 47 (1998) 158–163.

[6] O.D. Gordan, M. Friedrich, D.R.T. Zahn, ***Organic Electronics***, 5 (2004) 291–297.

[7] A.B. Djurisica, C.Y. Kwonga, T.W. Laua, W.L. Guoa, E.H. Lia, Z.T. Liub, H.S. Kwokb, L.S.M. Lamc, W.K. Chanc, ***Optics Communications***, 205 (2002) 155–162

[8] Y. Wu, D. Gu, F. Gan, ***Optical Materials***, 24 (2003) 477–482.

[9] D. Manno, R. Rella, L. Troisi, L. Valli, ***Thin Solid Films***, 280 (1996) 249-255.

[10] R. Rella, P. Siciliano, L. Valli, K. Spaeth, G. Gauglitz, ***Sensors and Actuators B***, 48 (1998) 328–332.

[11] A. V. Nabok, A. K. Ray, A. K. Hassan, J. R. Travis, ***Supramolecular Science***, 4 (1997) 407.

[12] M.D. Upward, P.H. Beton, P. Moriarty, ***Surface Science***, 441 (1999) 21–25.

[13] L. Liu , J. Yu , N. O.L. Viernes , J. S. Moore, J. W. Lyding, ***Surface Science***, 516 (2002) 118–126.

[14] M. Kanai, T. Kawai, K. Motai, X. D. Wang, T. Hashizhme, T. Sakura,, ***Suface Science***, 329 (1995) L619-L623.

[15] R. Hiesgen, M. Räbisch, H. Böttcher, D. Meissner, ***Solar Energy Materials & Solar Cells***, 61 (2000) 73-85.

[16] P. H. Lippel, R. J. Wilson, M/ D. Miller, Ch. Woll, S. Chiang, ***Phys. Rev. Letters***, 62 (2), 1989, 171-174.

[17] Y. Suzuki , M. Hietschold, D.R.T. Zahn, ***Applied Surface Science***, 252 (2006) 5449–5452.

[18] M. Nakamura, Y. Morita, H. Tokumoto, ***Applied Surface Science,*** 113/l 14 (1997) 316-321.

[19] K. Takayanagi, Y. Tanishiro, M. Takahashi, ***Journal of Vacuum Science & Technology A***, 3, (1986), 1502.

[20] www.ohdomari.com.

[21] R.J. Wilson, S. Chiang, ***Physical Review Letters***, 58 (4), (1987), 369

[22] E. J. Van Loenen, J. E. Demuth, R. M. Tromp, J. R. Hamers, ***Physical Review Letters***, 58(4), (1987), 373.

[23] J. F. Fia, R. G. Zhoa, W. S. Yang, ***Physical Review B***, 48, (1993) 18109.

[24] Scanning Probe Microscopy Software, WsXm 4, Develop 7.6, Nanotec Electronica SL., 2005.

[25] ACD/ChemSktech Freeware, Product Version 10, www.acdlabs.com

[26] S. A. Krashnikov, C. J. Hanson, A. A. Cafolla, ***Journal of Physics Condensed Matter***,

[27] M. S Liao and S. Scheiner, ***Journal of Chemical Physics***, 114 (2001) 9780.

[28] A. Rosa, E. J. Baerends, ***Inorganic Chemistry***, 33 (1994) 584.

[29] E. Z. Kurmaev, S. N. Shamin, V. R. Galakhov, A. Moewes, T. Otsuka, S. Koizume, K. Endo, H. E. Katz, M. Bach, M. Newmann, D. L. Ederer, M. Iwami, ***Physical Review B***, 64 (2001) 045211.

[30] E. A Lucia, F. D. Verderame, ***Journal of Chemical Physics***, 48 (1968)2674.

[31] B H. Schechtman, W. E. Spicer, ***Journal of Molecular Spectroscopy***, 33 (1970) 28.

[32] H. Yoshida, Y. Tokura, T. Koda, ***Chemical Physics Letters***, 109 (1986) 375.

[33] S. F. Alvarado, L. Rossi, P. Müller, W. Rieβ, ***Synthetic Metals***, 122 (2001) 73.

[34] J E. Downes, C. McGuiness, P. A. Glans, T. Learmonth, D. Fu, P. Sheridan, K. E. Smith, ***Chemical Physics Letters***, 390 (2004) 203.

[35] Y. Zhang, J. E. Downes, S. Wang, T. Learmonth, L. Plucinski, A. Y. Matsuura, C. McGuiness, P. A. Glans, S. Bernardis, C. O'Donnell, K. E. Smith, ***Thin Solid Films***, 515 (2006) 394.

[36] T. S. Ellis, K. T. Park, S. L. Hulbert, M. D. Ulrich, J. E. Rowe, ***Journal of Applied Phyics***, 94 (2004) 982.

[37] M. Gorgoi, D. R. T. Zahn, ***Applied Surface Science***, 252 (2006) 5453.

[38] I. G. Hill, A. Kahn, Z. G. Soos, Jr R. A. Pascal, ***Chemical Physics Letters***, 327 (2000) 181 2000.

[39] S. Kera, H. Yamane, I. Sakuragi, K. K. Okudaira, N. Ueno, ***Chemical Physics Letters***, 364 (2002) 93.

[40] T. Schwieger, H. Peisert, M. S. Golden, M Knupfer, J. Fink, ***Physical Review B,*** 66 (2002) 155207.

[41] H. Peisert, M. Knupfer, T. Schwieger, J. M. Auerhammer, M. S. Golden, J. Fink, ***Journal of Applied Physics***, 91 (2002) 4872.

[42] H. Peisert, M. Knupfer, J. Fink, ***Surface Science***, 515 (2002) 491.

[43] T. Chassé, C. I. Wu, I. G. Hill, A. Kahn, ***Journal of Applied Physics***, 85 (1999) 6589.

Chapter 6

A NEXAFS and XPS Study of CuTTBPc and H_2TTBPc in LB and Evaporated Films

Chapter 6 discusses the NEXAFS and XPS results. Using the NEXAFS technique a decrease in the HOMO peak as a function of angle of incoming radiation showed that the molecule had a strong angular dependency and hence must be highly ordered on the surface. It was possible to calculate the exact tilt angle of CutTTBPc in a 12 ML LB film on SiO_2. Analysis of the XPS would verify the NEXAFS results and confirm that there was a definite ordering of the CuTTBPc molecule, not only in the LB film but also in the evaporated films. The XPS results disclosed how the substrate and method of film deposition can influence the orientation of the molecule.

6.1 Introduction

LB films should, by nature, posses a well defined structure. The capability of the NEXAFS technique to determine molecular orientation is now widely accepted [1]. In section 2.6.3 it was outlined how this technique can be used to determine the tilt angle of a molecule on a surface. A systematic study of the orientation of the CuTTBPc molecules in an LB film was performed by investigating variations in the C 1s and N 1s NEXAFS spectra as a function of the incident angle of the synchrotron radiation and from this the tilt angle of the CuTTBPc molecule in the LB film was deduced.

The results of the NEXAFS experiment were compared to those of XPS experiments. XPS was implemented to investigate the orientation of CuTTBPc in vacuum deposited films (on SiO_2 and Si(111) substrates) and an LB film deposited on SiO_2. Additional electronic information regarding copper was obtained by comparing the valence band spectra of the CuTTBPc and H_2TTBPc films.

6.2 Data Analysis

6.2.1 NEXAFS Data Processing

The raw data was processed using a programme written in Matlab code [2]. The NEXAFS signal was first normalised to the number scans and the average flux in photon beam which is proportional to the electron current in the storage ring. A further background correction was made for absorption by carbon and nitrogen containing molecules deposited on the beamline optics. This was done by measuring C 1s and N1s spectra from a clean (carbon and nitrogen free) tantalum sample holder, figures 6.1 (a) and (b).

The normalised NEXAFS signal was then divided by the corresponding background signal. Finally, a background signal was fitted and removed from the spectrum such that the high photon energy region of each spectrum is normalised to unity.

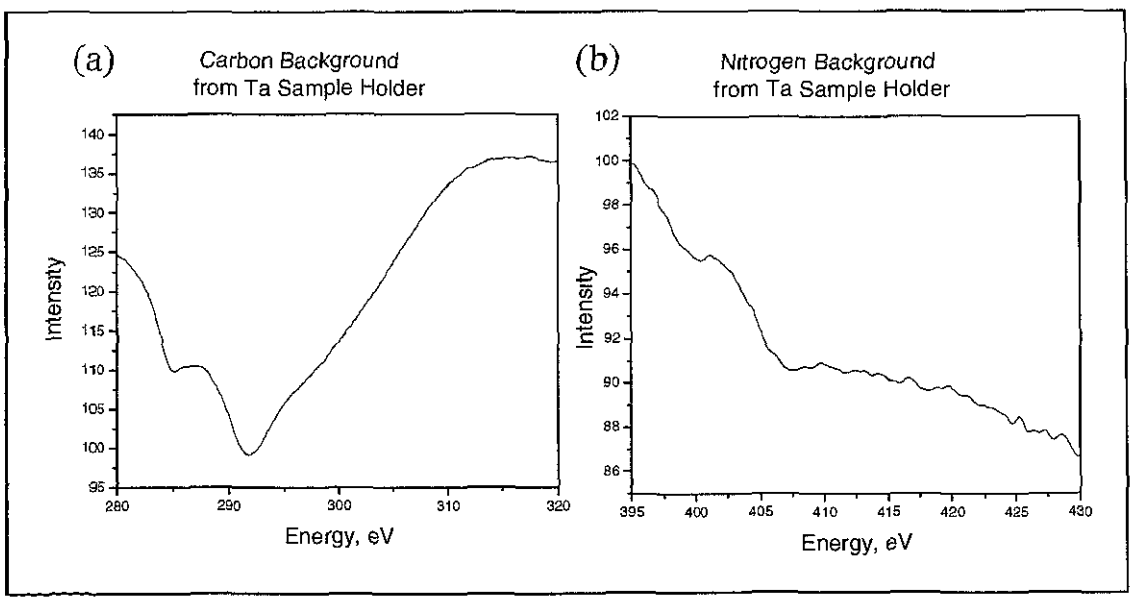

Figure 6.1: The carbon 1s (a) and nitrogen 1s (b) backgrounds obtained from the clean tantalum sample holder.

6.2.2 XPS Data Processing

XPS valence band spectra were recorded at different emission angles. An example of a spectrum for H_2TTBPc is shown in figure 6.2. These data were then normalised as follows. Firstly the raw data was divided by the number of scans and the average flux in photon beam. A constant background level was calculated by averaging the signal at the high kinetic energy end of each spectrum. This average background was subtracted from the raw data. The maximum intensity of the butyl peak was found and the spectrum was normalised to this value. Gaussian fits were applied to the HOMO peaks to calculate the integrated intensity of these peaks as a function of angle of incidence. The Origin plotting package [3] was sufficient to carry out the normalisation process and the area calculations.

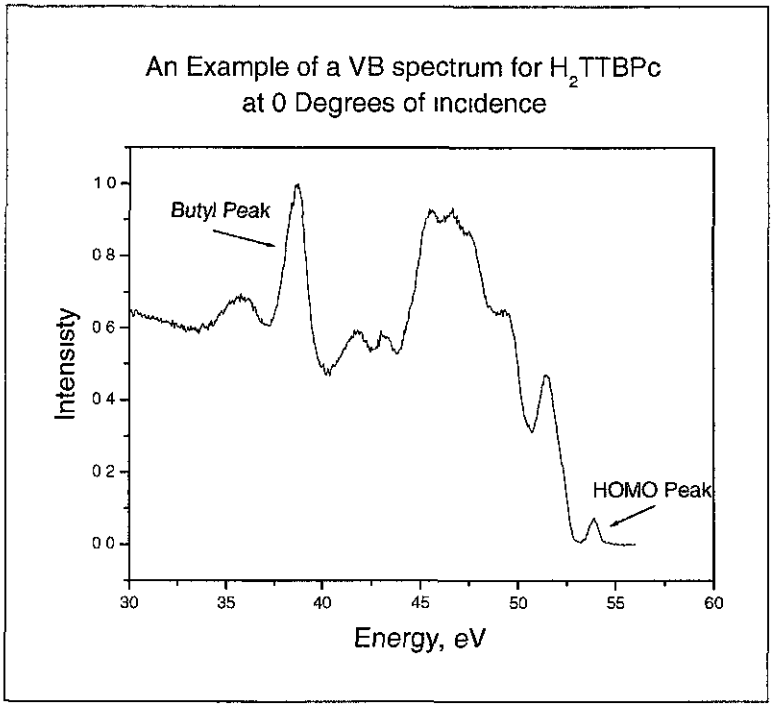

Figure 6.2: An example of a H_2TTBPc spectrum showing the butyl and HOMO peaks.

Both H_2TTBPc and CuTTBPc molecules were studied using the XPS. Since the only difference between these phthalocyanine molecules was the presence of a copper atom it was possible to study the contribution of the copper signal by subtracting the H_2TTBPc from the CuTTBPc spectrum. The subtraction of the normalised CuTTBPc and H_2TTBPc signals was carried out in Origin [3]. The area

under the copper $3d^84s^2$ peaks was calculated using Gaussian fits. An example of the $3d^84s^2$ peaks in the subtracted signal is shown in figure 6.3

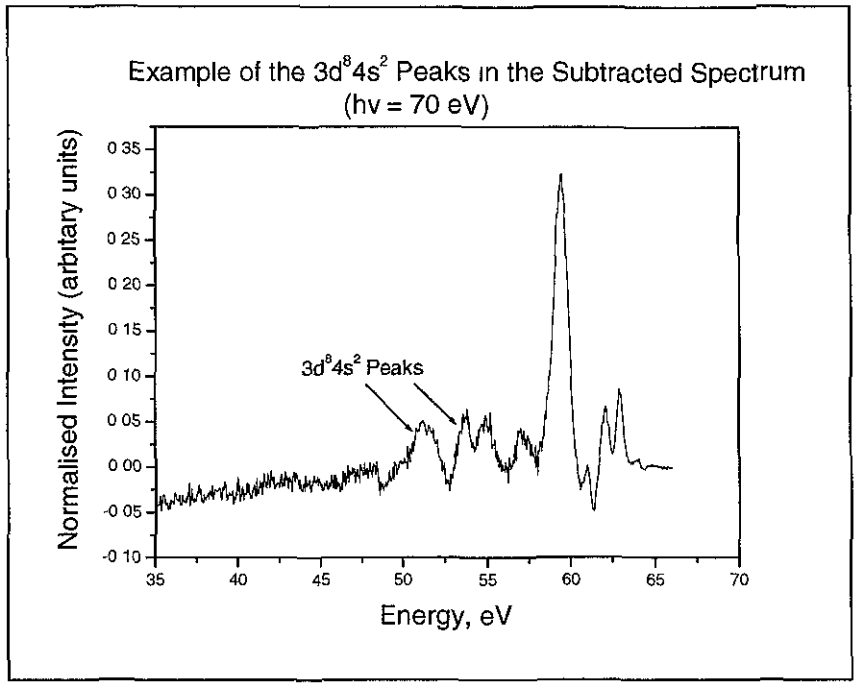

Figure 6.3: An example of the copper $3d^84s^2$ peaks in the subtracted spectra where the H_2TTBPc signal was subtracted from the CuTTBPc signal leaving just the copper signal.

6.3 Interaction of Radiation with Surface Molecules

The absorption of the incoming radiation is influenced by the orientation of the molecules on the surface. If the molecule is lying flat and the radiation is normal to the surface the π^* orbitals lie perpendicular to the surface and to the polarisation vector of the incoming radiation. In this configuration the σ^* orbitals are parallel to the surface and the polarisation vector. At normal incidence ($\theta = 0°$) the polarisation vector is parallel to the plane of the molecule. In this instance the π^* signal will be a minimum and the σ^* signal will be a maximum as shown in figure 6.4.

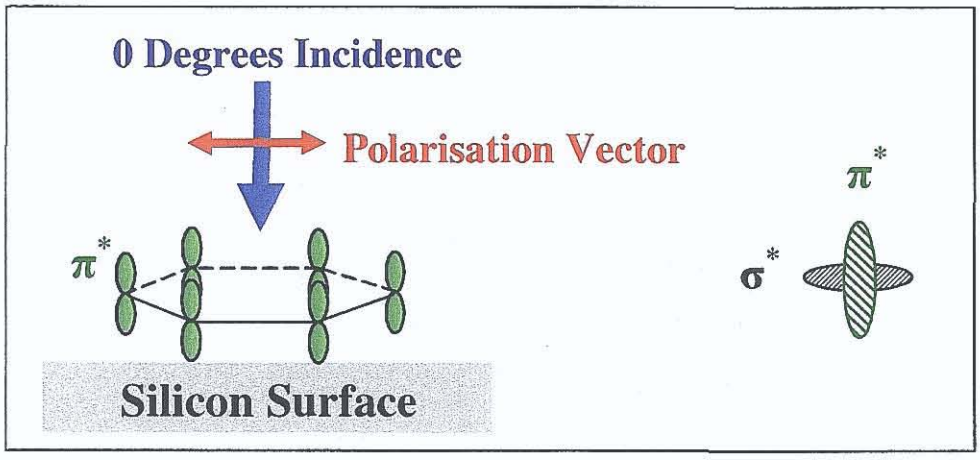

Figure 6.4: The interaction between the incoming radiation and the π^* and σ^* bonds when the molecule is lying flat on the surface.

If the molecule is standing on the surface the π^* orbitals lie parallel to the polarisation vector and there should be a maximum absorption for π^* and a minimum for σ^* in this configuration, figure 6.5.

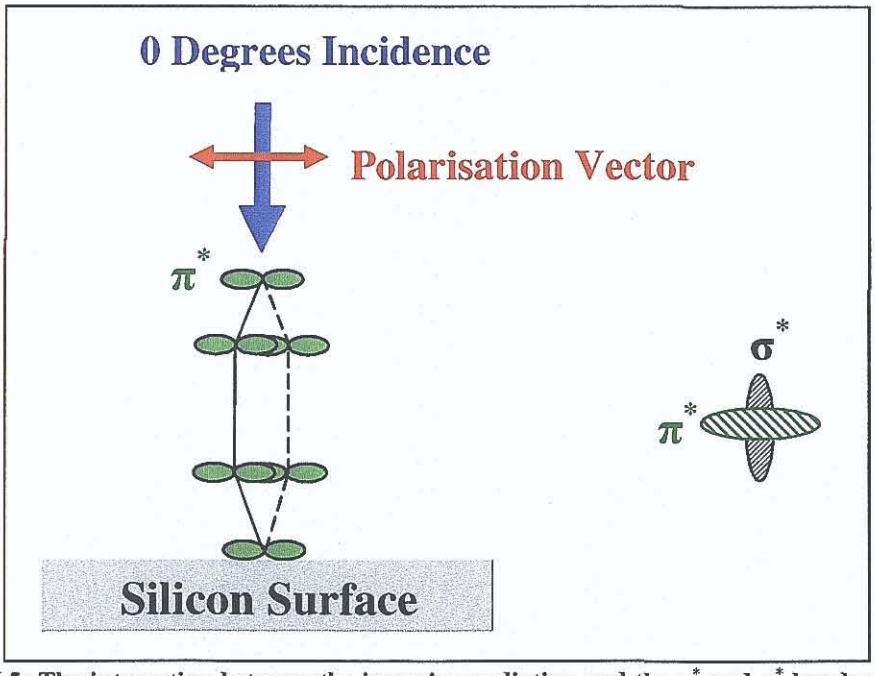

Figure 6.5: The interaction between the incoming radiation and the π^* and σ^* bonds when the molecule is standing on the surface.

6.4 NEXAFS Study – The orientation of CuTTBPc on SiO_2

The experimental conditions under which the pure CuTTBPc LB film was synthesised and the NEXAFS experiment was conducted are given in sections 4.2.1 and 3 6.1 respectively. Papers have been published on angular dependent NEXAFS studies of evaporated phthalocyanine and it derivatives [4 -7] but nothing to date has been reported on the NEXAFS studies of phthalocyanine LB films. Figure 6.6 shows an example of the C 1s spectra for the CuTTBPc LB film in this work. Here two extremes are shown to demonstrate how the intensity of the carbon 1s absorption peak changes when the angle of incidence of incoming photons is altered. The intensity of the π-π* transition drops significantly as the angle is changed from 0° to 80° relative to the normal. Such a strong angular dependence indicates that molecules have a specific molecular orientation on the surface.

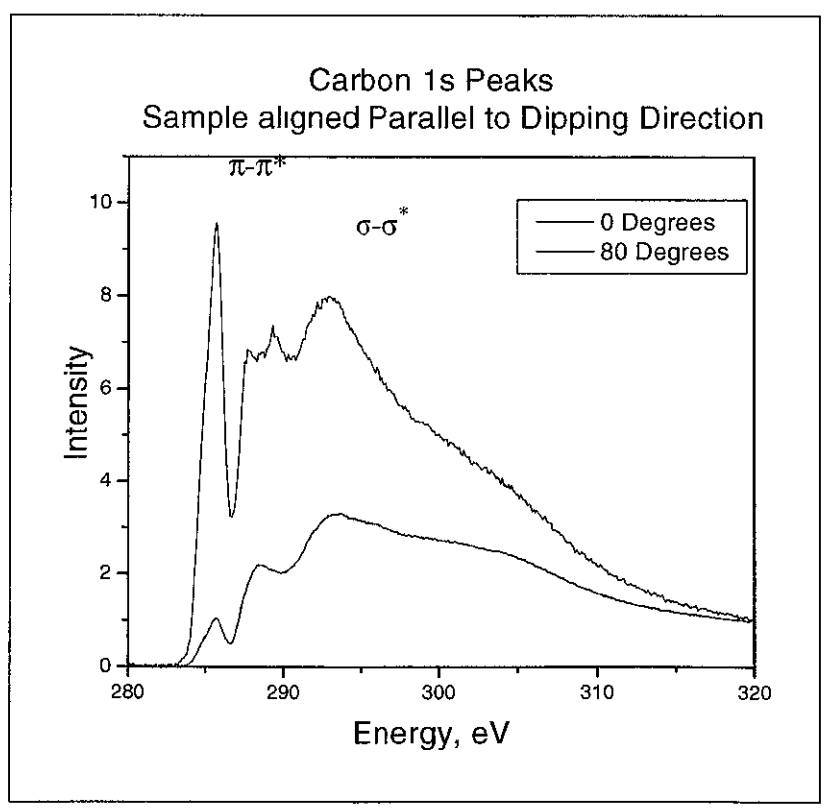

Figure 6.6: NEXAFS spectra recorded at 0 and 80 degrees relative to the normal, note the decrease in the peak intensity when the angle goes from 0 to 80 degrees.

Spectra were recorded at polar angles of 0, 25, 45, 60 and 80 degrees. In addition, for each set of polar angles, the azimuthal angle was varied such that the dipping direction was aligned parallel to, perpendicular to, and at 45° to the polarisation vector of the incident radiation, as shown in figure 6.7.

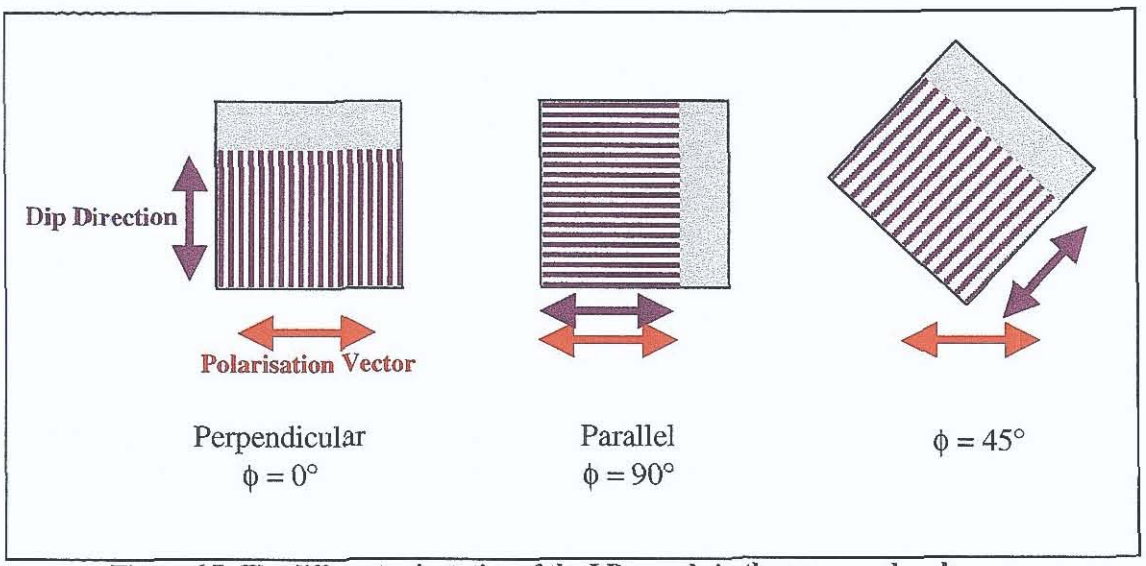

Figure 6.7: The different orientation of the LB sample in the vacuum chamber.

The full set of data for the corrected carbon and nitrogen spectra, taken with the dip direction perpendicular to the polarisation vector, are shown in figure 6.8. For both carbon and nitrogen it can be seen that the intensity of the π-π* peak decreased as the angle of incidence increased, whereas the intensity of the σ-σ* peak increased.

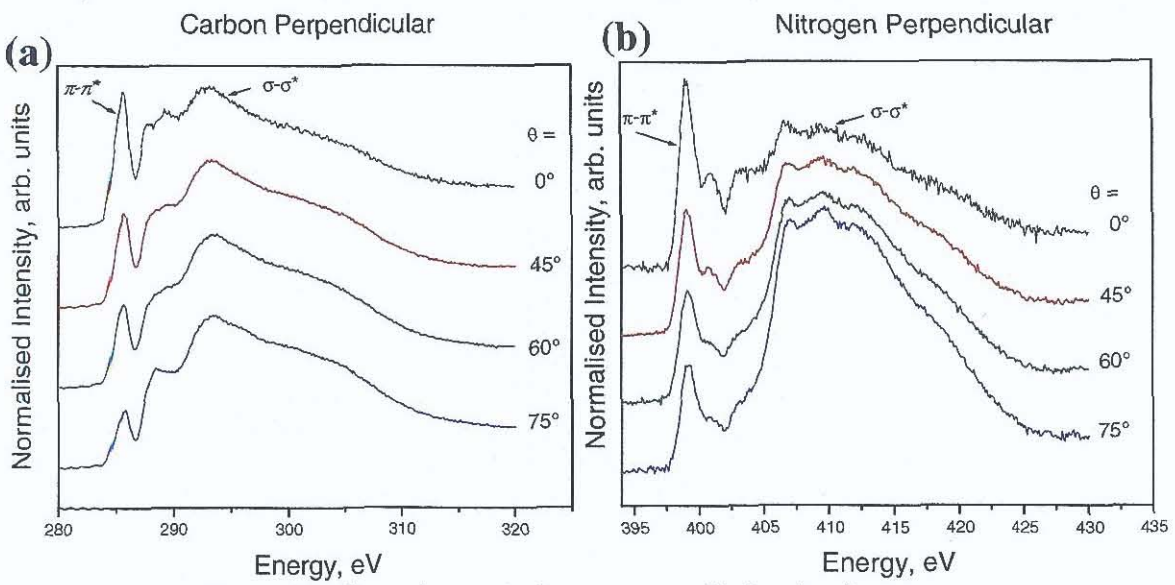

Figure 6.8: The carbon and nitrogen perpendicular signals.

A similar trend was found when the sample was orientated with the dip direction at 90 and 45 degrees the plane of polarisation, as shown in figures 6.9 and 6.10.

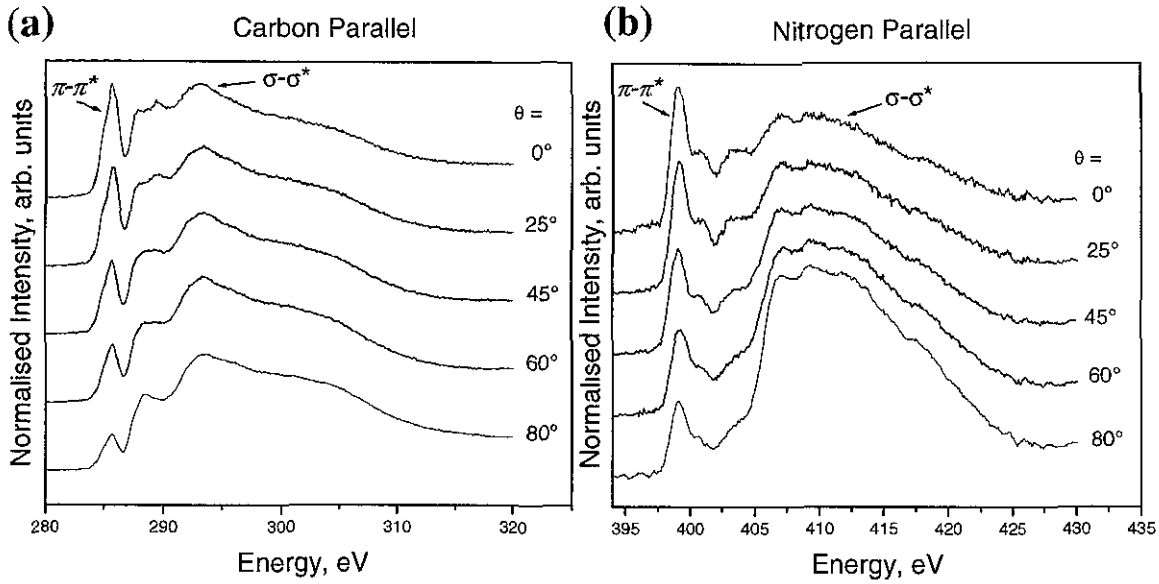

Figure 6.9: The carbon 1s (a) and nitrogen 1s (b) spectra obtained when the sample was sample was orientated parallel to the plane of polarisation

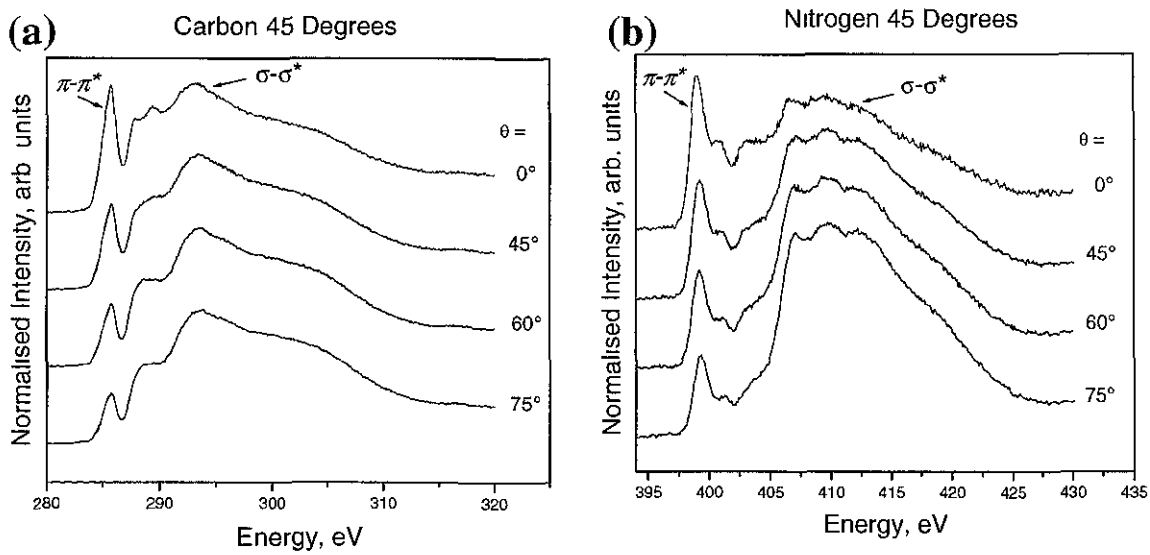

Figure 6.10: The carbon 1s (a) and nitrogen 1s (b) spectra obtained when the sample was orientated at 45° degrees to plane of polarisation.

All three azimuthal orientations showed the π-π^* peak decreasing and the σ-σ^* peak increasing as the angle of incidence increased. From these observations it could be deduced that the molecule was either standing upright, or at a slight tilt angle relative to the surface normal. To confirm this observation the area under the π-π^* peak for C 1s and N 1s was measured for each data set and the relative intensity was plotted as a function of the angle of incidence as shown in figure 6.11. There was no trend in the graphs to suggest that the azimuthal orientation of the sample influenced the results.

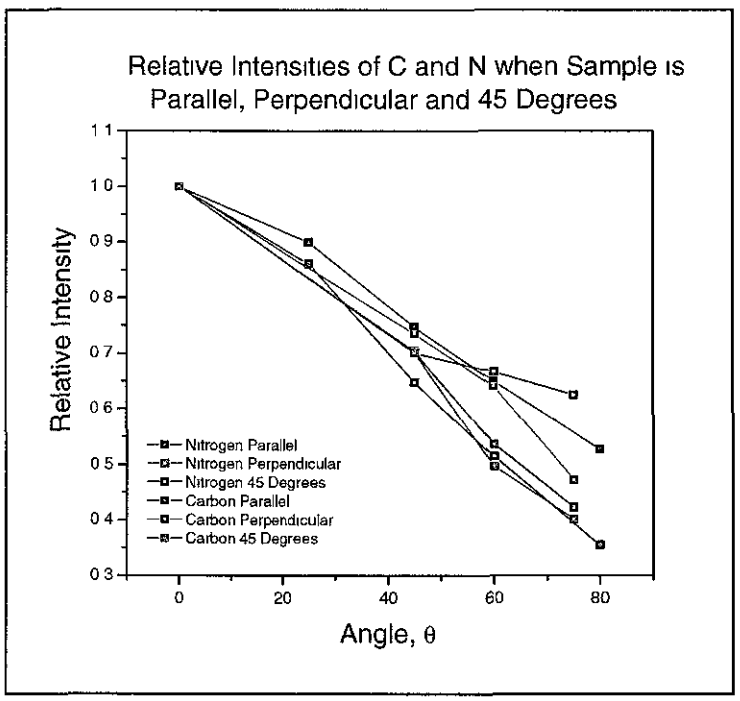

Figure 6.11: A plot of the relative intensity under the π- π^* peak versus angle of incidence for the different azimutal orientations of the sample.

In NEXAFS the molecular orientation can be determined by analysing the polarisation dependence of the either the π^* or σ^* transition intensities. Here the π^* intensities were used. The tilt angle of the molecule was calculated from the equation 2.36 which is given in Chapter 2. The polarisation factor was quoted to be 0.85 for the SX700 beamline. Equation 2.36 was used to fit the intensity of the π - π^* peaks with α as an adjustable parameter. Figure 6.12 shows the correlation between the simulated data (shown in black) and the experimental data (shown in red) for the

azimutal angles (a) 0°, (b) 45° and (c) 90°. In general there is good agreement between the simulated and experimental data indicating that the value calculated for the tilt angle of CuTTBPc is accurate. The different tilt angles of the molecule calculated for different azimutal orientations of the sample are presented in table 6.1.

Azimuthal angle ϕ	Tilt angle α
0°	21 ± 0.269°
45°	18.5 ± 0.143°
90°	16 ± 0.103°

Table 6.1 : The tilt angles for different azimuthal angles giving an average tilt of 18.5 ± 0.3°.

The fits to the experimental data are shown in figure 6.12

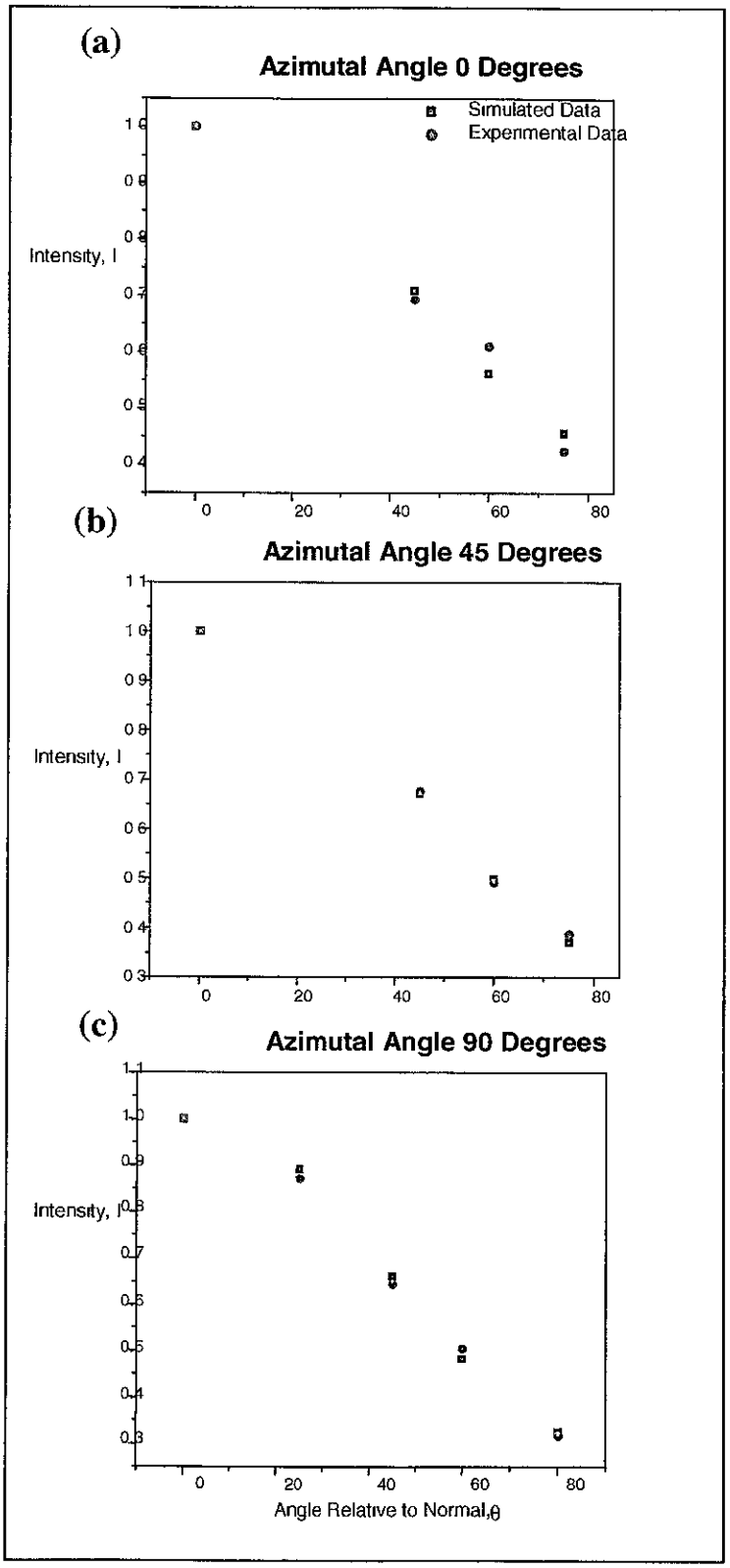

Figure 6.12: A comparison of the simulated data (black) with the experimental data (red) used to calculate the tilt angle of the molecule at various azimutal angles, (a) 0°, (b) 45° and (c) 90°.

Since the tilt angle for the different orientations were approximately the same this would imply that the azimuthal orientation of the sample is irrelevant. The average tilt angle for the three different orientations was 18.5° ± 0.3° relative to the surface normal, meaning that the molecule was almost standing upright on the surface.

6.5 XPS Study of the Angular Dependence of CuTTBPc and H_2TTBPc

In addition to NEXAFS another tool, namely XPS, was useful when exploring the geometry of molecular adsorbates and thin films on surfaces. XPS can be used to probe the HOMO and LUMO states. Ruocco *et. al.* [8] used XPS and XAS to study the orientation and satellite peaks of CuPc on Al (100) and found the orientation of the molecule to be 2° to the normal. Park *et. al.* [9] used XPS and LEED to study the orientation of CuPc on Au(001) and found the molecule be lying flat on the surface with unit cell dimensions of 1.27 nm × 1.27 nm. Through observations of XPS spectra Adolphi *et. al.* [10] found that changes in temperature can lead to the changes in the orientation of CuPc XPS was used by Lozzi *et. al.* [11] to study evaporated films of varying thickness of hexadecafluoro copper phthalocyanine on silicon. They found that ultra thin films showed a strong interaction between the surface molecules and the silicon substrate. This was attributed to charge transfer between the F-Si and Cu-Si. For bulk films they noted the presence of satellite peaks which were not visible for the ultra thin films. Hu *et. al.* [12] attempted to produce more ordered films of CuPc on glass by applying an electric field across the sample during the deposition of CuPc. Changes in the XPS spectra, along with changes in the AFM images and X-ray diffraction revealed differences in the chemical environment of copper and an increase in the ordering of CuPc. These findings showed that it was possible to detect molecular ordering using XPS and demonstrated that bulk films were required if the satellite peaks were be observed.

Evaporated films of CuTTBPc on SiO_2 and Si(111), along with H_2TTBPc on SiO_2, were prepared *in-situ*. These films were 10-20 MLs in thickness. The phthalocyanine was evaporated at a temperature of ~600K and at a rate of 0.2 ML

per minute from a tantalum crucible in a homemade deposition cell. The evaporated films and a 12 ML LB film of CuTTBPc (prepared as described in section 4.2.1) were analysed on station 4.1 at the SRS storage ring, Daresbury Laboratory, UK. The base pressure was $1x10^{-10}$ mbar and a Scienta SES200 hemispherical electron analyser with a total energy resolution of 100 meV was used. Angular dependence measurements were taken over a range of angles at a photon energy of 60 eV. To study the electron structure of the copper ion valence band spectra were measured in the photon energy range of 70-80 eV.

Figure 6.13 shows the spectra obtained at 60 eV for the 12 ML LB film. The angle of incidence of the incoming radiation was varied between 0°-75° relative to the normal . The HOMO peak was observed at binding energy of approximately 1.3 eV.As the angle of incidence increased the area under the HOMO peak decreased indicating the presence of molecular ordering within the LB film. This was not a surprising result as the very basis of LB technique states that LB films are highly ordered.

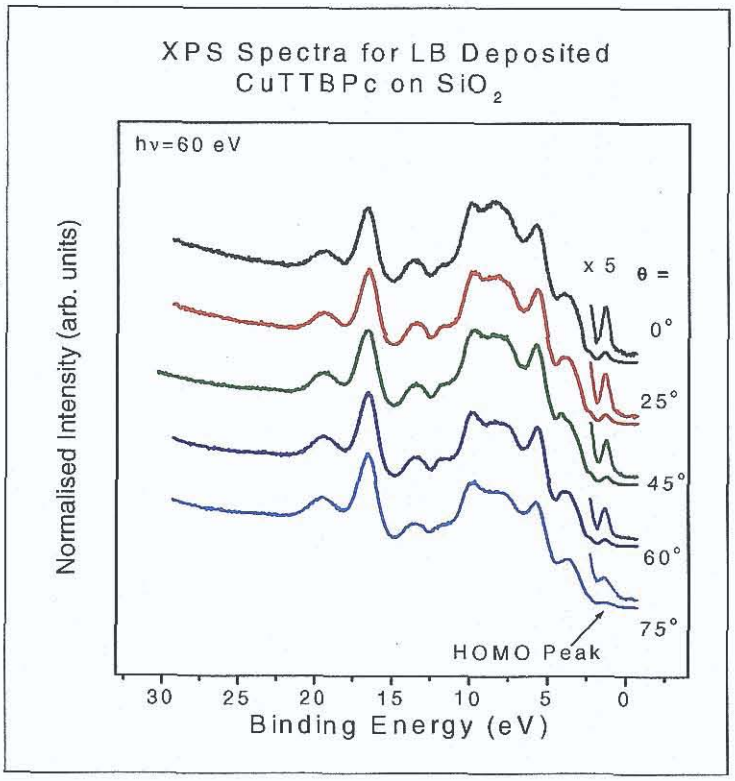

Figure 6.13:The XPS spectra for LB film of CuTTBPc on SiO_2.

XPS spectra were recorded at 60 eV as a function of the angle of incidence between 0°-75° for films of CuTTBPc evaporated on clean on SiO_2 (figure 6.14 (a)) and Si(111) substrates (figure 6.14 (b)). The thicknesses of these films was sufficiently large so that no features from the SiO_2 or Si substrate were observed in the spectra. Identical features were observed in the valence band spectra regardless of what surface the molecule was evaporated onto. For both sets of data a decrease in the HOMO peak was observed when the angle of incidence increases. Again this would indicate that there was molecular ordering within the deposited film. However, there appeared to be less ordering on the Si(111) surface, as the angular dependence was weaker.

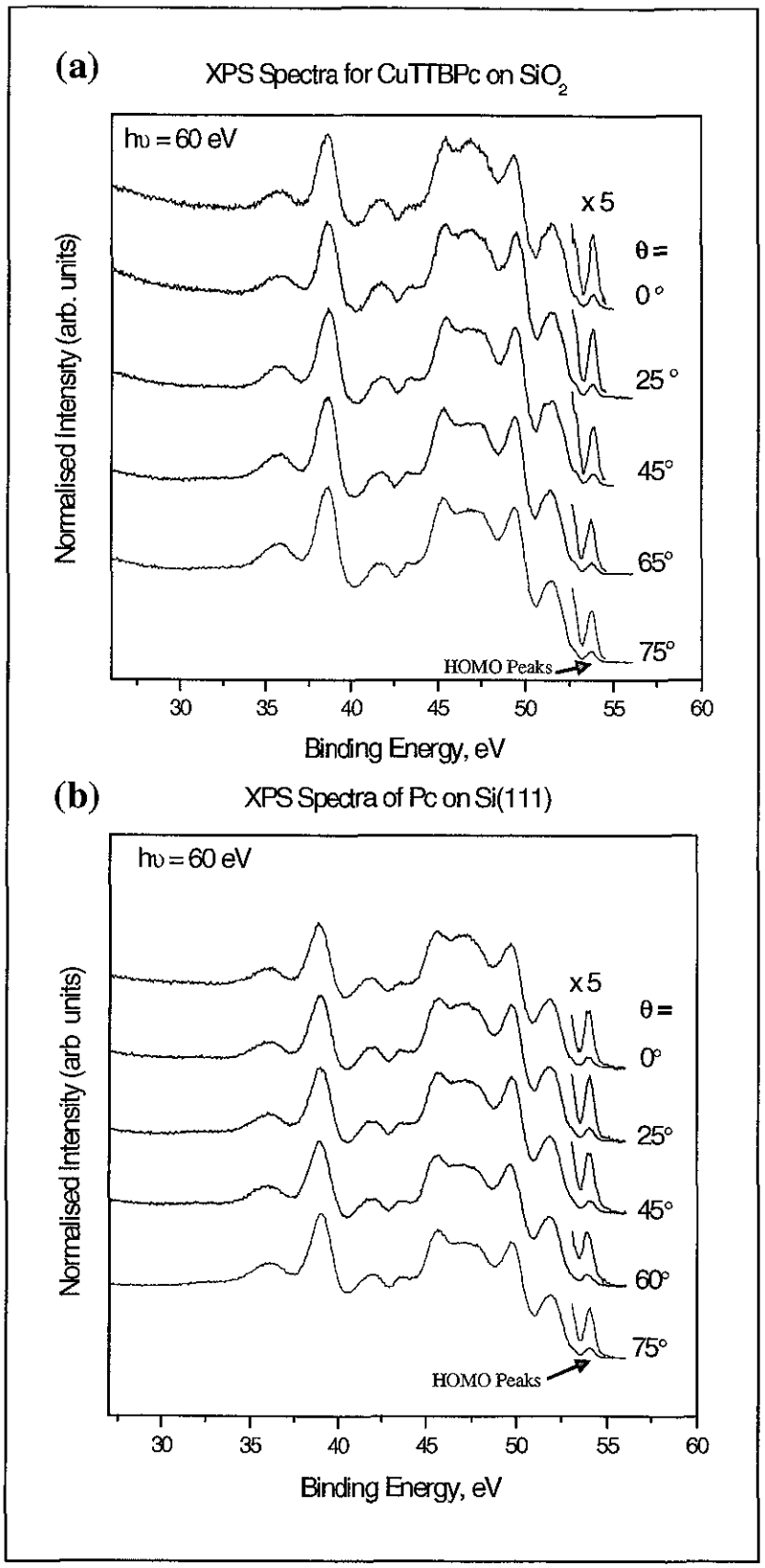

Figure 6.14:Angle dependent XPS spectra for CuTTBPc on SiO_2 (a) and Si(111) (b).

Spectra obtained for H_2TTBPc on SiO_2 were similar to those for both the LB and evaporated CuTTBPc films in that the HOMO peak decreased with angle. Figure 6.15 shows the H_2TTBPc spectra.

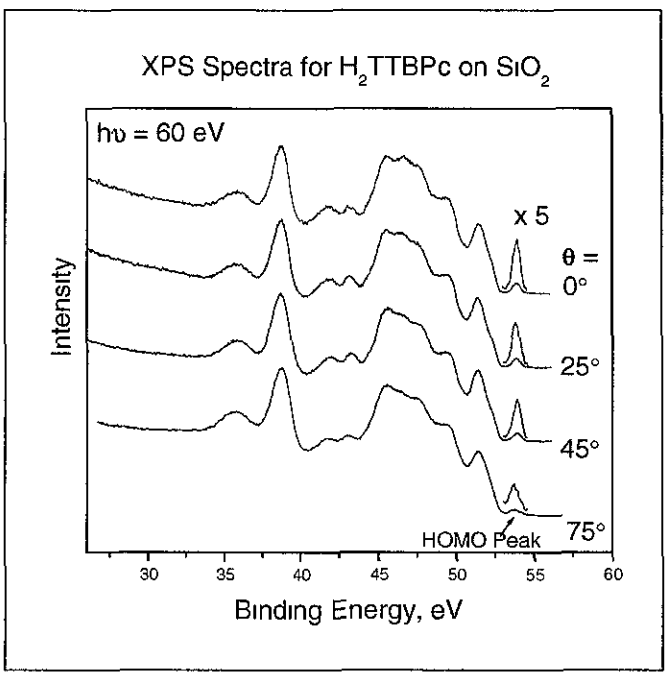

Figure 6.15: The XPS spectra for H_2TTBPc on SiO_2.

A plot of the relative intensities of the HOMO peak versus angle for the LB film and the evaporated film showed that there was a sharper drop in intensity for the LB film compared to the evaporated film, figure 6.16 (a). This suggested that the ordering was strongest for the LB film, followed by CuTTBPc and H_2TTBPc on SiO_2 and then CuTTBPc on Si(111). For comparison the NEXAFS results for the LB film of CuTTBPc on SiO_2 are also given in figure 6.16 (b). It can be seen that they showed the same angular dependence, within experimental error.

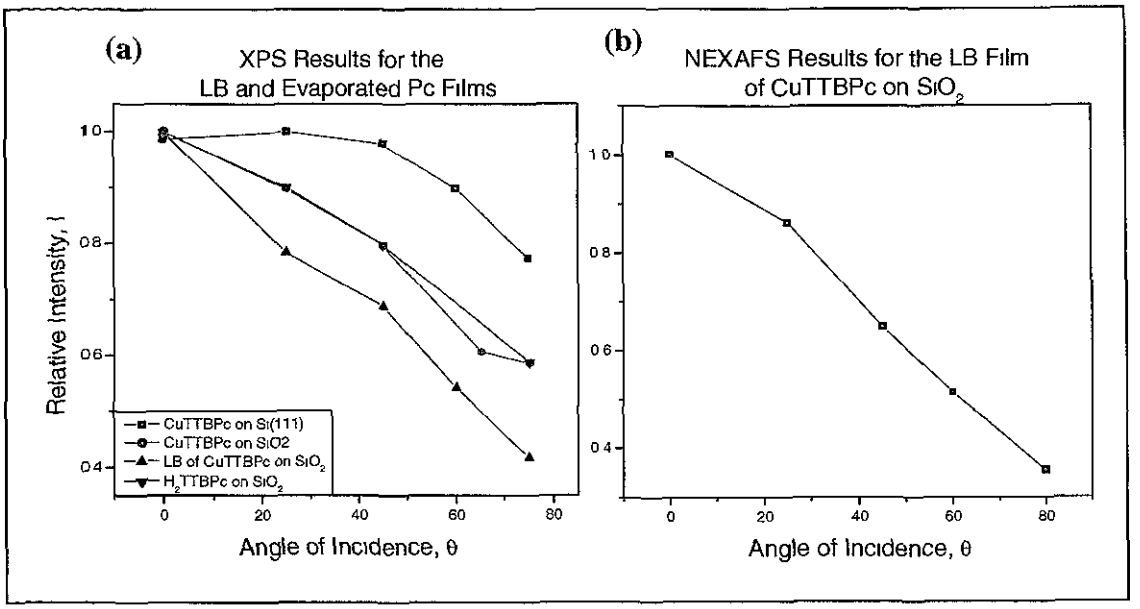

Figure 6.16: A comparison of the XPS (a) and NEXAFS (b) results of the relative intensities of the HOMO peak at different angles.

In conclusion it can be said that the NEXAFS spectra rsevealed a strong angular dependence in the CuTTBPc LB film. Through analysis of the interaction between the incoming radiation and the MOs of the molecule it was apparent that the CuTTBPc molecule was standing upright on the surface at an angle of 18.5±0.3°. VB XPS measurements were taken for the LB film and evaporated films of CuTTBPc on clean and oxidized Si(111). Both the LB and thermal evaporated films showed the same VB XPS spectra. The good agreement between the XPS and NEXAFS data further confirmed that the molecule had a standing orientation on the surface. XPS spectra also showed that the nature of the substrate was influential on the molecular orientation, as can be seen in figure 6.16.

6.6 XPS Study of Cu^{2+} ion in CuTTBPc

Considerable attention has been paid to the resonance and satellite structure for transition metals. Iwan *et.al.* [14] treated the central metal atom in CuTTBPc as Cu(II) as the minimum Cu-Cu distance was 5 Å, the particle density of Cu as reduced by a factor of approximately 50 compared to the metal and the atomic d-orbital were only slightly influenced in the tetragonal D_{4h} symmetry of the molecular field. In this work XPS measurements were taken to study the electronic structure of Cu(II) in CuTTBPc. Shake up peaks and the shake up process are described in

chapter 2 The satellite structure for the 3p core levels in transition metals reveals a strong resonance structure and this work attempts to explain to origin of this resonance as a basis for understanding of the multielectron effect. In order to study the copper satellite peaks it is necessary to use thick films. Ruocco *et. al.* [8] carried out synchrotron based photoemission studies of CuPc on Al (100) using 0.3, 0.5 and 4.0 nm thick films. They observed the disappearance of the copper satellite peaks at low surface coverages (0.3 and 0.5 nm), while at a thickness of 4.0 nm the satellite peaks were visible. Using XAS they found that the CuPc molecule tends to stand almost perpendicular to the surface (2° to the normal) when in the bulk form. XAS results for this research revealed that the CuTTBPc molecule was standing upright on the surface.

CuTTBPc films of 10-20 MLs have sufficient thickness to study the satellite peaks. CuTTBPc and H_2TTBPc were evaporated onto SiO_2 and valance band spectra were recorded for both surfaces using photons in the energy range of 70-80 eV. The H_2TTBPc spectra were then subtracted from the CuTTBPc spectra to obtain the contribution from the copper atom. The data was normalised as above and subtractions of the spectra were carried out using Origin[3]. An example of the subtraction is shown in figure 6.17

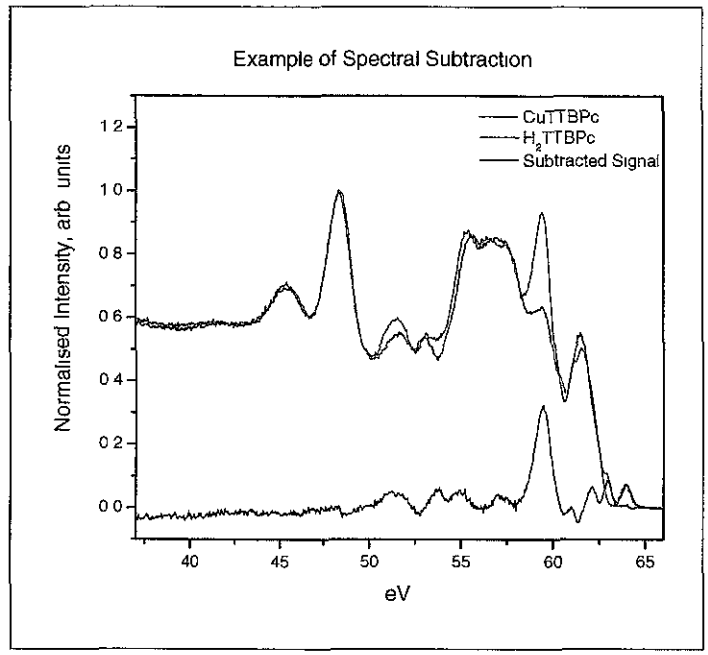

Figure 6.17: The subtraction of the H2TTBPc spectrum from the CuTTBPc spectrum. The subtracted spectrum is made up of the signals produced from copper alone. This subtracted spectrum was studied to determine the electronic structure of copper in CuTTBPc.

It is found that the electronic structure of copper (Cu^{2+}) in copper phthalocyanine is [Ar] $3d^9$ [13]. Identification of peaks in the copper satellite spectra was carried out with the use of the copper tables found in [15]. The subtracted spectra recorded with photon energies in the range of 70-80 eV were averaged to reduce the noise in the satellite spectra. For simplicity the position of the $3d^94s^1$ peak was set to zero, by getting a weighted average between the ^3D and ^1D peaks, and the position of the other peaks was found relative to this. Figure 6.18 shows the position and identification of the $3d^84s^2$, $3d^94s^1$ and the $3d^{10}$ peaks.

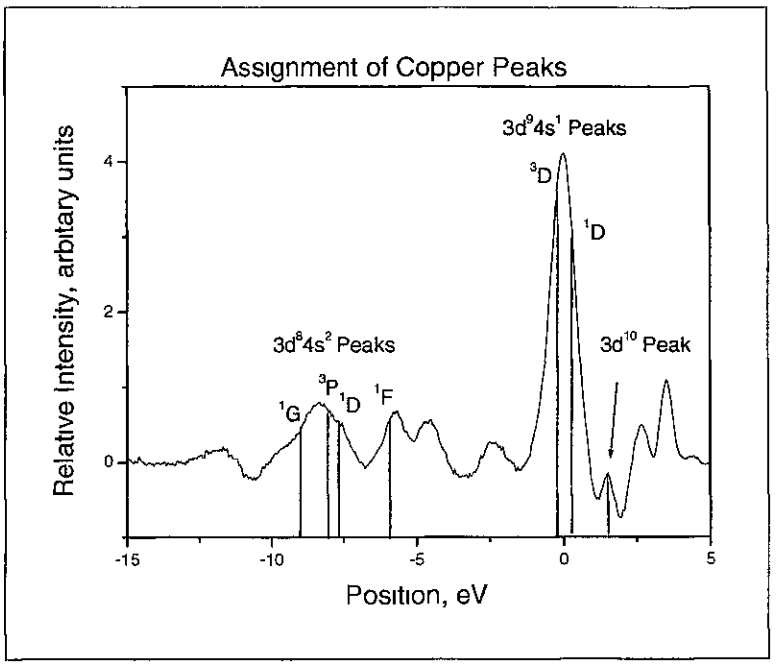

Figure 6.18: The averaged spectra of the copper with the identification of peaks.

Iwan *et. al.* [14] studied the electronic structure of copper in CuPc and found peaks which are in good agreement with the above results. They determined that the resonant satellites could be explained by an atomic shake up involving two 3d holes plus an excited 4s electron. Off resonance this two hole shake-up is excited according to

$$3d^{6}3d^{10}4s + h\upsilon \rightarrow 3p^{6}3d^{8}4s^{2} + e^{-} \qquad (6.1)$$

This occurs together with the one-electron photoemission process exciting a 3d electron:

$$3p^{6}3d^{10}4s + h\upsilon \rightarrow 3p^{6}3d^{9}4s + e^{-} \qquad (6.2)$$

which results in the ^{3}D and ^{1}D peaks at a relative energy of 0 eV, in figure 6.18. Iwan *et. al.* assigned the peak to the left of the ^{1}D as the $3d^{10}$ peak. At resonance, the excitation 3p → 4s followed by a simultaneous Auger decay creates a two hole state :

$$3d^{6}3d^{10}4s + h\upsilon_{res} \rightarrow 3p^{5}3d^{10}4s^{2} \leftrightarrow 3p^{6}3d^{8}4s^{2} + e^{-} \qquad (6.3)$$

This results in the resonant enhancement of the $3d^{8}4s^{2}$ final state, which was observed at a photon energy of 75eV, as shown in figure 6.19. Iwan *et. al* [14] also observed this resonance at a photon energy of 75 eV.

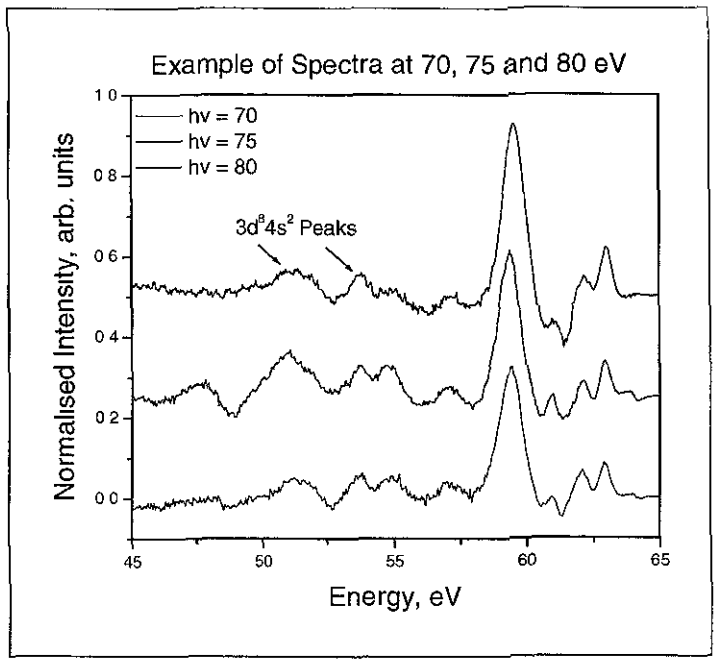

Figure 6.19: The spectra taken at 70, 75 and 80 hv. An increase in area under the $3d^8 4s^2$ peaks is observed around 75 eV before it drops off again.

Iwan et. al. [14] plotted the total area under the $3d^8 4s^2$ shake-up peaks in the photon energy range of 70-80 eV and found a maximum at approximately 75 eV. For this work the area under the $3d^8 4s^2$ shake-up peaks was found and was also plotted against photon energy. Although figure 6.20 shows a maximum at 75 eV it also shows a second peak at 78 eV.

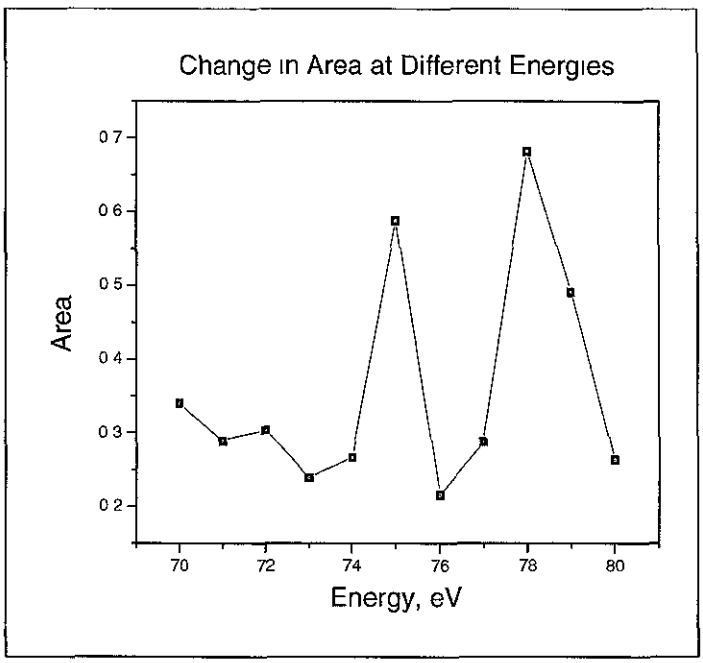

Figure 6.20: A plot of the total area under the $3d^8 4s^2$ peaks versus energy.

Since the resonance is due to the 3p to 4s transition spin orbit splitting should be observed and this would explain the presence of the second peak. To confirm the presence of this second peak the experiment would need to be repeated using a smaller photon energy step. In general there was, however, good agreement with this work and that of Iwan *et. al.* [14] regarding peak assignment and some agreement between the trends observed in the total area plots at different energies.

6.7 Conclusions

Both the NEXAFS and XPS results demonstrated that the CuTTBPc molecules had a definite orientation in the LB film. This was not surprising since the basis of the LB technique states that films produced using this method have a very well defined and ordered structure. Indeed Rajagopal *et. al.* [16] found that LB films containing PbA (lead arachidate) showed a strong angular dependence when studied by means of NEXAFS but little else has been reported on the finding of NEXAFS studies regarding LB films.

Using the NEXAFS technique Evans *et. al* [5] found that vacuum deposited CuPc was orientated in an upright position on an ordered S-GaAs substrate. This was contrary to the belief that CuPc stands upright on a disordered surface and

aligns flat on an ordered surface. A further study undertaken with SnPc on S-GaAs indicated that the SnPc molecule lies flat on the surface [7]. Although both phthalocyanines were deposited on S-GaAs surfaces the orientations of the CuPc and SnPc were different. This would indicate that the central metal ion in the phthalocyanine was influential in alignment of the molecule. AFM studies of the SnPc suggested that the film had a Stranski-Kratanov structure. Despite the formation of islands the NEXAFS results showed that overall the molecules did have some degree of ordering [7].

NEXAFS studies also indicated that molecular orientation depended not only the evaporated Pc molecules but on the surface morphology. Analysis of the C K-edge 1s $\pi \rightarrow \pi^*$ intensities found that hexadecafluoro CuPc (FCuPc) was standing at an angle of 60°, relative to the normal, on a MoS_2 substrate. Okudaira *et. al.* [4] and Kera *et. al.* [6] found that the orientation of H_2Pc was influenced by substrate and the temperature at which molecule was deposited. When H_2Pc was deposited on cold (90 K) Ag (111) the orientation was 50° relative to the normal. Annealing the sample to room temperature changed the orientation to from 50 ° to 40°. When the same molecule was deposited on a Ni_3Al (111) surface at room temperature the orientation was 30 to 55°, relative to the normal.

The AFM results for CuTTBPc LB films in this research showed that the molecules deposited in clusters as a result of the high degree of aggregation within the floating ML. This suggested the film has either a Stranski-Krastanov or Volmer-Weber structure. In spite of the islands found in AFM images of the LB films of CuTTBPc the NEXAFS results suggest that there was molecular ordering within the film and the film was possibly Stranski-Krastanov in structure. The average tilt angle of the molecule on SiO_2, was measured to be 18.5° ± 0.3° relative to the normal suggesting the molecule was practically standing upright on the surface.

The XPS scans of the VB region showed that the HOMO peak decreased in intensity as the angle of incidence increased. This indicated a strong angular dependence for the LB film of CuTTBPC and evaporated films of CuTTBPc on SiO_2 and Si(111). H_2TTBPc on SiO_2 also exhibited strong angle dependence. These results verified the NEXAFS results which found that there was molecular ordering

of the CuTTBPc molecule both in the LB and evaporated films. Plots of the relative intensities of the HOMO peak versus angle showed that both the substrate and method of film deposition played a role in the degree of ordering of CuTTBPc on the surface. Figure 6.16 showed that the LB film of CuTTBPc (on SiO_2) was the most ordered, followed by CuTTBPc and H_2TTBPc on SiO_2 and lastly CuTTBPc on Si(111) Since LB films were synthesised in a controlled environment, where is was possible to deposit the molecules layer by layer, it was not surprising that the LB films were more ordered than the evaporated films. The SiO_2 surface was relatively un-reactive compared to Si(111). This lead to the molecules diffusing evenly across the SiO_2 surface and forming ordered MLs whereas the Si(111) was quite reactive and molecule tended to form covalent bonds with the surface leading to disordered first and subsequent layers.

XPS studies of CuPc [8][9][10] and hexadecafluoro CuPc [11] showed the presence of satellite peaks in the bulk of the films. A photoemission study of the copper spectra for CuTTBPc on SiO_2 showed agreement with Iwan [14] and the copper table by Moore [15] which in turn suggested the copper in CuTTBPc has an oxidation state of Cu(II). Plots of the area under the Cu $3d^8 4s^2$ peaks did not follow the same trend as that of Iwan *et.al.*. This experiment should be repeated to double check the presence of a second peak due to spin splitting.

Overall it can be said that the NEXAFS and XPS results were complimentary of each other with both sets of results proving that molecular ordering exited in both the LB and evaporated CuTTBPc films.

Chapter Six References

[1] ***NEXAFS Spectroscopy***, Joachim Stöhr, Springer, 1996.

[2] MATLAB 7.1, The Language of Technical Computing, Version 7.1, 2005.

[3] Origin 6.1, OriginLab Corporation, 1991-2000.

[4] K.K. Okudaira , H. Setoyamaa, H. Yagia, K. Masec, S. Keraa, A. Kahnd, N. Uenob, ***Journal of Electron Spectroscopy and Related Phenomena,*** 137–140 (2004) 137–140

[5] D.A. Evans , H.J. Steiner, A R. Vearey-Roberts a, A. Bushell, G. Cabailh, S. O_Brien, J.W. Wells, I.T. McGovern, V R. Dhanak, T.U. Kampen, D R T. Zahn, D. Batchelor, ***Nuclear Instruments and Methods in Physics Research B***, 199 (2003) 475–480

[6] S. Kera, M.B. Casu, K R. Bauchspieß, D. Batchelor, Th. Schmidt, E. Umbach, ***Surface Science***, 600 (2006) 1077–1084.

[7] Vearey-Robertsa, H.J. Steinera, S. Evansa, I. Cerrilloa, J. Mendeza,b, G. Cabailhc, S. O'Brienc, J.W. Wellsc, I.T. McGoverna, D.A. Evansa, ***Applied Surface Science***, 234 (2004) 131–137.

[8] A Ruocco, F. Evangelista, A. Attili, M.P. Donzello, M.G. Betti, L Giovanelli, R. Gotter, ***Journal of Electron Spectroscopy and Related Phenomena***, 137–140 (2004) 165–169.

[9] K. T.Park, Alfred Miller, Kamil Klier, Robert L.Opila, Jack E.Rowe ***Surface Science***, 529 (2003) L285–L292.

[10] Barbara Adolphi, Olena Berger, Wolf-Joachim Fisher, ***Applied Surface Science***, 179 (2001) 102-108.

[11] L. Lozzi, L. Ottaviano, S. Santucci, ***Surface Science*** 470 (2001) 265-274.

[12] W.P. Hu, Y.Q. Liu, S.Q. Zhou, J. Tao, D.F. Xu, D.B. Zhu, ***Thin Solid Films*** 347 (1999) 299-301.

[13] Sergey. A. Krasnikov, Claire J. Hanson, Anttilio A. Cafolla, Dimer Structure of the CuTTBPc layer on the Ag/Si(111)($\sqrt{3}$ x$\sqrt{3}$) R30°surface: STM/STS study, Journal of ***Physics condensed Matter***,

[14] M. Iwan, E. E. Koch, ***Solid State Communications***, 34 (1980) 57-60.

[15] C. E. Moore, ***Atomic Energy Levels***, Vol. 3 U. S. National Bureau of Standards, Circular No. 467, U.S. GPO, Washington, D. C. (1958).

[16] A. Rajagopal, A Dhanablan, S. S. Major, S. K. Kulkarni, ***Applied Surface Sciecne***, 125 (1998) 178-186.

Chapter 7

Conclusions and Future Work

The synthesis of LB films can be a difficult task owing to the many external influences (humidity, pH, background noise, contamination etc.) which can have a negative effect on the film quality. Despite this it was possible to produce ordered films with molecules which traditionally may have been disregarded for the LB technique simply because they were not purely amphiphilic in character. CuTTBPc is notorious for aggregating due to lack of any hydrophilic moieties within the molecule and hence would not be considered ideal when trying to produce smooth, uniform monolayers. As the results presented in chapter 4 show this aggregation can be reduced by incorporating AA into the monolayer. In contrast to CuTTBPc, AA is an easy molecule to work with as it has both hydrophilic and hydrophobic properties. Isotherms of AA show very clear and distinct phase changes. Experiments involving AA showed that even slight changes in the dipping parameters can alter the quality of the LB film produced. Isotherms of pure CuTTBPc gave a Limiting Area per Molecule (LAM) of 44 (±1) $Å^2$ per molecule, this values indicates that there is a high degree of aggregation within the monolayer. Films produced with pure CuTTPc were found to be Y-Type indicating that the layers were being deposited on both the up- and down-stroke but the aggregation would result in formation of rough films. AA and CuTTBPc were mixed together in varying molar ratios and it was found that the aggregation could be reduced. Films of the 1:1 CuTTBPc:AA were found to be Y-type but the low transfer ratios suggested the film quality was poor. Films with thicknesses of 1 to 21 monolayers were synthesised to examine how the layer by layer growth was effected when mixing an aggregating molecule (CuTTBPc) with a non-aggregating molecule (AA). Films produced with 1:2 to 1:10 CuTTBPc:AA and 2:1 to 8:1 CuTTBPc:AA were both found to be poor quality Y-Type.

The AFM enables the surfaces of the above films to be studies on a micron scale. The AFM images of the 11 layer pure CuTTBPc film showed clusters. This would be expected as the isotherms showed aggregation. Interestingly the AFM images of a 1 layer 1:1 CuTTBPc:AA film had smooth regions with pinholes (characteristic of AA) and regions where clusters (characteristic of CuTTBPc) sat on

top of the smooth regions. Films with a thickness greater than 3 layers were found to be rough in appearance due to the pinholes and clusters. For the 11 layer films, which contained a varying amount of AA, it was found that as the molar ratio of AA went from 1:2 to 1:10 CuTTBPc:AA the films gradually started to take on a smooth appearance as the concentration of AA increased. For the 11 layer films produced with 2:1 to 8:1 CuTTBPc:AA the films, in general, exhibited characteristics of CuTTBPc with the presence of clusters.

The thickness refractive index and extinction coefficients for the LB films were found using ellipsometry. The diameter of the light beam was 1.5 mm and therefore a much greater area was averaged using the ellipsometer. Analysis of the isotherms and the AFM images suggest that aggregation may be an obstacle when trying to grow films with a uniform thickness. In fact the ellipsometry results showed that there was a very strong linear dependence between the thickness and the number of layers for the 1 to 21 monolayer films produced with 1:1 CuTTBPc:AA This confirmed that, despite the aggregation, the layers were stacking in a uniform fashion. The average monolayer thickness was calculated to be 2.31 (±0.33) nm for these films which was in close agreement with the AFM result of 1.70 (±0.04) nm. For the 11 layer films made with solutions of 1:2 to 1:10 CuTTBPC:AA the thickness was relatively uniform as was the thickness with the 11 layer films made with 2:1 to 8:1 CuTTBPc:AA. Average monolayer thicknesses of 2.35 (±0.14) nm and 2 38 (±0.16) nm were obtained respectively. The overall variation in the thickness values may have been a result of some uncontrollable parameters such as the varying degree of aggregation in each individual monolayer or any slight changes in the experimental setup, for example the temperature or humidity in the laboratory.

The n and k values were also studied. For the 1:1 CuTTBPc:AA films with thicknesses ranging from 1 to 21 monolayers, an exponential growth was found for the k value. The k values began to level off after the 11^{th} layer indicating that film needs a certain thickness before the n value can be calculated for the "bulk material". An average k value of 1.57 was found for the films with a thickness of 11 monolayers of higher. The films produced when the amount of AA was varied gave

a k value of 1.52, while the films produced when the amount of CuTTBPc was varied gave a k value of 1.51. For the 1:1 films a linear decrease in the n values was observed as a function of film thickness. The average n value after the 11^{th} layer was found to be 2.21. Values of 2.84 and 2.66 were found for the 11 layer films produced when the amount of AA and CuTTBPc was varied, respectively.

The isotherms, transfer ratios and AFM results show that it is possible to manipulate the aggregation of the monolayer through the incorporation of AA. Ellipsometry results showed there was some degree of ordering in the LB films containing CuTTBPc. In order to investigate this further LB films and evaporated films of pure CuTTBPc were studied and compared to each other.

STM images were obtained of CuTTBPc on the Ag/Si(111) surface. The evaporated molecules were found to lie flat on the surface in tightly packed molecular arrays forming dimers and trimers on the surface. It was possible to image the empty and filled states of the CuTTBPc molecule by altering the bias, therefore making it possible to image the TTB groups or the phthalocyanine ring. An attempt to image CuTTBPc on Si(111) proved difficult but it was possible to carry out XPS and NEXAFS studies of evaporated and LB films of CuTTBPc on SiO_2 and on Si(111).

NEXAFS was employed to investigate the ordering with the bulk material of a 12 ML film of an LB deposited film. As the results presented in chapter 6 indicate there was a strong angular dependence and from that it was found that the molecule was standing upright at an angle of 18.5±0.3° to the surface normal. This result proved that there was definite ordering in the LB film.

XPS results for the LB film of CuTTBPc on SiO_2 were compared to the XPS results for evaporated CuTTBPC on SiO_2 and Si(111). The results again indicated that the LB film possessed the highest degree of ordering and were found to agree well with the NEXAFS results. The LB film of CuTTBPc (on SiO_2) was the most ordered, followed by CuTTBPc and H_2TTBPc on SiO_2 and lastly CuTTBPc on Si(111). The nature of the substrate influenced ordering. The SiO_2 surface was relatively un-reactive compared to Si(111). This lead to the molecules diffusing evenly across the SiO_2 surface and forming ordered MLs whereas the Si(111) was

quite reactive and molecule tended to form covalent bonds with the surface leading to disordered first and subsequent layers. STS studies of CuTTBPc on Ag/Si(111) were also found to agree well with the NEXAFS and XPS results.

A study of the satellite peaks of copper in the CuTTBPc molecule revealed that the Cu was in a Cu(II) state. The spectra obtained agreed well with that of others.

The results of this research showed the LB films were more ordered than the evaporated films. LB films were synthesised in air in typical laboratory settings. This meant that films can be produced relatively quickly, assuming there are few experimental obstacles to overcome. Results of this work indicate it was possible to make LB films of CuTTBPc even though CuTTBPc may not be traditionally considered suitable molecule for the LB technique. Not only was it possible to deposit such films it was also possible to control the exact ML thickness and produce films with a high degree of molecular ordering.

The LB technique is becoming increasingly more popular in areas such as gas sensing, molecular devices and non-linear optics where properties such as monolayer ordering (ie. X, Y or Z type films) and film thickness can be controlled and manipulated. LB films are also used as anti reflecting coating, biosensors and optical processing units. The LB technique remains potentially useful due to its simplicity and ability to build molecular assemblies defined on the molecular scale [1][2][3]. One of the appealing features of LB films is that several materials can be used to process devices with different functionalities. The technique also offers "the possibility to tune the layer architecture according to the demands of the desired moleculary engineered organic thin film devices" [1]. In comparison to other techniques, such as thermal evaporation, the LB equipment is relatively inexpensive and requires little laboratory space.

In conjunction with this, interest is also growing in phthalocyanine molecules and their various derivatives as these molecules tend to be chemically and thermally stable. The means that there are endless possibilities with research which can be carried out with LB films containing phthalocyanines. As environmental issues become more prominent LB films containing phthalocyanines are being used to

sense pollutants such as nitrogen oxides [4]. Mixed LB films containing phthalocyanines and fatty acids look particularly promising due to improvements in the kinetic response of the sensor without changing the chemical structure of the phthalocyanine. Future research could also focus on the replacing the fatty acid with other substances due to poor thermostability [5].

The research in this thesis has made considerably contributions in the area of thin films of CuTTBPc. It has been demonstrated that, despite the obstacles discussed, it was possibly to grow very ordered LB films with this molecule. The results from the evaporated films showed that STM images with an extremely high quality were obtained and such images have so far not been reported. NEXAFS and XPS results were in excellent agreement with each other and both sets of data agreed very well the STS results. Overall this research has shown that the LB technique is valuable in the field of thin films where precise control over the film is desired.

Chapter Seven References

[1] H. Motschmann, H. Möhwald, ***Langmuir-Blodgett Films***, A Review.

[2] R. Gains, Langmuir-Blodgett Films, Plenum Press, New York, 1990.

[3] A. Ulmann, ***Introduction to Ultrathin Organic Films: From Langmuir–Blodgett to Self-Assembly***, Academic Press, San Diego, CA, 1991.

[4] I. Emelianov, V. Khatko, ***Sensors and Actuators B***, 47 (1998) 158.

[5] I. Emelaniov, K. Khatko, ***Thin Solid Films***, 354 (1999) 237